https://lib.uliege.be https://matheo.uliege.be

Mémoire

Auteur : Lizin, Stéphane
Promoteur(s) : Rauw, Gregor
Faculté : Faculté des Sciences
Diplôme : Master en sciences spatiales, à finalité approfondie
Année académique : 2019-2020
URI/URL : http://hdl.handle.net/2268.2/9217

Avertissement à l'attention des usagers :

Tous les documents placés en accès ouvert sur le site le site MatheO sont protégés par le droit d'auteur. Conformément aux principes énoncés par la "Budapest Open Access Initiative"(BOAI, 2002), l'utilisateur du site peut lire, télécharger, copier, transmettre, imprimer, chercher ou faire un lien vers le texte intégral de ces documents, les disséquer pour les indexer, s'en servir de données pour un logiciel, ou s'en servir à toute autre fin légale (ou prévue par la réglementation relative au droit d'auteur). Toute utilisation du document à des fins commerciales est strictement interdite.

Par ailleurs, l'utilisateur s'engage à respecter les droits moraux de l'auteur, principalement le droit à l'intégrité de l'oeuvre et le droit de paternité et ce dans toute utilisation que l'utilisateur entreprend. Ainsi, à titre d'exemple, lorsqu'il reproduira un document par extrait ou dans son intégralité, l'utilisateur citera de manière complète les sources telles que mentionnées ci-dessus. Toute utilisation non explicitement autorisée ci-avant (telle que par exemple, la modification du document ou son résumé) nécessite l'autorisation préalable et expresse des auteurs ou de leurs ayants droit.

University of Liège
Master in Space Sciences

Master's thesis

Probing the wind interaction in the massive binary system HD149404 with XMM-Newton

Graduation Studies conducted for obtaining the Master's degree
in Space Sciences by LIZIN Stéphane

Academic supervisor: Gregor RAUW

Academic year 2019-2020

Abstract

This work is based on the XMM-Newton observations of the massive binary system HD 149 404 made of a type O7.5 If primary star and a type ON9.7 I secondary star. In 2018, XMM-Newton observed this system at three distinct phases, the two conjunctions and a quadrature, in order to investigate the hydrodynamic shock resulting from the collision of the stellar winds under different angles.

In this work, we will start by a brief explanation of HD 149 404 making use of the available scientific literature to understand its peculiarities and interest for the scientific world. Since this binary system harbors two massive stars and an hydrodynamic shock, the properties of those stars will be discussed as well as the physics behind such a shock, notably by establishing the Rankine-Hugoniot relations. At that point, the reason behind the necessity of an X-ray observation of the system will be made clear by detailing the different physical processes that happen in such binaries and are responsible for the emission of X-ray photons.

Starting with the full description of the XMM-Newton data transmitted by the European Space Agency, we will see how raw data can be turned into scientifically usable ones by the reduction process specific to the high energy astrophysics. The question of the background during the observations will be tackled and, among others, the impact of the filter used by XMM-Newton will be discussed. The source of interest, HD 149 404, will be clearly identified within all the sources in the field of view and, via background and source regions, an observational spectrum will be extracted.

This observational spectrum will serve, in the Xspec software, to create a spectral fitting model. First, a very simple model will be discussed and used as a basis to understand the process of modeling an X-ray spectrum. Then, we improve this spectral model making use of the results of previous studies of this system and testing various hypotheses. Once in possession of our best fit model, we will extract relevant properties of the binary system such as the X-ray fluxes or the L_x/L_{bol} ratio and compare them with expected behavior from colliding wind binaries. Finally, the Canto formalism will be used to model the collision between the stellar winds and extract properties of the binary system such as the orbital inclination.

Acknowledgment

This thesis was realized under the supervision of Professor G. Rauw from the department of Astrophysics, Geophysics and Oceanography and within the High Energy Astrophysics Group (GAPHE) of the university of Liège.

First and foremost, I would like to thank Professor G. Rauw and express my deepest gratitude and appreciation for his tremendous help throughout this entire year. Starting from his assistance with the selection of the lectures for this special 1-year master in space sciences, passing by the design of this thesis and to the constant oversight of this project, his advices were always well on point and strongly valued. Without this permanent backing and the many discussions we had, it would not have been possible for this master thesis to reach its current state. For the constant support and the hours dedicated to this thesis, I sincerely thank you.

I would like to thank, as well, all the members of the jury for the time invested in reading and assessing this thesis in the unusual situation we are currently living in.

Finally, I also wish to express my gratitude to my parents and family for their continuous support and encouragement throughout my years of study and regarding my decision to commit myself to a second master degree to follow my dreams.

LIZIN Stéphane

Contents

List of Figures

1 Introduction

This master thesis is dedicated to the study of a binary system which consists of two distinct stars orbiting a common center of mass. Unlike our solar system, binary systems can have a center of mass far away from a star center and in between the stars that make up the multiple star system. The barycenter position will depend upon the ratio between the masses of the stars forming the binary system and therefore will be closer to the most massive star. An example of a binary system can been seen on Figure 1 and and it illustrates a so-called cataclysmic variable (CV) [46]. This particular system is made of a White Dwarf and a low-mass stellar companion. The low-mass star fills up its Roche lobe[1] and transfers matter to its compact companion. This leads to the formation of an accretion disk around the White Dwarf clearly recognizable on the artist view. They are well known to manifest eruptions that can vary in intensity and one of the most famous ones is the eruption of Nova Cygni observed by the Hubble Space Telescope in 1992.

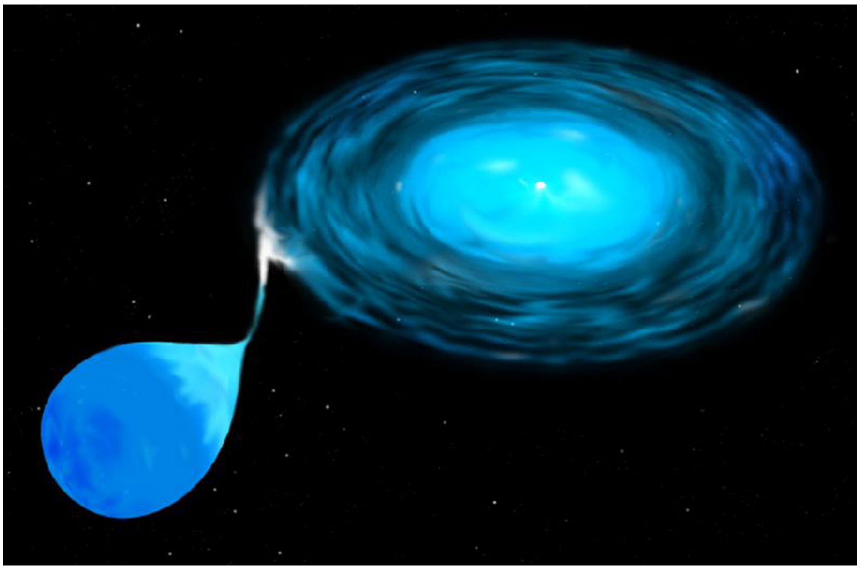

Figure 1: Binary system (Cataclysmic variable type) [46].

In this work, we will focus on another type of binary system called colliding wind binaries and, in particular, the binary system HD 149 404. Those systems are made of two massive stars which exhibit, like any other massive star, matter outflow through stellar wind. Mass-loss through a stellar wind has important consequences on the evolution of massive stars. The mass-loss rates are of order $10^{-7}\ \mathrm{M}_{\odot}/\mathrm{yr}$ during the main sequence, but increase dramatically during the more advanced stages of their life. The wind velocities are of order 1000 to 2000 km/s [46]. For single stars, the wind is to first approximation spherically symmetric as we will see in Section 2.2. However, when bound by gravity in a binary system, the two massive stars still produce winds but there is now an interaction between the two stellar winds producing a hydrodynamic shock between the stars. A representation of such an interaction at different phases of the binary can be seen on Figure 2.

In a first step, the concept of wind-wind interaction in those specific types of binary systems will be further detailed. We will discuss how this interaction takes place and what are the consequences of the emergence of a hydrodynamic shock. We will see if this is a stable phenomenon and what are the principal physical quantities behind the shock by introducing the Rankine Hugoniot relations. We take, here, an interest in the X-ray observation of the binary system HD 149 404 made of a type O7.5 If primary star and a type ON9.7 I secondary star [10] and we will see that there is a reason to study this

---

[1] The Roche lobe is the part of the space where the matter belongs to this star, taking into account the attraction of its companion star and the centrifugal pseudo-force.

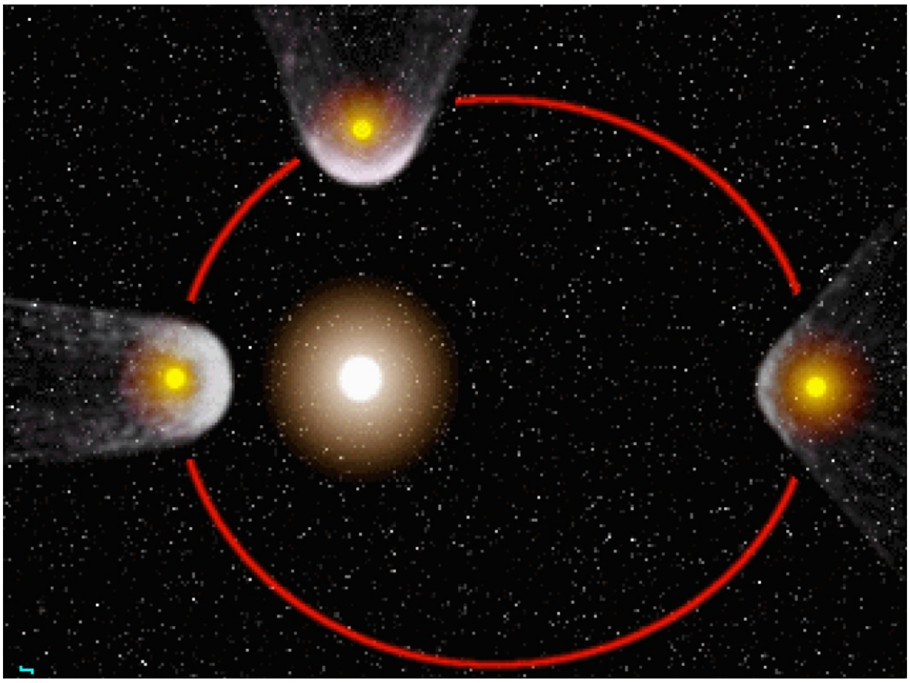

Figure 2: Binary system (Colliding wind) [46].

type of interaction in that specific spectral domain. We will see that the X-ray domain can bring some valuable information and greatly help us understand what is happening so far away from us. Before diving into the heart of the work, we will have a look at what other studies have found about this specific binary system HD 149 404 and what they can teach us about the properties of this binary. Indeed, this system has already been thoroughly studied by many scientists and engineers including by the Space Technologies and Astrophysics Research (STAR) Institute in the Space Sciences department at the University of Liège. Even though, in sciences, it is wise to expect the unexpected, those studies can give us some important clues regarding the binary system such as the spectral types of both stars previously mentioned or the past evolution of the system and help us answer some important question useful in the framework of this thesis: What are the inclination and period of the system? At what evolutionary stage is the system? Has the system experienced some perturbations that can affect our research or explain our results?

With any experimental scientific work, the most important things are the data and how we can obtain them. This is, of course, the most crucial step in any research and the basis of any hypothesis made during the analysis and interpretation parts. After the discussion regarding the binary system and its scientific history, we will switch our focus on the different ways we can collect X-ray data. The reason we had to use a space telescope will be brought up as well. We will discuss why we couldn't use the easier option with a ground-based telescope like the Very Large Telescope, VLT, from the Cerro Paranal Observatory. The special way to gather X-ray photons used by any X-ray telescope, like XMM-Newton, will be briefly explained, the difficulties that present the peculiar technique used will also be mentioned and the specific data set available for this work will be presented. This will be a good opportunity to understand how XMM-Newton, one of the most iconic spacecraft in the world, gathers data using specific filters and windows. By doing so, we will also make sure that the data collected were obtained under nominal conditions and are perfectly able to be used by scientists. Once in possession of raw but reliable data, we need to reduce them to usable data. Every step of the process will be detailed and we will see the peculiarities linked to X-ray data compared to any other part of the electromagnetic spectrum. During this process, we will, among other things, identify the source and background regions on the CCD detectors and inspect the raw data for any perturbing phenomena. In fact, making sure that the spacecraft had a stable, unperturbed attitude during the observation is not enough. We need to make sure that nothing happened during the observation with the surrounding and, in particular, with our Sun that has a "bad habit" of producing flares. The low-energy protons ejected during these flares can reach the X-ray detectors and produce a background flare that can seriously impact the quality of the X-ray data. In this work, we are solely interested in the binary system HD 149 404 and not in phenomena linked with the Sun's activity that need to be discarded. After this important step, we will have access to different images of the binary system coming from the EPIC cameras on XMM-Newton and the field of view available during the observations.

Once in possession of those precious data and, now, sure of their quality, we can start to analyze them. First, we will try to fit those data with the software Xspec [35]. This software, developed by NASA, is a command-driven, interactive, X-ray spectral-fitting program as described by the developers. With this software and the notorious χ^2 statistic, we will discuss different approaches to model the data collected by the spacecraft. We will try various combinations of multi-temperature optically thin thermal plasma models and extract the best-fit solutions. Besides different plasma components at different temperatures, we will also study the influence of the plasma composition mostly in terms of Carbon (C), Nitrogen (N) and Oxygen (O). This composition will not be randomly chosen but the scientific literature will be put to the contribution at this step. Indeed, as already mentioned, several studies have been carried out on this binary system and regarding the chemical composition of each star. Our goal will be, here, to model the resulting composition that best fits the data by answering the question of what is the resulting composition after the interaction: "Does each star contribute evenly to the X-ray emission or not?".

On Figure 2, placing an observer at the bottom of the picture, we can clearly see that, depending on the phase at which we look at the system, we will observe very different things. In the perfect case of the picture, with an inclination equal to ninety degrees, we will see the shock sideways at phase 0.25 and 0.75, lose the sight of the shock at phase 0.5 when the bigger star hides it and have a perfect view of the shock at phase 0 (not represented on the picture). This is a well-known behavior of colliding wind binaries and the reason we have at our disposal three sets of data very close to the three cases just mentioned (phase 0, 0.25 and 0.5 in the case of HD 149 404). When those three data sets have been through the reduction pipeline and have been correctly fitted with our best model, we can finally analyze them. We will take an interest in comparing the three different phases and see if we observe any variations between the three observations. We will extract a few relevant overall properties such as the ratio between the X-ray fluxes and the bolometric luminosity of the system, also known as the L_x/L_{bol} ratio. Once again, we will use the available literature and, the results and conclusions made from our scientific work, will then be compared to what is known about colliding winds in binary systems. In a final step, we will try to model the wind collision with a numerical simulation like it has been done for a similar binary system HD 228 766. Different methods and formalisms will be used in order to extract some constraints on the stellar wind properties such as the velocity of each wind or its density.

2 The Binary System

2.1 The History of HD 149 404

In this section, we will go over different scientific papers and extract the relevant information useful in the framework of this thesis. For further information about the binary system that might not be detailed here, you are invited to directly consult the articles themselves available in the reference section of this work. The scientific reviews of the binary system HD 149 404 are, here, presented in the form of a list of articles each accompanied by a brief summary fully inspired by the articles themselves, no external sources to the articles have been used to prepare this section.

2.1.1 The strange case of the massive binary HD149404 [10]

In 2001, G. Rauw & al. discussed a large set of spectra obtained over a period of 3 years with various instruments of the massive binary system HD 149 404 in order to derive an orbital solution for the system as well as the spectral type of the binary components. Based on the typical O-star absorption lines of He I, He II, N III, Si III, C IV and O III, they were able to assign the spectral type O9.7 to the secondary while the primary was found to be of spectral type O7.5. Similarly, based on criteria on the equivalent width (EW), a luminosity class of I was assigned to both stars. Those identification steps were peculiarly complex due to the heavy blending present in the various spectra.

	He I λ4471		cross-correlation	
	Prim.	Second.	Prim.	Second.
T_0(HJD–2450000)	1680.188 ± 0.531		1680.279 ± 0.174	
$\gamma\,(\mathrm{km\,s^{-1}})$	-54.0 ± 5.2	-46.4 ± 11.5	-46.6 ± 1.7	-41.6 ± 3.5
$K\,(\mathrm{km\,s^{-1}})$	62.8 ± 6.0	99.1 ± 9.0	59.7 ± 2.0	98.7 ± 3.2
$a\,\sin i\,(R_\odot)$	12.2 ± 1.2	19.2 ± 1.9	11.6 ± 0.4	19.1 ± 0.6
$m\,\sin^3 i\,(M_\odot)$	2.64 ± 0.66	1.68 ± 0.42	2.52 ± 0.21	1.52 ± 0.13
$q = m_2/m_1$	0.634 ± 0.085		0.605 ± 0.027	
$R_{\mathrm{RL}}/(a_1 + a_2)$	0.42 ± 0.01	0.34 ± 0.01	0.42 ± 0.01	0.34 ± 0.01
$R_{\mathrm{RL}}\,\sin i\,(R_\odot)$	13.2	10.7	13.0	10.3
rms (O–C) $(\mathrm{km\,s^{-1}})$	18.3		6.1	

Figure 3: Orbital solutions adopting a period of P = 9.81475 days and assuming e = 0.0. T0 corresponds to the conjunction with the secondary in front. The quoted errors correspond to 1 σ uncertainties[10].

In order to determine an orbital solution, the radial velocities of the absorption line He I λ4471, the least blended and most covered line among the data set, were used. Using a generalized Fourier spectrogramme technique, designed for uneven sampling, applied to the time series of radial velocities coming from the He I λ4471 line, the method yielded an orbital period of 9.814 days. The full orbital solution accounting for this 9.814 days period and an eccentricity of zero is available on Figure 3. Radial velocities obtained through a cross-correlation technique of the entire spectra with a mask also indicated an eccentricity compatible with 0, hence a circular orbit. On Figure 4, we have the best fit solution of the radial velocity curve of the two components from the determined orbital solution. Combining the minimum masses of the orbital solution and the typical masses of O9.7 and O7.5 supergiants, an orbital inclination of 21° was estimated for the binary system.

The emission lines from the spectrum of the secondary component of HD 149 404 indicate an enhancement of the Nitrogen in the atmosphere which motivated the revision of its spectral type to ON (i.e. an O-type star displaying anomalously strong N lines in its spectrum). This characteristic of the secondary along the location of the two stars in the HR diagram seems to indicate that the secondary, while currently the least massive star of the binary, seems to be the most evolved component. This could

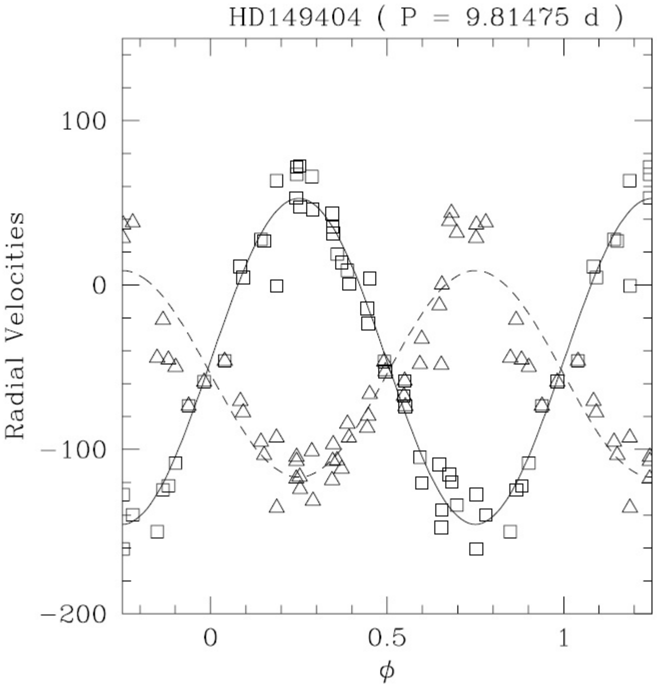

Figure 4: Radial velocity curve of the He I $\lambda4471$ line in the spectrum of HD149404 as a function of the orbital phase and assuming e = 0.0 (cf. Figure 3). The triangles correspond to the primary's RV s while the squares indicate the RV s of the secondary[10].

be explained by a significant loss of mass of the secondary through Roche lobe overflow in the past. This hypothesis seems to be confirmed by the extracted radii of the stars, 24.3 $R_\odot$ for the primary and 28.1 $R_\odot$ for the secondary. Indeed, the secondary star, with the assumed inclination, possesses a Roche lobe radius of 29 $R_\odot$ which is barely larger than the actual star radius. The question whether or not this Roche lobe overflow is still ongoing critically depended on the value of the inclination. In view of the uncertainties on the inclination, no firm conclusion could be reached.

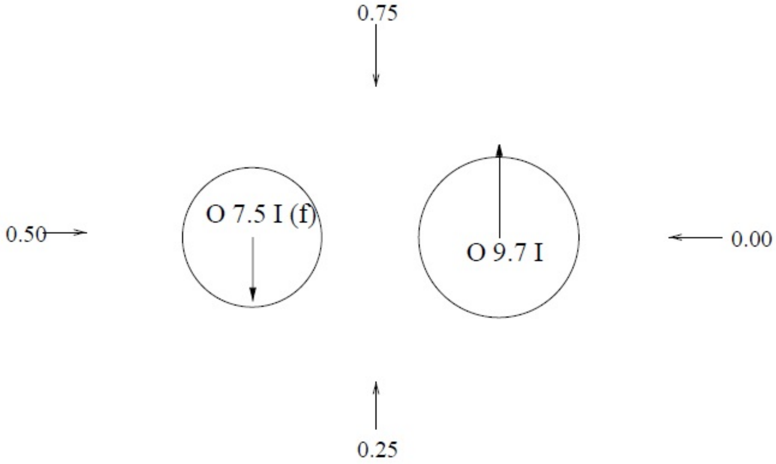

Figure 5: Schematic view of the HD149404 system projected on the orbital plane (i=21°) alongside the line of sight at different phases (ϕ= 0.0, 0.25, 0.5 ,0.75)[10].

It was also shown that several emission lines, such as Hα, were not coming from the stellar atmospheres but rather from the arms of a colliding wind shock region. On Figure 5, the binary system as well as the line of sight for orbital phases near conjunction and quadrature is represented projected on the plane of the orbit (shock region not shown here).

2.1.2 Observational signatures of past mass-exchange episodes in massive binaries: The case of HD 149 404 [9]

In 2016, F. Raucq & al. decided to investigate the mass exchange due to a Roche lobe overflow episode in the past of the binary system HD 149 404 as postulated in 2001 by G. Rauw & al. [10]. The data used correspond to the optical spectra from G. Rauw & al. [10] and are complemented by 25 UV spectra from the International Ultraviolet Explorer (IUE). In order to study the individual component of a binary system, the blended spectra must be separated which was realized by a spectral disentangling routine. This technique allowed the scientists to reconstruct the individual line spectra of the primary and secondary. Based on the spectral lines of those reconstructed spectra, a classification of the stars was made which perfectly coincided with the classification done in 2001 by G. Rauw & al. [10] (O7.5(f) I + ON9.7 I). Similarly, based on the reconstructed emission widths, a brightness ratio was estimated (l_1/l_2) yielding a value of 0.70±0.12.

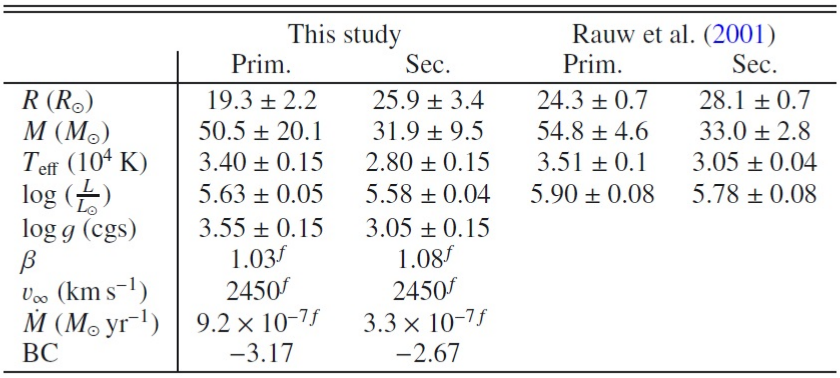

	This study		Rauw et al. (2001)	
	Prim.	Sec.	Prim.	Sec.
R ($R_\odot$)	19.3 ± 2.2	25.9 ± 3.4	24.3 ± 0.7	28.1 ± 0.7
M ($M_\odot$)	50.5 ± 20.1	31.9 ± 9.5	54.8 ± 4.6	33.0 ± 2.8
$T_{\rm eff}$ (10^4 K)	3.40 ± 0.15	2.80 ± 0.15	3.51 ± 0.1	3.05 ± 0.04
$\log\left(\frac{L}{L_\odot}\right)$	5.63 ± 0.05	5.58 ± 0.04	5.90 ± 0.08	5.78 ± 0.08
$\log g$ (cgs)	3.55 ± 0.15	3.05 ± 0.15		
β	1.03^f	1.08^f		
v_∞ (km s^{-1})	2450^f	2450^f		
$\dot{M}$ ($M_\odot$ yr^{-1})	9.2×10^{-7f}	3.3×10^{-7f}		
BC	−3.17	−2.67		

Figure 6: Stellar parameters of the primary and secondary stars as obtained with CMFGEN (f exponent stands for values fixed from the literature)[9].

In order to extract fundamental properties of the components of the binary system HD 149 404, a non-LTE model atmosphere code CMFGEN has been used. The stellar parameters corresponding to the best fit solution of the CMFGEN model are presented on Figure 6 and compared with the results from G. Rauw & al. [10]. Based on the now fixed stellar parameters, the CMFGEN code could fit the CNO abundances based on their lines in the reconstructed spectra (cf. Figure 7). From the spectral analysis and the derived CNO abundances, the suspected overabundance of Nitrogen in the secondary is confirmed. From the extracted radii, it is also clear that none of the two stars are currently filling their Roche lobe (filling factor of 15% and 73% for the primary and secondary respectively). Still based on the extracted radii and the estimated inclination of the system (i=21°), an evaluation of the rotation period led to 3.77±0.32 days for the primary and 7.46±0.95 days for the secondary which corresponds to asynchronous rotation of the two stars.

The observed CNO abundances of the secondary could be interpreted by considering that the current secondary star was actually, in the past, the more massive component of the binary system. This component transferred mass and momentum to the current primary star during a Roche lobe overflow episode. This process allows to explain the strange abundances found for the secondary since, during that RLOF episode, the outer envelope was removed (transferred to the primary) which revealed deeper layers of the star where material are coming from the convective core in hydrogen burning phase. This conclusion is also supported by the asynchronous rotations of both stars which is also explained by mass and momentum transfer resulting in a spin up of the primary. Accounting for the current spectroscopic

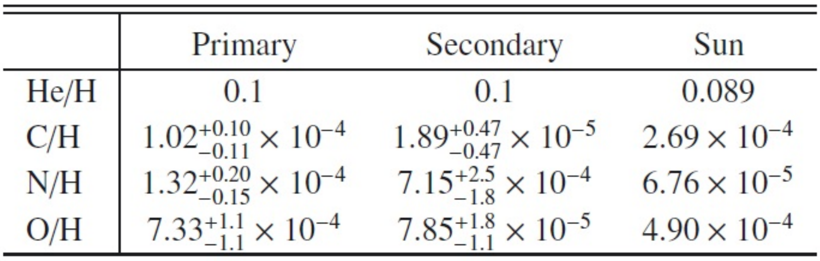

	Primary	Secondary	Sun
He/H	0.1	0.1	0.089
C/H	$1.02^{+0.10}_{-0.11} \times 10^{-4}$	$1.89^{+0.47}_{-0.47} \times 10^{-5}$	2.69×10^{-4}
N/H	$1.32^{+0.20}_{-0.15} \times 10^{-4}$	$7.15^{+2.5}_{-1.8} \times 10^{-4}$	6.76×10^{-5}
O/H	$7.33^{+1.1}_{-1.1} \times 10^{-4}$	$7.85^{+1.8}_{-1.1} \times 10^{-5}$	4.90×10^{-4}

Figure 7: Chemical abundances of the components of HD 149 404 [9].

mass, the secondary should have lost at least 9.3 $M_\odot$ assuming a fully conservative mass transfer (even higher in case of non-conservative mass transfer).

2.1.3 A compilation of interstellar column densities [17]

In 2011, S. B. Gudennavar and his collaborators decided to focus their study on the interstellar medium. They gathered 3008 absorption lines data from the literature from stars across our galaxy. The final objective was to create a huge database accessible to the scientific community to estimate the distribution of gas and dust in our galaxy.

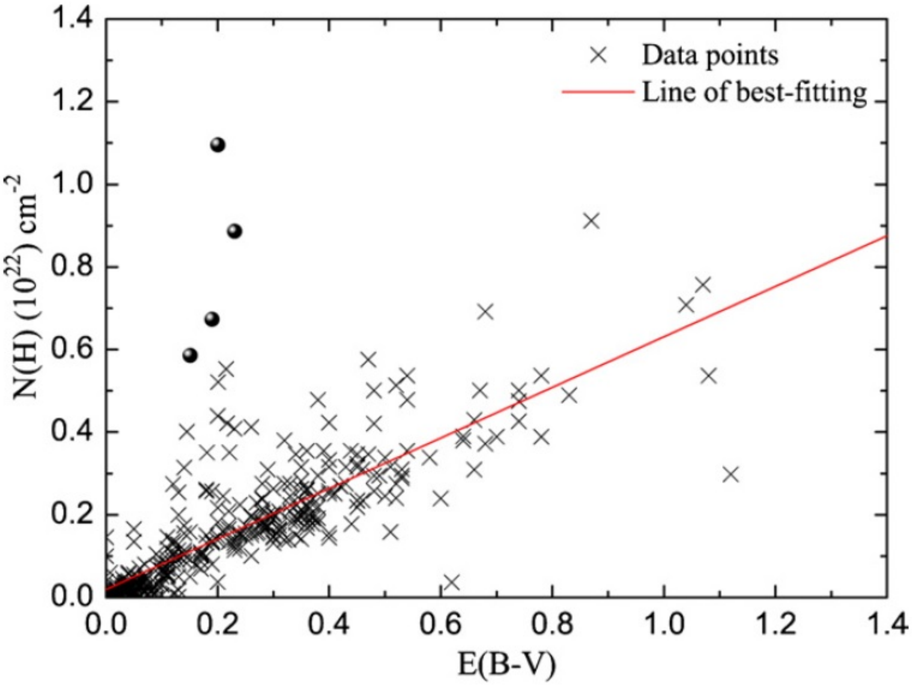

Figure 8: N(H) as a function of E(B-V)[17].

One of the most important results they found concerns the interstellar column densities. They managed to extract multiple relations between the densities of different species in the interstellar medium among one of particular interest for us, the relation between the Hydrogen column density and the color excess due to the reddening phenomenon resulting from the interstellar extinction. This relation is shown on Figure 8 and the corresponding best fit solution gives a slope of (6.1±0.2) 10^{21} atoms/cm^2/mag. This relation is especially useful when dealing with models to represent the X-ray spectrum of the binary system HD 149 404 to establish the Hydrogen column density of the interstellar medium. By making use of the SIMBAD database [47] for the color index (B-V) and the reference paper [13] for the intrinsic color index, the color excess can be computed which leads to a Hydrogen column density N_H of 3.72 10^{21} cm^{-2}.

2.2 Massive Stars

The stars involved in the binary system HD 149 404 of interest have been identified as a primary supergiant O7.5 I type and a supergiant companion ON9.7 I type [10]. Those massive stars, while representing a small portion of the stars in the universe due to their short lifetime of a few millions years, play a crucial role in the universe and possesses the most spectacular end of life with the famous supernova explosion. Massive, in astrophysics, is the adjective used to describe stars that are at least 8 times more massive than the Sun. Before entering in the heart of the work and discussing the wind interaction (cf. Section 2.3), it is a good time to briefly describe those peculiar objects in the universe as well as understand their formation and main characteristics that will be useful for the remaining of this work. It is also important to note that this section, dedicated to massive stars, was mostly inspired by the lecture on stellar structure and evolution given by professor M.-A. Dupret [20].

Figure 9: Pillars of creation in the Eagle Nebula, M16 open cluster, seen by HST [40].

Like any star in the universe, it all starts with a cloud of molecules, atoms or ions referred to as a nebula that can take various shapes. A famous one is the Eagle Nebula shown on Figure 9 that was observed by the Hubble Space Telescope. It is an active region in the Open Galactic Cluster Messier 16 made of dust and gas where a lot of star formation activity is taking place. In general, those clouds have a mass of around 50 000 times the solar mass and size of 40 light years. They are in hydrostatic equilibrium and can remain in that state due to their internal pressure, the centrifugal force and their magnetic field. However, several perturbations can break this equilibrium and cause the cloud to collapse. Indeed, when the cloud enters a higher density region like a spiral arm of a galaxy or is submitted to a shock wave coming from a close by supernova for instance, the cloud can't maintain its shape and collapses. As the principal cloud collapses, higher density regions inside it start to collapse as well and we have a fragmentation of the initial cloud. This initial collapse and fragmentation is isothermal and this process stops when the collapse becomes adiabatic. At this stage, the fragmentation stops, the biggest parts will give birth to the most massive stars while the smallest fragments will generate Brown Dwarfs, failed stars. The temperature of the central part, the core, increases and we have the dissociation of H_2 into hydrogen H when the core reaches 2000 K. This endothermic reaction causes a second collapse since the temperature and pressure don't increase as they should to compensate the weight of the gas column. In the zone where all H_2 have turned into atomic hydrogen, a new hydrostatic equilibrium is found. At this stage, the proto-star is hidden by the dust and gas coming from the cloud and the accretion disk, both originating from the material of the cloud fragment giving birth to this star.

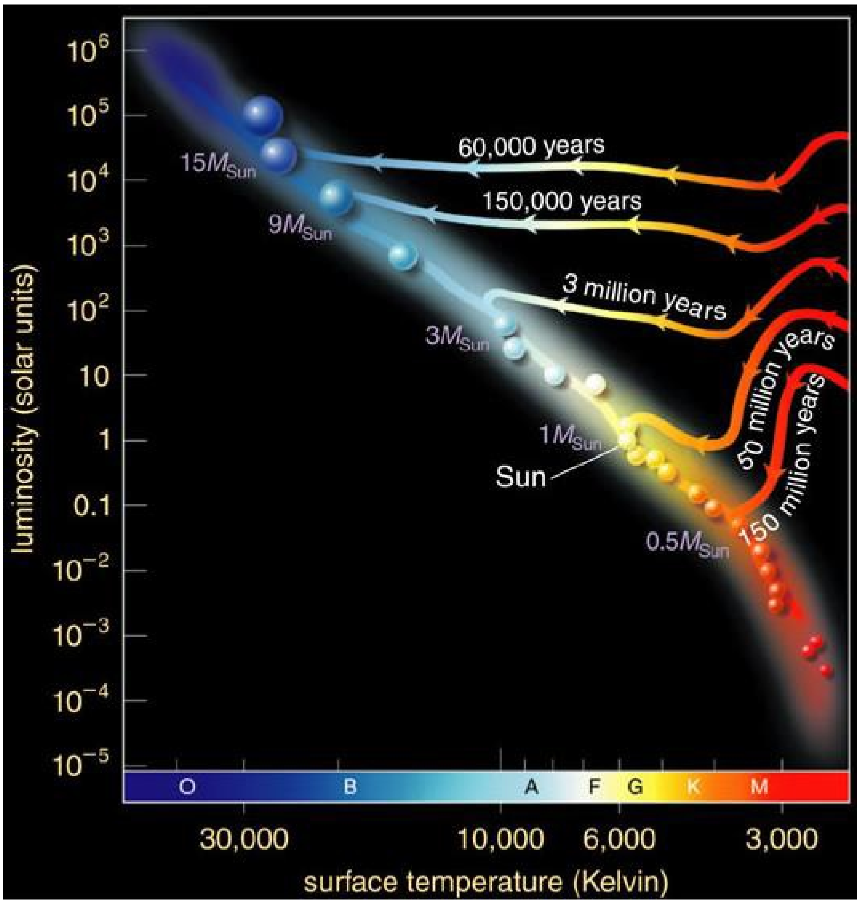

Figure 10: Pre-main sequence stellar evolution (Hayashi and Henyey tracks) [20].

When the star appears on the Hertzsprung-Russell diagram, it is located on the right side and on the so called Hayashi track (vertical lines) which corresponds to a phase of hydrostatic equilibrium in pure convection and without thermal equilibrium since, at this step, no nuclear energy is produced but the star radiates, we can see it. This is easily explained by the Virial theorem which states that during contraction, half the gravitational contraction energy is converted into internal energy and the other half is radiated. As the temperature increases, the opacity decreases and a radiative core appears. The star leaves the Hayashi track and follow the Henyey track crossing the HR diagram from the right to the left (horizontal line). We can see this evolution from the proto-star to the main sequence on Figure 10 and we can clearly notice that the time it takes to cross the HR diagram and reach the main sequence is shorter the more massive the star. As the star continues to contract before reaching the main sequence, the core temperature continues to increase and, when it reaches 10 million Kelvin, fusion reactions can start. Turning hydrogen into helium provides energy to the star and stops its contraction. After a short while, a thermal equilibrium is reached and the energy production by fusion reaction counteracts the radiative losses. As we consider massive star, electron degeneracy doesn't play a role and we will neglect its impact on the evolution of the star.

To fuse hydrogen into helium, the star has the well-know pp-chain and CNO cycle at its disposal. As we can see on Figure 11, in massive stars where the temperature is higher, the CNO cycle dominates

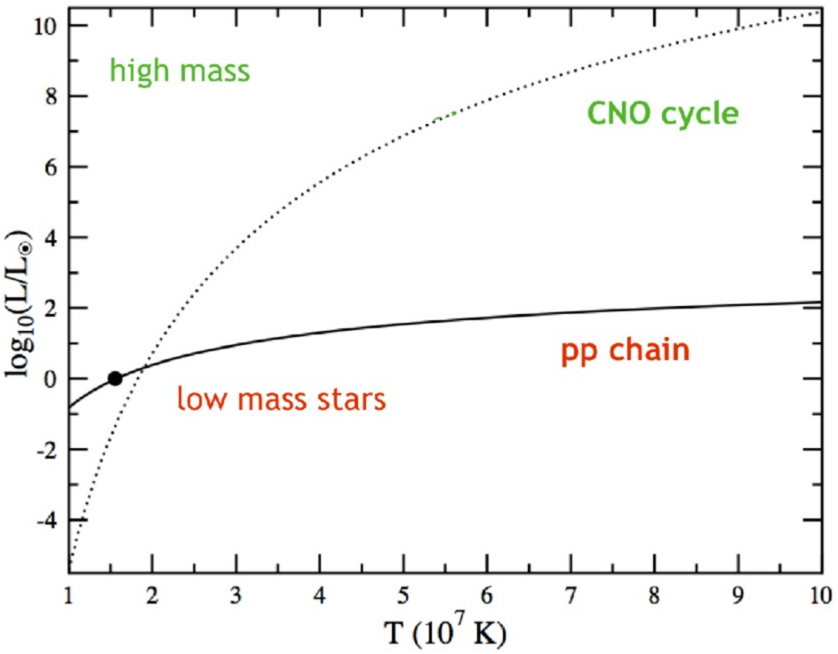

Figure 11: Hydrogen burning (PP-chain VS CNO cycle)) [4].

the energy production and conversion of hydrogen into helium by using carbon, oxygen and nitrogen already present in the star. The lifetime of those stars on the main sequence, phase of hydrogen burning, is very short compared to lower-mass stars. As a result of the mass luminosity relation that holds for stars on the main sequence, the higher the mass of the star, the higher its luminosity which, in turn, required a higher energy production by fusion reactions to maintain the thermal equilibrium. This higher energy production means that the star burns through its stock quite fast and will leave the main sequence rapidly after reaching it. If we consider a star of 10 solar masses, we can compute a lifetime of only 20 millions years. We need to keep in mind that a massive star has at least 8 times the weight of our Sun but this can go way higher. For instance, the mass of η Carinae A has been estimated to be between 100 times and 150 times the solar mass [38]. On Figure 10, we can also observe that, when those massive stars reach the main sequence phase, they are extremely hot ($T_{eff} \geq 15\ 000$ K), of spectral type O or B and extremely luminous which will have an important consequence throughout their life.

When the main sequence phase of hydrogen burning is over, the helium core contracts and heats up, the star envelope expands until hydrogen shell burning can start and eventually helium burning with the triple alpha process when a temperature of 10^8 K is reached. Similar to how the helium burning phase starts for the helium core, the carbon and oxygen core will also start the carbon burning followed by the photo-disintegration of neon, the oxygen burning and the silicon burning in successive phases as we can see on Figure 12. On this Figure 12, we can observe a comparison between the evolution post-main sequence of a massive star that will eventually become a red supergiant and a solar-like star whose different evolution phases will not be covered here. At the end of their life, massive stars have a core with an onionskin structure as shown on Figure 13. At this stage, every particle that can be created by fusion has been synthesized and no new fusion reaction can take place to turn iron into another heavier element. Thus, when the iron core reaches a mass close to the Chandrasekhar limiting mass, the core is not able to maintain its hydrostatic equilibrium and collapses. This collapse is so brutal that it can't be stopped by electron degeneracy and a supernova type II is taking place. The envelope is expelled which has an whopping impact on the interstellar medium by enriching it with heavier elements. The remnant of that supernova is either a neutron star (degeneracy of ions) or a black hole.

Since massive stars are frequently found in binary or even higher multiplicity systems, mass exchange through Roche lobe overflow can considerably alter their evolution. Indeed, the more massive star will

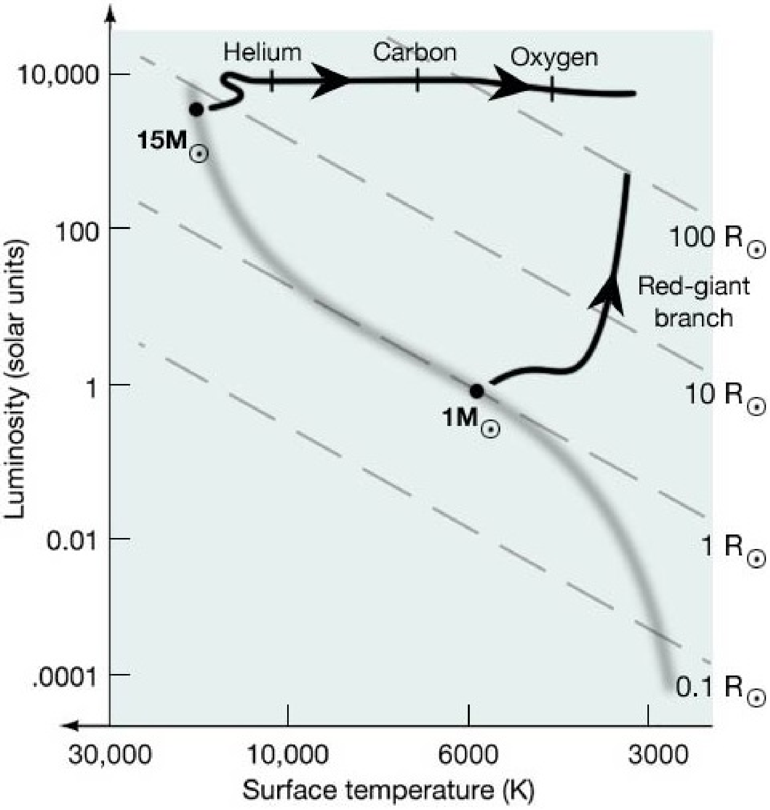

Figure 12: Post-main sequence stellar evolution (Solar like and massive star) [19].

usually fill up its Roche lobe first and transfer material and angular momentum to its companion. In this way, the mass donor loses its outer layers, thereby revealing layers of material that have been exposed to the ashes of nuclear reactions and display unusual CNO abundances. The mass gainer might eventually become more massive than the originally more massive star, and will see its rotational velocity increase due to the gain in angular momentum. This scenario most probably applies to HD 149 404 where the ON spectral-type of the secondary star is a clear indication of N enrichment (and C depletion), and where the nowadays more massive primary star is most likely the gainer of a mass transfer episode.

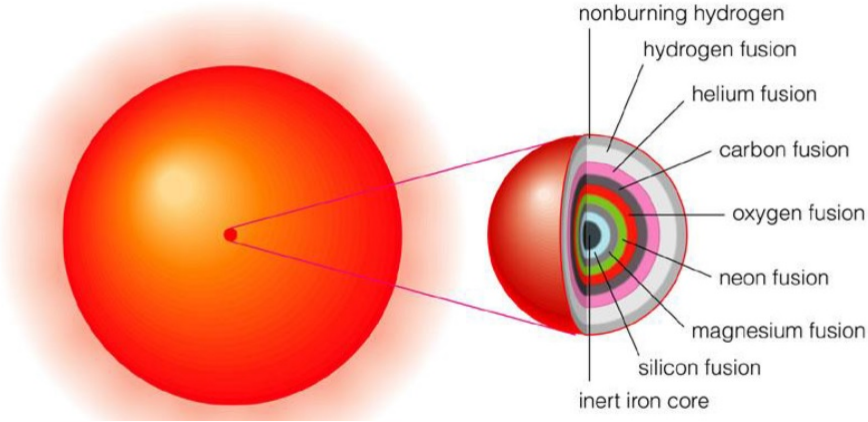

Figure 13: Core of massive stars at the end of their life (Onionskin structure) [20].

During their entire life and at different phases of their evolution, convective mixing in massive stars or mass-loss either through stellar winds or through Roche lobe overflow in a binary system can bring material processed by the CNO cycle and other fusion reactions from the stellar interior to the surface and upper atmosphere. This alteration of the stellar atmosphere composition has also a major impact on the stellar wind composition. Indeed, due to their high temperature and luminosity, those stars are an important source of UV radiations that create important radiation pressure. When a particle of the stellar atmosphere absorbs a photon, it gains a radial acceleration away from the star. At its turn, the particle re-emits a photon in a random direction and, the average direction of the resulting acceleration from this process is an acceleration away from the star, the particle from the upper atmosphere of the star is then pushed away from the star and with a net force in an outward direction: this is the process of creation of the stellar wind. Since the star is in hydrostatic equilibrium, its shape is a sphere and the wind has a spherical symmetry due to the nature of the wind driving mechanism. This symmetry is however broken when winds collide in binary system (cf. Section 2.3) and we have the appearance of a hydrodynamical shock. This acceleration of particles due to the radiation pressure of the massive star follow the velocity law (1) linking the distance of the particle from the star r and its velocity v (R being the radius of the star, v_∞ the terminal velocity of the wind and the parameter $\beta > 0$).

$$v(r) \;=\; v_\infty \left(1 - \frac{R}{r}\right)^\beta \tag{1}$$

The terminal velocity for typical massive O-type or Wolf-Rayet stars is between 1000 and 3000 km/s and is associated with huge mass-loss rates (3) from 10^{-7} up to 10^{-4} solar mass per year. This driving mechanism is also unstable, meaning that any perturbation of the particle velocity in the wind will inevitably grow in absolute value [46]. This leads to the formation of clumps of material in the stellar wind and instabilities in the fluid flow that can have a consequence on the hydrodynamic shock if the massive star is in a binary system (cf. Section 2.3). From the convective mixing, the internal fusion reactions and the ejection of particles via the stellar wind, we can already understand why we will study the composition of the plasma mostly in terms of Carbon, Oxygen and Nitrogen as postulated in Section 1. It must be stressed that mass-loss through stellar winds has an important impact on stellar evolution, especially during the more advanced stages of evolution, such as the Wolf-Rayet phase. Those stars possess such strong stellar wind that their envelope has been expelled and the core is exposed to the outer space.

2.3 Wind-Wind Interaction

When massive stars happen to be in a multiple stars system, the winds collide and we talk about colliding wind binaries. Binaries are systems made of two distinct stars but, in practice, multiple stars system can have more than two stars and are not limited to binaries. With more stars, those systems are usually referred to as Hierarchical systems as it is the case for the Triple Star system HD 150 136 which consists of a close binary system, two stars of spectral type O3.5 V and O6 V, with a very short period of 2.675 days and a third component of spectral type O7 V with a long orbital period of 8.2 years on a very eccentric orbit (e = 0.73). On Figure 14, we can see the evolution of the radial velocity of the third component with the red curve and the close binary formed by the two other stars with the blue curve. As far as this thesis is concerned, our multiple stars system HD 149 404, has been clearly identified as a close massive binary system consisting of two O supergiants, O7.5 If and ON9.7 I, with an orbital period of 9.81 days and a circular orbit (cf. section 2.1).

As massive stars can have highly supersonic winds up to 3000 km/s, their encounter gives rise to a contact discontinuity surrounded by two hydrodynamic shocks (one in each wind). This very thin discontinuity, of the order of the mean free path, leads to important changes in the fluid properties and is a region where particles, mostly electrons, can be accelerated and become relativistic. We will first take an interest in the shape and location of the shock, then, we will switch to the physical properties and the consequences of such a brutal disturbance and finally, we will understand the specific reasons why the observation is done in the X-ray domain and not the optical one for instance.

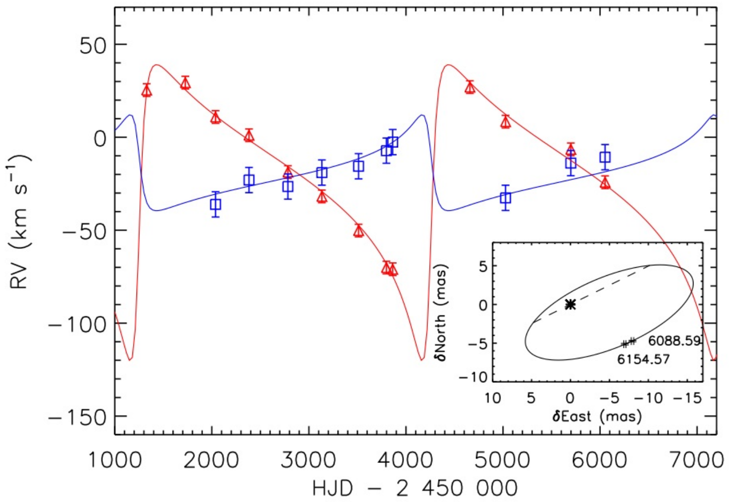

Figure 14: Radial velocity curve of HD 150 136 (blue = close binary, red = third star) [46].

In the followings sections dedicated to the hydrodynamic shock, the lectures on high energy astrophysics [45], variable stars [46] and aerothermodynamics of high speed flows [37] as well as the Caltech lecture on interstellar shocks [34] were especially useful regarding all the mathematical developments that will be done.

2.3.1 Hydrodynamic shock location

To compute the shape and location of the hydrodynamic shock, we will start with a 2D binary system made of two massive stars of radius R_1 and R_2 and separated by a distance d as we can see on Figure 15. Assuming the general case, the discontinuity will take a conical shape like any detached or bow shock observed in fluid dynamics and we will consider one point P on that curve representing the shock. Each of those stars has a stellar wind characterized by a velocity law v_i (2) and a mass-loss rate $\dot{M}_i$ (3) (i=1,2) where r_i, ρ_i and $v_{\infty,i}$ are respectively the distance between the center of a star and the point P, the density of the stellar wind and the terminal velocity of the stellar wind.

$$v_i = v_{\infty,i}\left(1 - \frac{R_i}{r_i}\right)^{\beta} \tag{2}$$

$$\dot{M}_i = 4\pi r_i^2 \, v_i \, \rho_i \tag{3}$$

The shape and location of the hydrodynamic shock are defined by the equilibrium between the dynamical pressure of the colliding stellar winds normal to the shock. Expressing that equilibrium for the arbitrary point P chosen, we have the following mathematical expression (4):

$$\rho_1 \, v_1^2 \, \cos^2(\phi_1) = \rho_2 \, v_2^2 \, \cos^2(\phi_2) \tag{4}$$

By introducing the continuity equation (3) and the expression of the stellar velocity (2) as well as inserting a very important parameter in colliding wind binaries, the wind momentum ratio $\mathcal{R}$ (5), also symbolized η by some scientists, in the equilibrium equation (4), we obtain (6).

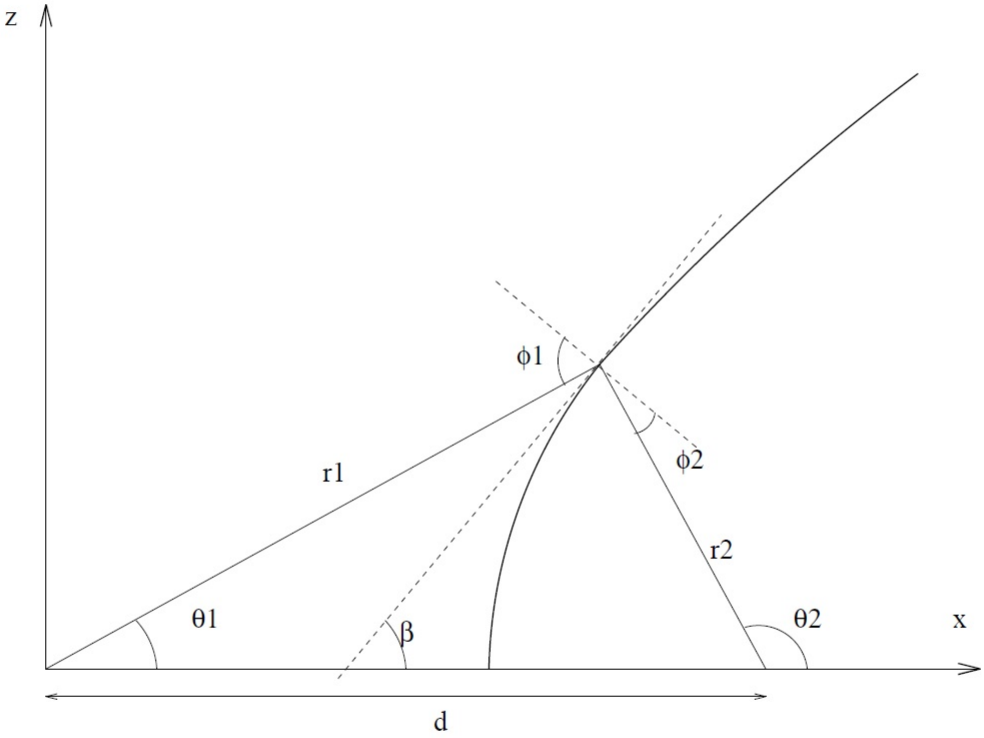

Figure 15: Hydrodynamic shock between two massive stars in a binary system [46].

$$\mathcal{R}^2 \;=\; \eta \;=\; \frac{\dot{M}_1 \; v_{\infty,1}}{\dot{M}_2 \; v_{\infty,2}} \tag{5}$$

$$\cos(\phi_2) \;=\; \frac{r_2}{r_1} \; \underbrace{\mathcal{R} \; \frac{(1-\dfrac{R_1}{r_1})^{\dfrac{\beta_1}{2}}}{(1-\dfrac{R_2}{r_2})^{\dfrac{\beta_2}{2}}}}_{\lambda} \; \cos(\phi_1) \tag{6}$$

Making use of the geometrical relations between the angles defined on Figure 15 ($\pi/2 - \phi_1 = \beta - \theta_1$ and $\pi/2 - \phi_2 = \theta_2 - \beta$), we obtain the following trigonometric identities (7 and 8):

$$\cos(\phi_1) \;=\; \sin(\beta)\;\cos(\theta_1) \;-\; \cos(\beta)\;\sin(\theta_1) \tag{7}$$

$$\cos(\phi_2) \;=\; \cos(\beta)\;\sin(\theta_2) \;-\; \sin(\beta)\;\cos(\theta_2) \tag{8}$$

Inserting those trigonometric identities to the equilibrium equation under its second form (6), we obtain the following expression for the ratio of the distances $\frac{r_1}{r_2}$ (9):

$$\frac{r_1}{r_2} \;=\lambda\, \frac{\tan(\beta)\;\cos(\theta_1) - \sin(\theta_1)}{\sin(\theta_2) - \tan(\beta)\;\cos(\theta_2)} \tag{9}$$

In equation 9, we introduced a parameter, $\tan\beta$, that characterizes the shape of the curve representing the hydrodynamic shock. By isolating this parameter and expressing it in terms of Cartesian coordinates, we end up with an expression of the contact discontinuity. Using the properties of right triangles, we can get rid of the sine and cosine in equation 9 and obtain the final expression for the shape of the hydrodynamic shock (10) where $r_1 = \sqrt{x^2 + z^2}$ and $r_2 = \sqrt{(x-d)^2 + z^2}$.

$$\tan(\beta) = \frac{dz}{dx} = \frac{z\,(\lambda\, r_2^2 + r_1^2)}{\lambda\, r_2^2\, x + r_1^2\,(x-d)} \tag{10}$$

If the winds of both stars have reached their respective terminal velocity before their interaction and the formation of the hydrodynamic shock, the parameter λ, whose expression can be found in equation 6, reduces to the wind momentum ratio $\mathcal{R}$ and we can go a bit further. For this to be possible, the interaction has to take place when $v_i \approx v_{\infty,i}$ meaning that the distance between the shock and each star needs to be significantly larger than the radius of the star ($r_i >> R_i$). Assuming that their terminal velocity is reached before the interaction, we can easily determine the location of the stagnation point of the flow. This point of the flow corresponds to a local velocity equal to zero and, from the Bernoulli principle in fluid mechanics, this corresponds to a maximum in terms of pressure. Coming back to equation 4 and introducing $\phi_i = 0$ (for i=1,2), we obtain the following equation (11):

$$\rho_1\, v_1^2 = \rho_2\, v_2^2 \tag{11}$$

By introducing the mass-loss rate $\dot{M}_i$ (3) (i=1,2) and the condition on the velocity in equation 11, we obtain (12):

$$\frac{\dot{M}_1\; v_{\infty,1}}{r_{1,\mathrm{stag}}^2} = \frac{\dot{M}_2\; v_{\infty,2}}{r_{2,\mathrm{stag}}^2} \tag{12}$$

To solve this equation with the two unknowns $r_{1,\mathrm{stag}}$ and $r_{2,\mathrm{stag}}$, we have to introduce the condition that $r_{1,\mathrm{stag}} + r_{2,\mathrm{stag}} = d$ which can be easily understood remembering the definition of those distances and the separation between the stars on Figure 15. Introducing the wind momentum ratio $\mathcal{R}$ (5) and utilizing the condition we imposed, we can solve the system and find the distance of the stagnation point to each star (13 and 14).

$$r_{1,\mathrm{stag}} = \frac{\mathcal{R}d}{1+\mathcal{R}} \quad \text{Distance from star 1 center} \tag{13}$$

$$r_{2,\mathrm{stag}} = \frac{d}{1+\mathcal{R}} \quad \text{Distance from star 2 center} \tag{14}$$

Following a similar reasoning and, with the same hypothesis, we can also determine the opening of the cone corresponding to the shock. As investigated by D. Eichler and V. Usov [49] during their study of wind interaction in binary system made of a typical Wolf-Rayet star and a OB companion, the result of the numerical computation of this angle can be approximated by an analytic expression of Θ, the half opening angle in equation 15.

$$\Theta \;\approx\; 120 \left(1 - \frac{\mathcal{R}^{-\frac{4}{5}}}{4}\right) \mathcal{R}^{-\frac{2}{3}} \quad [^\circ] \tag{15}$$

Now, we have at our disposal an expression for the shape of the hydrodynamic shock caused by the interaction of the stellar winds in a massive binary such as HD 149 404. We also have determined an analytic expression for the location of the stagnation point and the opening angle of the shock cone. In those three formulas, we can notice that the wind momentum ratio $\mathcal{R}$ is the only parameter or, in the general case, the most relevant one. At this step, this is an important information to keep in mind and that will be used in the section dedicated to the analysis of the data and the wind collision simulation (cf. Section 7). A popular method that will be used is the semi-analytical formalism developed by Cantó [14] that allows to compute the shape of the hydrodynamic shock by solving a set of non-linear equations. Still, it is important to note that this 2D model is rather simple and doesn't fully represent the far more complex reality. Indeed, one major assumption in the computation we made regarding the ability of the wind to reach its terminal velocity is highly debatable. The wind of star 1, by being exposed to the stellar radiation pressure of massive star 2, is slowed down and vice versa for the wind of star 2. This, coupled with the distance between the two stars being "relatively" small (especially in close binaries), greatly reduces the ability of both winds to accelerate and reach their terminal velocity. In this model, we have also completely neglected the fact that both stars are on an orbit and moving around their common barycenter and we have assumed a symmetric shock with respect to the line joining both stars (i.e. this formalism neglects the Coriolis deflection).

All those phenomena add up and can render the computation of the shock very difficult. The resulting hydrodynamical problem of the interaction of stellar winds in massive binary systems is, in reality, extremely complex and, like most problems in fluid mechanics, is highly sensitive to instabilities that might be present in the pre-shock wind and greatly affect the shape and position of the contact discontinuity. Moreover, the properties of the post-shock plasma strongly depend upon the efficiency of radiative cooling processes as we will discuss in the next section. For a more rigorous treatment of the hydrodynamic shock and its simulation in binary systems, we can have a look at the video on Figure 16. This simulation was developed by E. Gosset and E.R. Parkin in 2011 [8] and accounts for a 3D hydrodynamic simulation of the wind-wind interaction, in the binary system WR 22, which includes the effect of the stellar radiation pressure and the orbital motion. The stars are represented by a yellow dot and the shock, and region around the colliding wind binary, by the gas density from high density in red, passing by the white and finally blue for the lowest density. In this simulation, we can see two massive stars: the primary, a Wolf-Rayet star of 72 solar mass, and the smaller companion, an O-type star of 26 solar mass. The feature that stands out is the obvious effect of the orbital motion on the shock and especially the wake around and behind the O-type star. Focusing on the region between the two stars and not the spiral shaped wake, we can clearly see that the shape of the contact discontinuity is not symmetrical like in our reasoning. The surface of the shock is also not smooth but full of ripples representing the instabilities in the fluid flows that notably arise from the cooling of the post-shock plasma. The efficiency of this cooling is modulated by the changing orbital separation due to the highly eccentric orbit. In terms of location of the shock, as the O-type star moves on its eccentric orbit, we can see the evolution of the stagnation point which is even attached to the surface of the companion star around the periastron passage due to the huge intensity of the Wolf-Rayet wind. A similar remark can also be made regarding the evolution of the opening of the shock asymmetric cone.

Figure 16: 3D hydrodynamic simulation of the wind-wind interaction in WR 22 [33].

2.3.2 Hydrodynamic shock properties

After the details regarding the geometric characteristics of the contact discontinuity, we will take an interest in the physical changes brought up by the shock in the flow. On Figure 17, we can observe the evolution of the density across a shock wave in a gas made, at 100%, of Argon and at a Mach number of 9, meaning 9 times the speed of sound in the free flow, pre-shock, conditions of pressure and temperature given on the graph [37]. A few remarks can be drawn from the different curves representing the experimental data (○), the computational fluid dynamics, CFD, simulation of the Navier-Stokes equation (red curve) and the direct Monte-Carlo simulation of Boltzmann equation (blue curve). The first element, easily recognizable, corresponds to the continuous rise of the density throughout the shock. The second corresponds to the shock thickness that is of the order of the mean free path, the average distance between two successive collisions of molecules. The final observation concerns the rarefaction of the flow and the failure of the classical fluid dynamics (Navier-Stokes) to correctly describe the physical change during the shock. While not being extremely useful to describe the hydrodynamic shock happening in space at much higher Mach numbers, this introductory example already shows us how difficult it is to understand and correctly model the physics behind the shock itself. However, disregarding the region of the shock itself, we can see that the fluid dynamics is perfectly able to determine the pre- and post-shock conditions of the flow and this will be the main subject of this section.

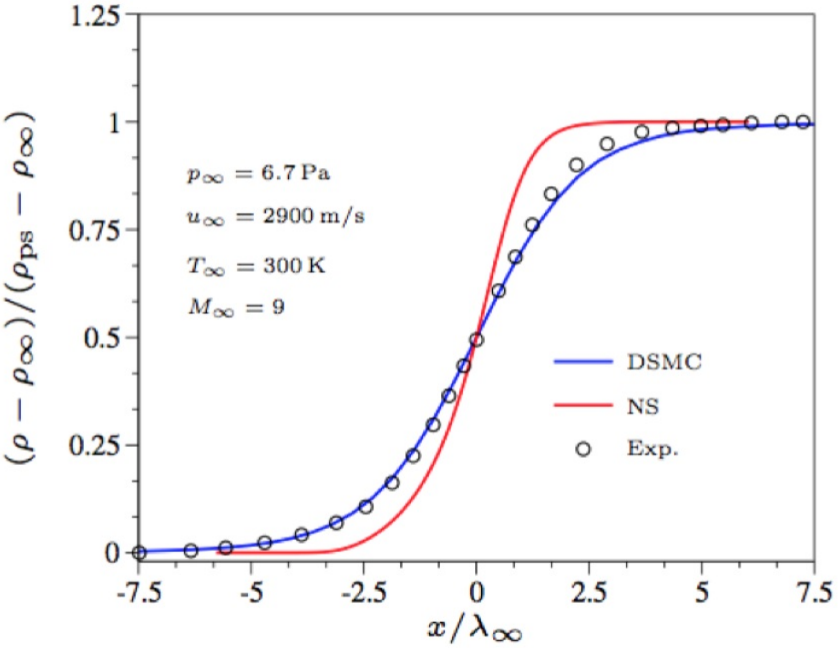

Figure 17: Normalized density distribution across shock wave in Argon at M=9 [37].

As almost everything in fluid dynamics, it all starts with the famous Navier-Stokes equations: the continuity equation (16) that accounts for the mass conservation, the conservation of momentum (17) and conservation of total energy (18). Those three equations are written with the Einstein summation convention that dictates that, when a sub-index (here i or j) is twice or more repeated in the same equation, one sums across the n-dimensions. This means, in the context of Navier-Stokes in 3 spatial dimensions, that one repeats the term 3 times, each time changing the index for one representing the corresponding dimension (in our case: 1,2,3 or x,y,z). Taking the continuity equation (16) as example, it is a shorter representation of: $\frac{\partial \rho}{\partial t} + \frac{\partial(\rho u_1)}{\partial x_1} + \frac{\partial(\rho u_2)}{\partial x_2} + \frac{\partial(\rho u_3)}{\partial x_3} = 0$. The momentum conservation equation (17) is, in the context of the Einstein summation convention, a superposition of 3 separable equations which could actually be written in three lines: one line equation for each i in each of which one sums the three terms for the j sub-index.

$$\frac{\partial \rho}{\partial t} + \frac{\partial(\rho u_i)}{\partial x_i} = 0 \tag{16}$$

$$\frac{\partial(\rho u_i)}{\partial t} + \frac{\partial(\rho u_i u_j)}{\partial x_j} = -\frac{\partial p}{\partial x_i} + \frac{\partial \tau_{ij}}{\partial x_j} + \rho f_i \tag{17}$$

$$\frac{\partial(\rho E)}{\partial t} + \frac{\partial(\rho u_i H)}{\partial x_i} = \frac{\partial(\tau_{ij} u_j)}{\partial x_i} + \rho f_i u_i + \frac{\partial(q_i)}{\partial x_i} \tag{18}$$

In this general form of the Navier-Stokes equations, we recognize a few properties of the fluid: the density ρ, the velocity vector $\underline{u}$, the pressure p, external body forces acting on the fluid $\underline{f}$, the total energy E, total enthalpy H, the heat flux $\underline{q}$ and the viscous stress tensor $\underline{\underline{\tau}}$ that can be expressed in terms of viscosity η and the velocity gradient tensor $\underline{\underline{S}}$ as follows 19:

$$\underline{\underline{\tau}} \; = \; -2\eta \underline{\underline{S}} \; = \; -2\eta \left(\frac{1}{2} \left[\nabla \underline{u} + (\nabla \underline{u})^T \right] - \frac{1}{3} \nabla \cdot \underline{u} \; \underline{\underline{I}} \right) \tag{19}$$

Let us consider a simple planar strong shock in a perfect gas and work in the frame where the shock is stationary as shown on Figure 18. As mentioned previously, we will try to compute the post-shock conditions (sub-index 2) and relate them to the pre-shock ones (sub-index 1). The following reasoning will start from the general Navier-Stokes equations of fluid dynamics, establish the Rankine-Hugoniot relations for a strong shock and describe the changes in physical properties of the flow for shocks created by the encounter of two different stellar winds which happens at very high Mach numbers (M >> 1).

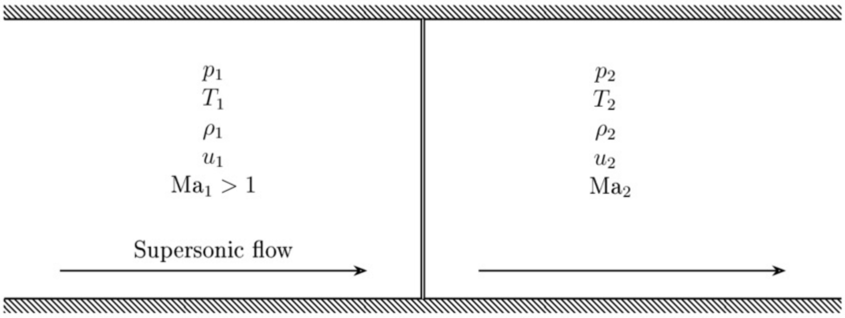

Figure 18: Steady normal shock [37].

Considering an inviscid flow in the absence of external forces and coupled with the approach shown on Figure 18, the Navier-Stokes equations can be simplified and solved for the post-shock conditions. Starting with the continuity equation (16), the partial derivative with respect to time t disappears in our stationary frame as well as the ones in y and z since the fluid flow is solely in the x direction ($\underline{u} = [u_x,u_y,u_z] = [u,0,0]$). We end up with the following mass conservation equation (20):

$$\nabla \cdot (\rho \; \underline{u}) \; = \; 0 \quad \Rightarrow \quad \frac{\partial(\rho u)}{\partial x} \; = \; 0 \tag{20}$$

Solving this partial derivative equation, we have a link between the pre- and post- shock conditions 21 on the mass flux:

$$\rho_1 \; u_1 \; = \; \rho_2 \; u_2 \tag{21}$$

Applying the same hypotheses to the Navier-Stokes equation of conservation of momentum, we obtain a simplified partial derivative equation (22).

$$\frac{\partial(\rho u^2)}{\partial x} \;=\; -\frac{\partial p}{\partial x} \quad \Rightarrow \quad \frac{\partial(\rho u^2 + p)}{\partial x} \;=\; 0 \tag{22}$$

Making use of the perfect gaz law ($p = \frac{\rho k T}{\mu}$), we have another equation (23) linking the density, velocity and temperature pre- and post-shock. This expression can be further simplified by using the continuity equation (21) found previously.

$$\rho_1 \left(\frac{kT_1}{\mu} + u_1^2\right) \;=\; \rho_2 \left(\frac{kT_2}{\mu} + u_2^2\right) \quad \Rightarrow \quad \frac{kT_1}{\mu u_1} + u_1 \;=\; \frac{kT_2}{\mu u_2} + u_2 \tag{23}$$

So far, we have 3 unknowns for 2 equations and the system can't be solved. To find the last equation, we will apply our hypotheses to the third equation of fluid dynamics, the energy conservation. Only one term remains as we can see in the following equation (24):

$$\frac{\partial(\rho u H)}{\partial x} \;=\; 0 \quad \Rightarrow \quad \rho_1 u_1 H_1 \;=\; \rho_2 u_2 H_2 \tag{24}$$

With the continuity equation (21), the energy conservation takes the form of the conservation of the total/stagnation enthalpy (25) in the fluid flow upstream and downstream of the contact discontinuity.

$$H_1 \;=\; H_2 \tag{25}$$

By definition, the total enthalpy is the enthalpy of a fluid obtained by isentropically decelerating it to rest. We can then express this conservation of total enthalpy in terms of temperature and velocity (26).

$$c_p T_1 + \frac{u_1^2}{2} \;=\; c_p T_2 + \frac{u_2^2}{2} \tag{26}$$

To go further, we need to introduce a few thermodynamic quantities of calorically perfect gases. The heat capacity C is defined in thermodynamics as the amount of heat that must be added to any material to induce a change of temperature of one Kelvin. We distinguish the heat capacity at constant pressure c_p and at constant volume c_v. Those two heat capacities are not independent and are linked to each other by the Mayer's relation (27) where n is the number of moles and R is the perfect gas constant. Their ratio is also of importance and is called the specific heat ratio γ (28). This ratio is widely used to describe isentropic processes in thermodynamics.

$$c_p - c_v \;=\; nR \tag{27}$$

$$\gamma \;=\; \frac{c_p}{c_v} \tag{28}$$

Making use of the Mayer's relation and the definition of the specific heat ratio, we obtain the following expression for the heat capacity at constant pressure c_p (29):

$$c_p \;=\; \frac{\gamma n R}{\gamma - 1} \tag{29}$$

Inserting (29) and using the perfect gaz law in the first term of the energy conservation equation (26), we obtain (30):

$$c_pT \;=\; \frac{\gamma}{\gamma-1}nRT \;=\; \frac{\gamma}{\gamma-1}\frac{p}{\rho} \;=\; \frac{\gamma}{\gamma-1}\frac{kT}{\mu} \tag{30}$$

Beside its definition by a ratio of heat capacities, the specific heat ratio γ also possesses a proper mathematical definition and is related to the degrees of freedom (dof) of a molecule or atom by the following relation (31):

$$\gamma \;=\; 1+\frac{2}{dof} \tag{31}$$

So far, we have treated the shock in a very general matter. The reasoning done so far allowed us to introduce the Rankine-Hugoniot relations for a steady normal shock (21,23 and 25). Those equations are valid for a calorically perfect gas and mixtures of gases in thermo-chemical equilibrium and are widely used to study shocks around a supersonic aircraft, during re-entry of a spacecraft in the atmosphere or even in space for the collision of stellar winds. To go further in our reasoning, we need identify the nature of the fluid undergoing the hydrodynamical shock. In stellar wind collision, the fluid coming from the stars is mostly made of ions coming from the surface of the massive stars. In that case, the fluid undergoing the shock is an atomic gas which means 3 degrees of freedom and thus a value of the specific heat ration γ (31) of $\frac{5}{3}$. Making use of this new information and equation (30), the conservation of total enthalpy (26) takes the following form (32):

$$\frac{5kT_1}{2\mu}+\frac{u_1^2}{2} \;=\; \frac{5kT_2}{2\mu}+\frac{u_2^2}{2} \tag{32}$$

We have now in our possession two equations (23, conservation of momentum) and (32), conservation of energy) with two unknowns for the post-shock conditions u_2 and T_2. Using the first equation to eliminate T_2, we obtain the following quadratic equation in term of the post-shock velocity u_2 (33):

$$2u_2^2-\frac{5}{2}\left(\frac{kT_1}{\mu u_1}+u_1\right)u_2+\frac{5kT_1}{2\mu}+\frac{u_1^2}{2} \;=\; 0 \tag{33}$$

This quadratic equation (33) has two solutions. The first one corresponds to the case where nothing happens to the fluid and the velocity remains the same and we don't have a shock (34). The second solution (35) represents the velocity of the fluid after undergoing the hydrodynamic shock, the case of interest since we made the assumption that a shock is present in the fluid flow (cf. Figure 18).

$$u_2 \;=\; u_1 \tag{34}$$

$$u_2 \;=\; \frac{5kT_1}{4\mu u_1}+\frac{u_1}{4} \tag{35}$$

In fluid dynamics, an interesting quantity to discuss shocks is the Mach number M which is related to the isentropic speed of sound a and is a dimensionless parameter of a fluid flow. The speed of sound and Mach numbers are defined respectively in equations (36) and (37).

$$
\begin{aligned}
a^2 &= \left(\frac{\partial p}{\partial \rho}\right)_s = \frac{\gamma k T}{\mu} && (36)\\
M &= \frac{u}{a} && (37)
\end{aligned}
$$

Inserting the Mach number of the pre-shock flow in the expression of the post-shock velocity (35), we end up with the following relation (38):

$$
u_2 = \left(\frac{3}{4M_1^2} + \frac{1}{4}\right) u_1 \tag{38}
$$

With the use of the continuity equation (21) and the conservation of momentum (23) or energy (32), we can have similar expressions for the downstream density ρ_2 and temperature T_2 linking them with their upstream quantities solely by the Mach number.

$$
\begin{aligned}
\rho_2 &= \frac{4\rho_1}{3M_1^{-2} + 1} && (39)\\
T_2 &= \left(\frac{7}{8} + \frac{5M_1^2}{16} - \frac{3}{16M_1^2}\right) T_1 && (40)
\end{aligned}
$$

As mentioned previously when discussing the stellar winds of massive stars (cf. Section 2.2), we have velocities up to 3000 km/s which correspond to a very high Mach number (M >> 1). In the case of such a strong shock, the upstream Mach number dominates the expressions of the downstream velocity, density and temperature which reduce to the relations (41), (42) and (43):

$$
\begin{aligned}
u_2 &= \frac{u_1}{4} && (41)\\
\rho_2 &= 4\rho_1 && (42)\\
T_2 &= \frac{5}{16} M_1^2 T_1 = \frac{3\mu u_1^2}{16k} && (43)
\end{aligned}
$$

With such strong shocks, the gas becomes much hotter and the shocked material can reach temperature of the order of several 10 million Kelvin ($T_2 > 10^7 K$). As for any shock, the density increases and is limited here by a factor 4 as is the decrease in velocity.

In a similar manner as for the determination of the hydrodynamic shock location, we made here a few assumptions, to facilitate the computation of the post-shock conditions and to help us understand what is happening to the fluid flow, that can be debatable. For instance, in our simple model, we neglected the presence of external force even though massive star have huge gravitational and radiative fields. The material from the wind of star 1 is submitted to the radiation pressure and the gravity of its star of origin, star 1, but also the radiation and gravity of star 2. The same can be said about the material present in the wind of star 2 and those forces have an impact on the properties of the pre-shock flow. This is especially the case in close massive binaries where the radiation coming from one star can "slow" the acceleration of the wind material coming from the other star. Even taking into account the gravity of that one star which has the opposite effect (speed up the acceleration), the radiation effect is not fully compensated and we observe a decrease in the pre-shock velocity which in turn leads to a lower post-shock temperature. This phenomenon is a limitation similar to the one we found in the location of the contact discontinuity and one of the reason the wind can't reach their terminal velocity. Another possible alteration of the pre-shock conditions has been studied by Parkin and Sim in 2013 [12] when they introduced the concept of self-regulated shocks. The idea is that the X-ray emission coming from the shocked material (post-shock) could impact the pre-shock material and further ionize it which in turn slows the acceleration of that material. On the video shown on Figure 16, we can see the evolution of the density in a colliding wind binary WR 22 that accounts for the influence of radiation pressure and the orbital motion. It is clear on this advance simulation that the simple result we found in the expression (42) is not valid and that the computation of the density is more complex than a multiplication of the pre-shock condition by four.

We can also briefly discuss here what is happening to the post-shock plasma heated at up to several ten millions Kelvin by the hydrodynamic shock. It turns out that the changes sorely depend on the efficiency of radiative cooling. Stevens & al. [12], in 1992, proposed a dimensionless parameter χ to estimate the efficiency of this radiative cooling for each star. In its expression (44), t_{cool}, t_{esc}, d and $\dot{M}$ represent respectively the cooling time, the escape time, the pre-shock velocity in 1000 km/s, the separation between the star in question and the shock in 10^7 km and the wind mass-loss rate in 10^{-7} $M_\odot$/year. If $\chi << 1$, the radiative cooling is extremely rapid and the shocked plasma radiates its energy and we end up with an isothermal wind. On the opposite, if $\chi >> 1$, the radiative cooling is not possible and the shocked plasma decreases its temperature in the wind interaction region through an adiabatic expansion.

$$\chi \; = \; \frac{t_{\text{cool}}}{t_{\text{esc}}} \; = \; \frac{v^4 d}{\dot{M}} \tag{44}$$

2.4 Why observe in X-rays

The high energy, X-ray part of the electromagnetic spectrum, corresponds to photons with a wavelength between 0.1 and 100 $\AA$ (0.1 to 100 keV in terms of energy). If we take a look at Figure 19, we can see that, in order to have photons in that specific spectral domain, the temperature of the body, a black body for Planck's law, needs to be extremely high (extremely hot bodies are required to generate X-ray photons). With increasing temperatures, we can see that the maximum of the curve, where most of the energy is radiated, is shifted to shorter wavelengths λ. The amount of energy radiated at the shortest wavelengths, extreme left side of the curve, is also increased as the black body temperature increases and the lowest wavelength at which photons are produced gets shorter and shorter with the increasing temperature.

This behavior of a black body can also be noticed by looking at Wien's displacement law (45) that follows the wavelength of maximum radiation as a function of the black body temperature. If we take our Sun, we can see that, with an effective temperature around 5800 K, the radiation is maximum at around 0.5 μm which corresponds to visible light. For the Earth, with a temperature around 300 K, it will lead to a maximum around 10 μm (infrared radiation) [36].

$$\lambda_{max}\, T \; = \; 2.898\ 10^{-3}\ [m \cdot K] \tag{45}$$

By a quick look at the black body radiation with Planck's and Wien's displacement laws, it is clear that a cosmic X-ray source must be at an extremely high temperature. By using those laws, we can deduce that a plasma producing photons in the X-ray domain is at a temperature ranging from 10^5 K

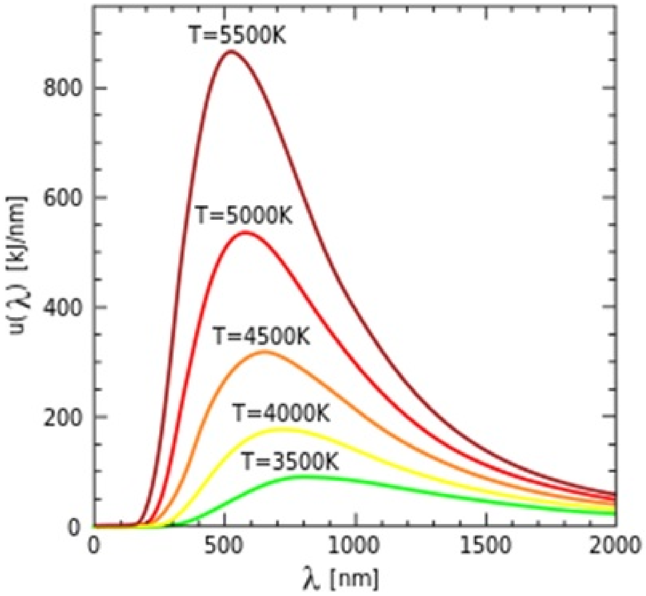

Figure 19: Black body radiation at different temperatures (Planck's law) [36].

to 10^8 K. For this thesis, we are working on the binary system HD 149 404 made of two massive stars and with the presence of a hydrodynamic shock due to the interaction between the stellar winds. In section 2.2, we have described massive stars, like the two O supergiants that make up the binary system of interest, and explained that they are among the hottest stars in the universe. Moreover, in section 2.3, we have demonstrated, starting from the Navier-Stokes equations, that a hydrodynamic shock caused by highly supersonic winds leads to shocked material reaching temperatures of the order of several 10 million Kelvin. It is then safe to say that HD 149 404 is a perfect candidate to be studied by an X-ray space telescope since, by its nature, the plasmas, within the binary system, have a high enough temperature to produce those specific photons.

We can even go deeper to justify the use of an X-ray telescope by recalling quickly the physical processes happening in such a hot plasma and resulting in the production of those X-ray photons. We have already detailed the black body radiation which can explain the emission of some cosmic X-ray sources but other processes can lead to the production of cosmic X-rays in hot plasmas. Those processes, in high energy astrophysics, are usually classified as thermal or non-thermal. A process leading to X-ray emissions is considered thermal if the distribution of energy of the free electrons follows a Maxwell-Boltzmann energy distribution law at a certain temperature. Beside the black body radiation that we mentioned earlier, thermal processes notably include Bremsstrahlung, also known as braking radiation. On Figure 20, we have a sketch representing the emission of Bremsstrahlung. In a plasma, we have free electrons that move with a velocity distribution depending on the plasma temperature. When a free electron passes close to a nucleus (ion), it is deflected by the electrostatic field of that specific nucleus. Due to this interaction, the electron's velocity is modified. As we know, charged particles that are accelerated or decelerated will emit an electromagnetic radiation that can be an X-ray photons if the total kinetic energy of the electron is high enough. This is due to the fact that the photon emitted by this process possesses an energy lower or equal to the total kinetic energy of the electron responsible for its emission ($\epsilon = h.\nu$). As we have a certain distribution of energy of the free electrons, this process will lead to emissions across the entire electromagnetic spectrum.

We have seen that electrons and nuclei can interact in a plasma but other interactions can take place as well. Indeed, a photon can also collide with a free charged particle which changes the characteristics of the photon as well as the charged particle. This process and interaction is called Compton scattering and its discovery by the physicist Arthur Holly Compton allowed him to win the Nobel Prize in physics

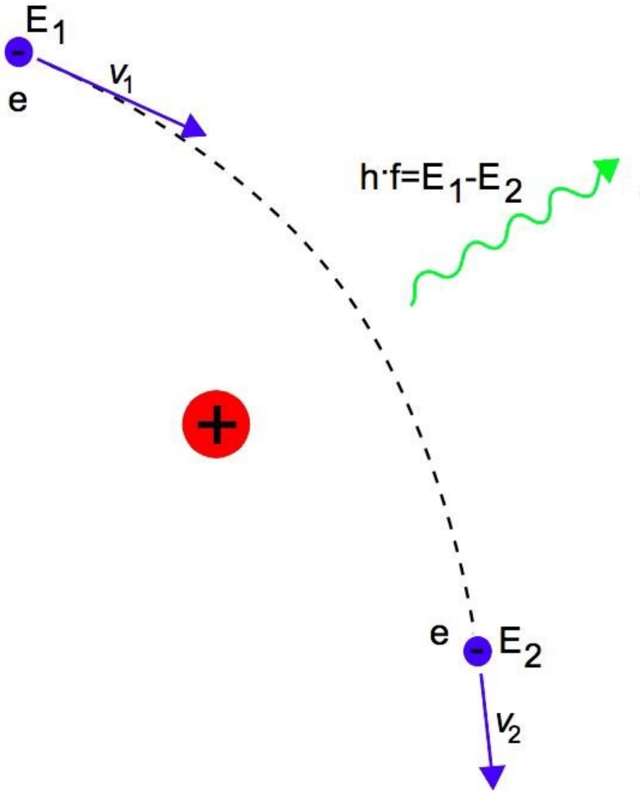

Figure 20: Bremsstrahlung, braking radiation [6].

in 1927. He discovered that the wavelength of a photon is increased when this photon is scattered by a stationary electron as represented on Figure 21. With the Compton scattering, energy is transferred from a high energy photon to an electron whose velocity is increased. In this process, this high energy photon is turned into a lower energy one which means that the radiation field is losing and transferring energy to the free electrons. This is valid for electrons at rest or with a certain velocity as long as they are not moving close to the speed of light.

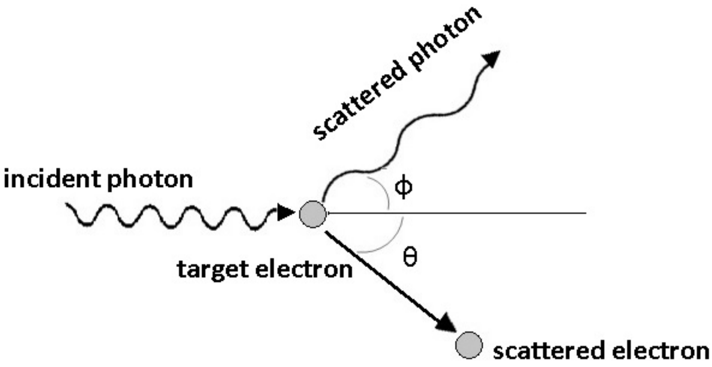

Figure 21: Compton scattering [50].

In the presence of relativistic electrons, meaning electrons at a velocity extremely close to the speed of light ($u_e \approx c$), the interaction between the photon and the now relativistic electron has a different outcome. In fact, the situation is reversed and the high speed electron scatters the low-energy photon (long wavelength), into a high-energy (short wavelength) photon. This time, the collision leads to a transfer of energy from the electrons to the radiation field. This process is called inverse Compton scattering and is represented on Figure 22 (Figure B). This non-thermal emission process is responsible for the generation of X-ray photons by transferring energy from highly relativistic electrons to low energy photons. This process can even lead to γ-ray photons if the velocity of the electron is even closer to the speed of light (the electron possesses even more energy). Here, we can clearly see that this type of emission doesn't depend on a Maxwell-Boltzmann type of distribution of energy but solely on the populations of relativistic electrons (hence the non-thermal adjective used to describe this type of emission).

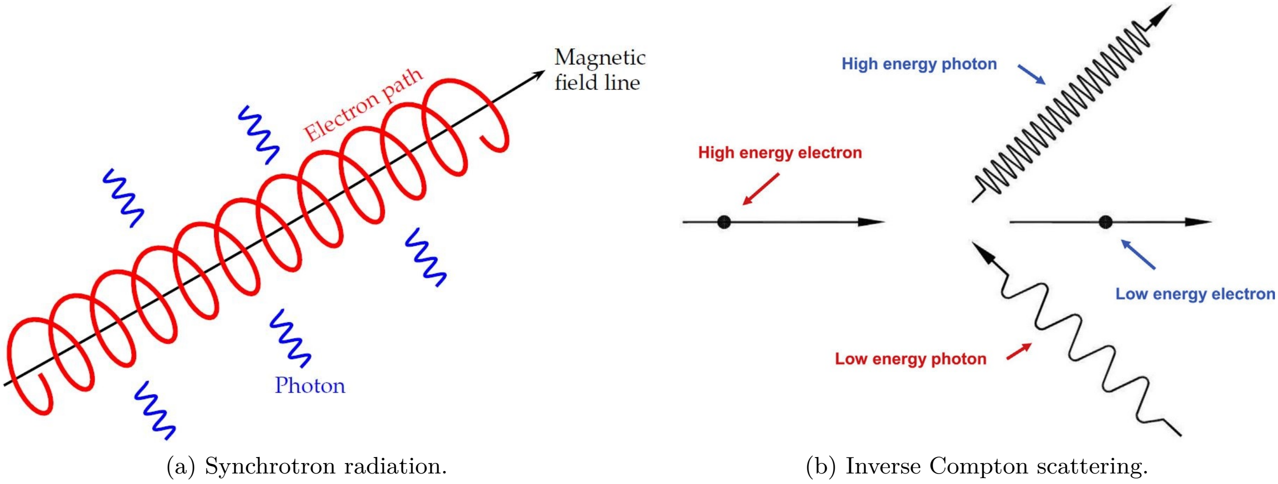

(a) Synchrotron radiation.

(b) Inverse Compton scattering.

Figure 22: Processes of X-ray photons emission [3][2].

The role of relativistic electrons in the creation of X-ray radiations is even more important because they are also involved in another process generating high energy photons: Synchrotron radiation. On Figure 22 (Figure A), we have a representation of what happens when a relativistic electron is trapped by a magnetic field line. When an electron, a charged particle, encounters a magnetic field, it is submitted to the Lorentz force which will impact its motion. Synchrotron radiations correspond to radiations emitted by relativistic electrons when they are accelerated by a magnetic field in a perpendicular direction to their motion which leads to the helix trajectory we all know from trapped particles in the Earth magnetic field. Similarly to Bremsstrahlung, the changes in direction of the relativistic electrons lead to the emission of X-ray photons since the electrons have an extremely high energy due to their highly relativistic nature. In similar fashion as the inverse Compton scattering process, the amount of X-rays produced by synchrotron radiations depends on the population of relativistic electrons.

If we look at the processes leading to the emission of non-thermal X-ray photons, we have seen that they all rely on the presence of relativistic electrons and, in particular, their number, population. Those emissions display power-law spectra which are completely different from the thermal X-ray emissions due to a Maxwell-Boltzmann energy distribution. From observations, the exponent of the power law seems to be slightly above 2 if we consider a power law distribution of the type $dN(E) \propto E^{-\gamma}dE$. The presence of relativistic particles as well as their distribution indicate that there must be some mechanism responsible for their presence and for the acceleration of electrons up to relativistic speeds. To understand this, let's imagine that such a mechanism exists and that one interaction, with this assumed mechanism, is able to increase the energy of a particle. This can be represented by a simple multiplication of the initial energy of that particle E_0 by an unknown factor β greater than 1 as shown in equation 46.

$$E = \beta E_0 \tag{46}$$

Once an interaction has taken place, the particle, whose energy is now increased, has two possibilities: undergo another acceleration/interaction or leave this region/mechanism. Let's take P as the probability that this particle remains in this region and interacts again with this mechanism. We can express the energy of a particle after k interactions as well as the number density of particles that went through those interactions, starting from an initial number density N_0, as followed (47and 48):

$$\begin{aligned} N(E \geq E_k) &= N_0 \ P^k && (47) \\ E_k &= \beta^k \ E_0 && (48) \end{aligned}$$

From the relations (47) and (48) and by expressing the number density of particles with an energy greater than E_k as an integral (49), we can go further and find an expression for the number density of particles at a certain energy E.

$$N(E \geq E_k) \ = \int_{E_k}^{\infty} N(E) \ dE \tag{49}$$

Since we are here only interested in the results that can explain the interest and reasons to use an X-ray telescope to observe the binary system, we will not give the details of the mathematical operations used to find the expression of the number density of particles but simply show the final result obtained during the High-Energy Astrophysics lectures [45] (chapter 2) which inspired this entire section and the related mathematical developments. This final result, the relation (50), corresponds to a distribution of energy taking the form of a power-law distribution which is precisely what is observed and what characterizes the processes of inverse Compton scattering and synchrotron radiations explained earlier.

$$N(E) \ \propto \ E^{\frac{\ln P}{\ln \beta} - 1} \tag{50}$$

So far we have seen that non-thermal X-ray emissions are associated with the population of relativistic electrons and that a mechanism could be responsible for the acceleration and, hence, the production of the relativistic electrons but does this mechanism truly exist? In fact, such a mechanism exists in the universe and regions in space have been identified in Astrophysics as being responsible for accelerating electrons up to relativistic speeds. We all know that solar flares, with the associated synchrotron radiations, are one site where such acceleration takes place since they are well studied and monitored due to the potential threat they represent for our high-tech societies on Earth. Other objects have also been identified such as Pulsars and active galactic nuclei (AGN). In our cases, the appropriated mechanism/phenomenon we are looking for is the hydrodynamic shock that can be caused by a Supernovae explosion but also by collision between stellar winds.

This mechanism, responsible for the acceleration of electrons from an already high-energy up to relativistic speed by a highly supersonic shock (U >> a), is called: First-order Fermi mechanism. In this context, the Rankine-Hugoniot relations (41 and 42) for a highly supersonic shock can apply to the flow and the high-energy electrons are assumed to have an initial velocity greater than the shock speed U to be able to enter the acceleration mechanism. It can be shown that a particle interacting with the shock by going forth and back, from upstream to downstream and back to the upstream flow, is accelerated and gains, on average, an energy proportional to the shock speed as described by the relation 51.

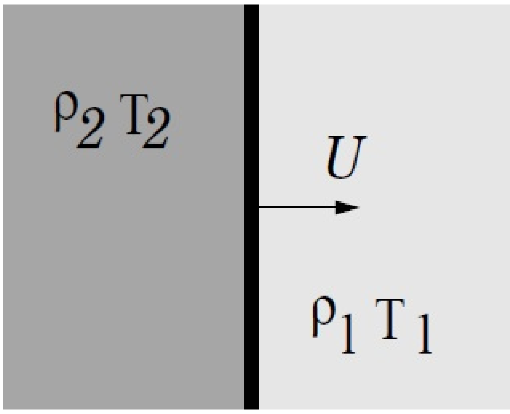

Figure 23: Strong shock (absolute frame of reference) [45].

$$\left\langle \frac{\Delta E}{E_0} \right\rangle = \frac{U}{c} \tag{51}$$

By inspecting the energy gained by undergoing an interaction with the hydrodynamic shock, we can extract the value of the energy boost β (cf. equation 46) received by the electron (52:

$$\beta = 1 + \frac{U}{c} \tag{52}$$

In a similar manner and using the Rankine-Hugoniot relations for a strong shock as well as the average velocity of a particle undergoing the interaction, it can be shown (cf. High-Energy Astrophysics lectures [45] for the full mathematical details) that the probability that a particle is coming back for more interactions and is not swept away from this acceleration region is (53):

$$P = 1 - \frac{U}{c} \tag{53}$$

Going back to the power-law distribution we obtained while discussing the possibility of accelerating electrons (50), we find that the first order Fermi mechanism, also known as diffusive shock acceleration, gives an exponent for the power law (54) extremely close to the one observed which seems to be slightly above 2. This mechanism is effective and takes place on a really short distance, the contact discontinuity, which allows for a rapid acceleration of the electrons due to a short time between two successive interactions with the hydrodynamic shock.

$$N(E) \propto E^{-2} \tag{54}$$

As it must be clear by now, the use of an X-ray telescope is the ideal choice to fulfill the goal of this work. Indeed, if we recall the title of this thesis, "Probing the wind interaction in the massive binary system HD149404 with XMM-Newton", the interest of the X-ray data stands out. Indeed, we are dealing with two massive O-type stars that produce energetic winds which can be the theater of shocks leading to an intrinsic soft X-ray emission, but will also produce a collision that can lead to even hotter plasma, emitting harder X-rays, in the wind interaction zone (cf. Section 2.3). All the conditions are in place in order to have thermal as well as non-thermal X-ray emissions by the different processes we mentioned and detailed throughout this entire section which renders the binary system HD 149404 a suitable target for an observation by the ESA X-ray space telescope XMM-Newton.

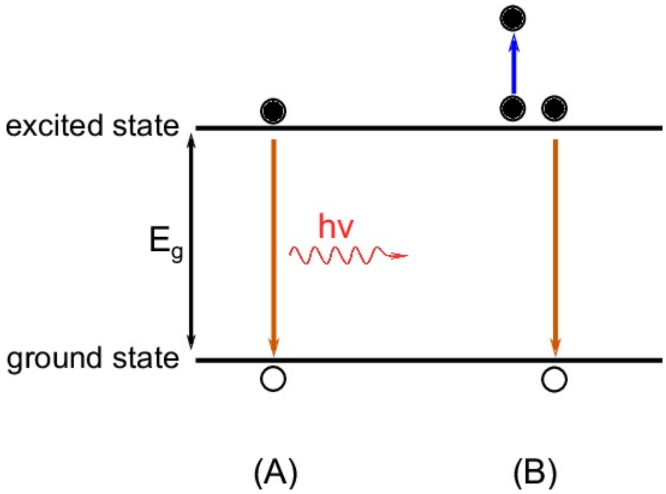

Figure 24: Radiative recombination [5].

However, it is important to state that we have mentioned a few processes and mechanisms able to produce cosmic X-rays but there are several others. For instance, we can mention processes leading to the emission of lines in the X-ray domain. Barkla discovered, in 1908, that the transition of an electron between the innermost energy levels, closest to the nuclei, can lead to the emission of an X-ray photon if the energy difference between the two electronic levels is great enough (55). In X-ray astrophysics, those transitions are designated by letters K, L, M,.. which correspond, in the modern atomic model, to specific values of the principal quantum number n (n=1 for K, n=2 for L and so on). Such lines are possible for the atomic species that we can find in the stellar wind of massive stars (cf. Section 2.2) such as Carbon, Oxygen and Nitrogen since their innermost electronic levels are sufficiently apart to emit X-ray photons while, for instance, going from an exited states back to the ground level. This is illustrated on Figure 24 where we can see on the left a radiative recombination, the exited electron returns to the ground level while emitting an X-ray photon, and, on the right, the Auger auto-ionization process, an exited ion is coming back to the ground level by emitting a photon and self ionizing by ejecting one of its electron.

$$h\nu = E_2 - E_1 \tag{55}$$

3 XMM-Newton

In order to study the binary system HD 149 404 and the shock created by the collision of the two winds, we need to observe it at different times and phases. As already mentioned in section 1, the goal was to observe the binary system at phases 0 and 0.5 to have the secondary in front and then the primary. The last observation is dedicated to the side view of the binary at phase 0.25 or 0.75. The reasons behind the choice of those three specific phases are detailed in a following section regarding the binary system and the data set itself (cf. Section 4).

In general, to observe any stars, we have two possibilities: from the ground or from space. The cheapest and easiest one is the use of a ground-based telescope such as TIGRE or VLT, respectively Telescopio Internacional de Guanajuato, Robótico-Espectroscópico and Very Large Telescope. Another unusual and fascinating option would be the use of an aircraft transformed into an airborne observatory like SOFIA, Stratospheric Observatory for Infrared Astronomy. Unfortunately, we take here an interest in the X-ray emission resulting from the violent collision between the winds from the two stars, O7.5I(f) and ON9.7I, as well as the intrinsic X-ray emission from the stars. In this specific, high-energy, spectral domain below 10 nanometers in wavelength, the protecting Earth atmosphere is absorbing all the incoming X-rays. As we can see on Figure 25, this means that the Earth atmosphere is completely opaque to that portion of the electromagnetic spectrum and we are left with only one possibility to observe any cosmic X-ray phenomenon: going to space.

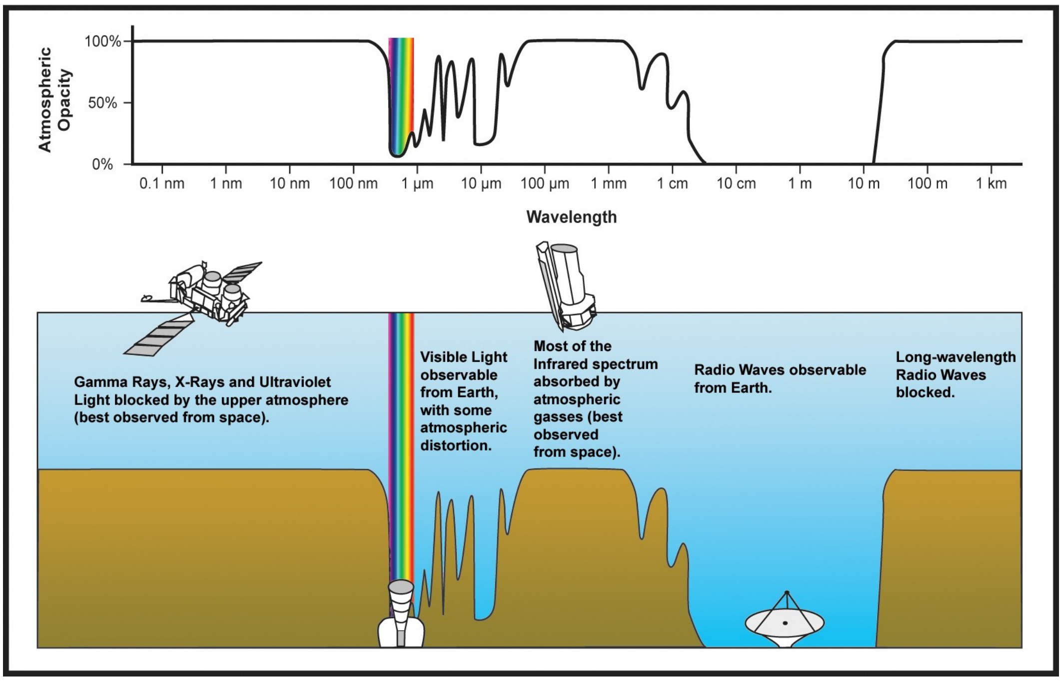

Figure 25: Earth atmospheric opacity [36].

In space around the Earth, we have, as scientists, several available X-rays telescopes with each their specific characteristics and capabilities like Chandra, NuSTAR, Swift and XMM. For this project, the collection of data on the binary system has been carried out by the ESA X-ray telescope XMM-Newton. On Figure 26, we can have an idea of the spacecraft size compared to an average person. This picture was taken in 1999 by the airbus engineers shortly before its launch by the Ariane V rocket on December 10^{th}, 1999. The spacecraft, measuring 10 meters long and weighting 4 tons, is one of the largest scientific satellite launched by ESA, the European Space Agency.

Alongside the Hubble Space Telescope and Voyager 1, X-ray Multi-Mirror Mission, better known as

Figure 26: XMM-Newton before launch [7].

XMM-Newton, is one of the most iconic scientific spacecraft to have ever been built and launched. This emblematic spacecraft is the second Cornerstone mission of the Horizon 2000 ESA programme and the most powerful X-ray telescope. The mission was designed to answer many questions about the universe reaching from the mysterious black holes over the formation of galaxies and to our origins and the origin of the Universe, where are we coming from. What makes it even more incredible and unbelievable is the fact that this space telescope is still operating more than 20 years after its launch. Still being one of the leading scientific tools to study the X-ray universe demonstrates the astonishing work performed by the scientists and engineers at the basis of this project. For a space mission, such a long lifetime is extremely rare and astronomers around the world decided to celebrate the 20 Years of XMM-Newton Discoveries by a series of conferences and meetings.

This high-energy domain allows scientists and engineers to study the universe at a completely different level. Most of the time, the X-ray sky looks completely different from the visible one as we can see on Figure 27. This picture corresponds to the ROSAT, Röntgensatellit, All Sky Survey in X-rays on the left and the corresponding optical image on the right of the sky around the famous Orion constellation. This picture illustrates the complementarity brought by the X-ray observations which trace very different physical phenomena. For the Orion's Belt we have the counter part of the X-ray source and we can clearly see them in both images but this is not always the case. If we look at the upper part of the image, in the optical, we can see the Moon while, in the X-rays, it totally vanishes. On the bottom left, we can see the brightest star in the sky, beside the Sun, Sirius also known as Alpha Canis Majoris. Here again, we can see that the star changes completely between the two pictures and this is due to the

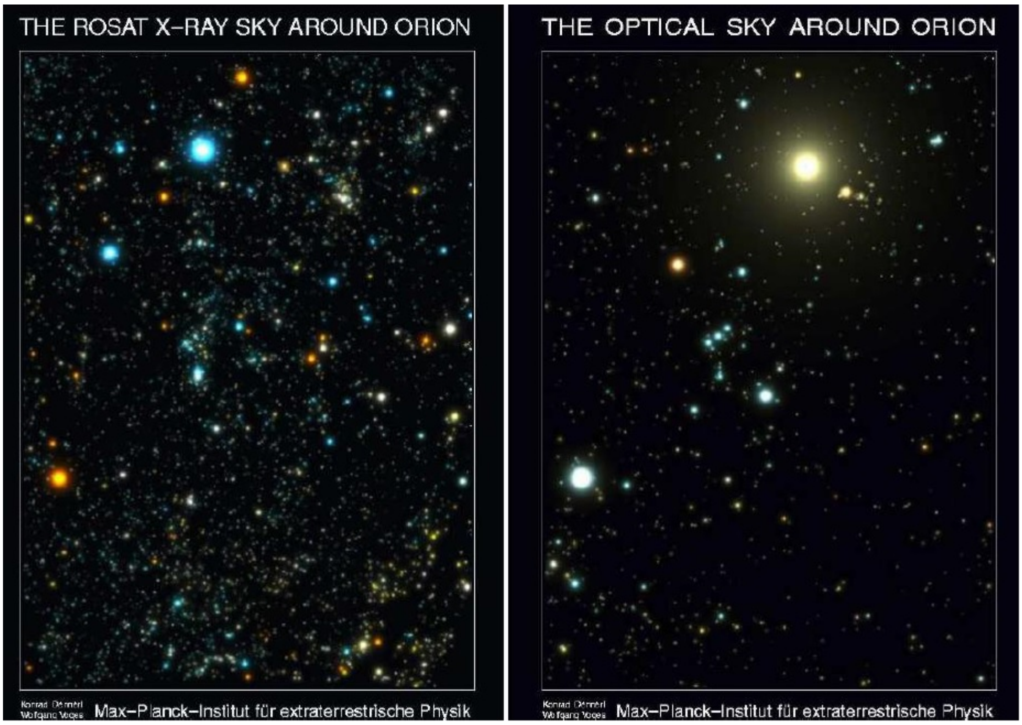

Figure 27: Visible (right) and X-ray (left) sky [45].

fact that Alpha Canis Majoris is actually a binary system. In the optical, we see the A-type star Sirius A while in the X-ray, we can only see the hot White Dwarf companion Sirius B. The rest of Figure 27 is full of similar cases and attests to the interest of the scientific world for X-ray astronomy as well as its importance in understanding our Universe.

Spectral domain	Collecting area	Effective area	Angular resolution	Field of view	Spectral resolving power
0.83-124 $\AA$	2600 cm^2	1400 cm^2 1 keV	$\leq$ 15 arcsec	30 arcmin (EPIC)	800 (RGS:0.33-2.5 keV)

Table 1: XMM-Newton specifications [45].

In X-ray astrophysics and for telescopes like XMM-Newton, one major source of hassle is the difficulty to focus X-ray photons. Unlike visible light where simple lenses or mirrors are used to focus the incoming light, X-ray photons are so small in wavelength that everything is empty to them and, most of the time, they just pass through those optical instruments as if they didn't even exist. A solution used by the XMM-Newton engineers is a reflection and a focus of those high-energy photons by what is called grazing-incidence mirrors. By tilting a regular mirror and almost aligning it with the direction of propagation of the X-ray photons, the space between the atoms of the mirror, as seen by the photon, is now small enough that the X-ray photon will undergo reflection. Having one parabolic mirror to focus the X-ray photons is physically enough but due to the extremely low grazing angle needed, it would require a very long focal length that a space telescope can't afford. To overcome this issue, the engineers placed a second hyperbolic mirror after the first one to reduce greatly the focal length needed. This type of assembly is called a Wolter type I mirror in tribute to the German physicist Hans Wolter who invented those types of telescopes. For XMM-Newton, the designers of the mission wanted to collect photons over a wide range of energies and ensure a very good quality around 7 keV. To do so, the mirror needed to have a very slight grazing angles of 30 arcmin which results in a 7.5 meters focal length [28]. To maximize the collecting area, the engineers used a special trick and, to build one telescope, they nested 58 circular mirrors with the same focal point and center. The final result of this particular design can been observed on Figure 28.

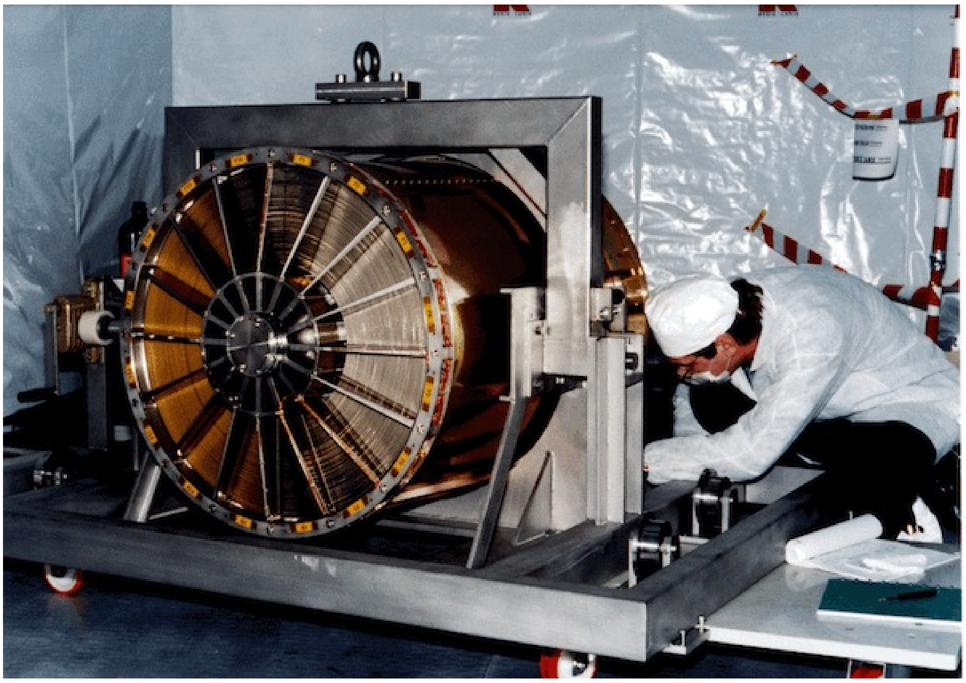

Figure 28: XMM-Newton, 58 nested shells mirrors [41].

On the final spacecraft, the designers placed three of the X-ray telescope shown in Figure 28 at the front of the spacecraft. In the front view of the X-ray space telescope on Figure 29, we can see the three Wolter type I mirrors which each have a distinct camera and detector. Above those "golden" mirrors, we have two star-trackers to ensure the pointing direction and attitude of the satellite while gathering scientific data. If we look closely to the bottom left of XMM-Newton, we can see another aperture: the Optical/UV monitor telescope. The goal is to have a classical Ritchey-Chretien telescope that is able to look at the same field of view as the X-ray telescopes. This allows to have multi-wavelength observations of almost any XMM target and ease the identification of the optical counterpart to the X-ray source if there exists one. If the target is optically too bright, like our binary system HD 149 404, the optical monitor can unfortunately not be used.

At the focal point of the three identical telescopes, there are three X-ray CCD cameras called EPIC, European Photon Imaging Camera. Two of them are perfectly identical and use the MOS, Metal Oxide Semi-conductor, technology for the CCD while the last one is different and uses the pn technology that is able to detect photons with a high efficiency up to 15 keV while the MOS is more efficient in the range between 0.2 and 10 keV [28]. From now on and throughout this thesis, we will refer to those detectors as: MOS 1, MOS 2 and PN (keeping the EPIC implied). Also specific to the MOS detectors, half the light collected by the telescopes is sent to the on-board spectrometers RGS, Reflection Grating Spectrometers (one in parallel to each MOS). Their role is to split the incoming light in a similar way of a prism and decompose the light into a spectrum. The position of the incoming photons is used to precisely determine the high-resolution X-ray spectrum while the energy of the photons, associated with the position, is used to split the X-ray spectrum into the different grating orders [45]. A global overview of XMM-Newton specifications is available on Table 1. In a following section (cf. Section 4), we will detail the different operating modes and filters of all those instruments and the ones we decided to use for this specific project. We will discuss our specific data set and see if the spacecraft was able to operate in nominal condition during the observation. We will also go a bit deeper on the working principle of EPIC and how we can use those properties to reduce the raw data obtained during the acquisition phases.

Figure 29: XMM-Newton at Cité de l'espace [43].

4 The Dataset

In order to have the opportunity to use XMM-Newton for a scientific observation, it is required to write a properly motivated proposal to ESA during one of the XMM-Newton announcement of opportunity. Indeed, XMM-Newton is an extremely busy scientific spacecraft and there are many more observation requests than what can be achieved. Stated otherwise, to fulfill all the requests for observing time, between 6 and 8 times more time would be needed than what is available, even though XMM-Newton is operated in a highly optimized way. Therefore, only the best scientific proposals are selected by the XMM-Newton Observing Time Allocation Committee, OTAC [26], while the rejected proposals will have to wait a new announcement of opportunity to try their chance again which gives them time to improve their request. The framework of writing a proposal is very specific and all the required documents and rules can be found on the ESA website [25].

During the XMM-Newton seventeenth announcement of opportunity, AO17, the Liège group of high energy astrophysics, led by professor G. Rauw, wrote a proposal entitled :"Constraining the properties of the post-RLOF massive binary HD149404" (ESA proposal ID 082051 to introduce in reference [31] to get the proposal). The idea behind the requested observations was to study the binary system HD 149 404 that had experienced a Case A Roche lobe overflow episode [9]. The objective of their project was to constrain the orientation of the orbital plane of the binary system and check the inclination range obtained based on the BRITE data [13] as well as probe the properties of the stellar winds of both components [44]. As far as the wind interaction zone is concerned, it will be modeled based on the semi-analytical formalism of Canto [14] as previously used during the study of the binary system HDE 228 766 by G. Rauw & al. [11]. The proposal was also motivated by stating that only a few massive binary systems, which are in a post Case A Roche lobe overflow stage, have been properly studied. X-ray observations could shed new light on the properties of this short-lived and poorly understood step in the evolution of massive binary systems. To correctly study HD 149 404 and achieve the scientific goals, they proposed to realize three distinct observations with XMM-Newton of the system: one at each conjunction phase (stars aligned with the line of sight, ϕ equal to 0 and ϕ equal to 0.5) and one at quadrature phase (stars aligned perpendicularly to the line of sight, ϕ equal to 0.25 or 0.75).

This proposal was accepted by the by the OTAC for AO17 and the three observations were conducted during XMM-Newton revolutions 3422, 3426 and 3428 [29]. A summary of the observation parameters and XMM-Newton instruments set-up can be found in Table 2.

ID number	0820510401	0820510501	0820510601
XMM revolution	3422	3426	3428
Scheduled Start Time	2018-08-16 05:23:42	2018-08-23 17:02:34	2018-08-28 14:42:55
Scheduled Stop Time	2018-08-16 14:08:42	2018-08-24 03:10:54	2018-08-28 22:29:35
Scheduled Duration [s]	31500	36500	28000
Window (Mos and PN)	Full frame	Full frame	Full frame
Filter	Thick	Thick	Thick
Observation Start Time	2018-08-16 05:41:08.000	2018-08-23 17:19:59.000	2018-08-28 15:00:20.000
Observation Stop Time	2018-08-16 14:08:03.000	2018-08-24 03:10:16.000	2018-08-28 22:28:58.000
Observation Duration [s]	30415	35417	26918
Phase of HD 149 404 ϕ [/]	0.25	0.0	0.5

Table 2: XMM-Newton three data sets/observations summary of HD 149 404.

Each observation made by XMM-Newton can be identified by a unique observation ID which allows scientists all over the world to access those data once available in the XMM-Newton Science Archive [31]. On this website, it is possible to download all the public data acquired during the observations and even get some rough information such as the XMM-Newton field of view of the target for the different instruments (cf. Figure 30 for field of view during the first observation). Due to the magnitude of this specific target ($m_V = 5.5$ [44]), the Optical Monitor of XMM-Newton had to be shut down to prevent any damage and a thick filter ought to be used on the telescope to remove the optical and UV light coming from the source [22] which will result in a loss of photons in the soft X-rays (low energy) as shown on Figure 33 in Section 5.

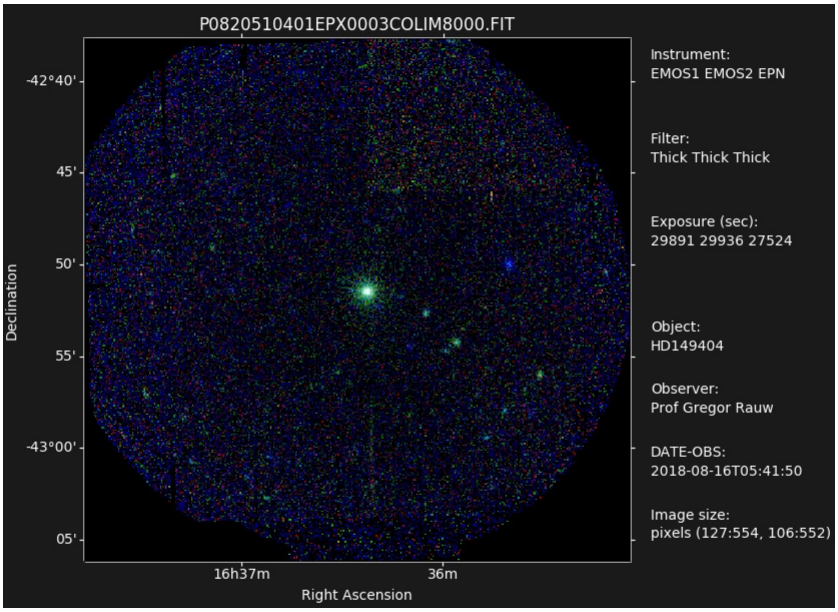

Figure 30: XMM-Newton field of view during revolution 3422 (Mos 1, 2 and PN combined) [31].

During the data acquisition phases, the EPIC cameras, both Mos and the PN, were operated in imaging mode with a full frame window (cf. Figure 31). In this specific mode, the entire CCDs, all the pixels, are read during the read-out sequence which gives access to the entire field of view of XMM-Newton. For each MOS CCD, this means a frame of 600 by 600 pixels with a time resolution of 2.6s. Imaging mode implies that the impact of a photon on the CCD, hence the creation of a certain amount of free electrons, is recorded in a list of so-called events with information regarding the event coordinate on the CCD (pixel), the pattern number (cf. Section 5) as well as the corresponding energy [27]. Those files, among plenty others such as the spacecraft telemetry, are transmitted to the user as a full set of XMM-Newton data files called observation data files (ODF) [48]. Those files include raw event lists for each CCD of each camera, instrument housekeeping files as well as spacecraft files, all in the FITS format. The FITS format, Flexible Image Transport System, is the standard data format used in astrophysics and is endorsed by the International Astronomical Union. From a user point of view, each file is simply a table, a list representing the data as well as keywords describing the instrument and detector states (filter, window mode and so on...). For instance, the file "3428_0820510601_M1S00110IME.FIT" stands for the observation 0820510601 during XMM-Newton revolution 3428 and describes the list of events in imaging mode (IME) occurring for the MOS 1 camera (M1, instrument number S001) and, in particular, the first CCD (code 10).

On Table 2, we can also see that the scheduled observation times and durations were not respected and that the real observation lasted less than predicted. This delay in the acquisition process is quite common and can be due to many reasons such as a pointing stability issue. Nevertheless, we can see that the difference, between the actual observation times and durations, is relatively small which means that the data we have effectively match the different states of the system we wanted to observe. In our case, taking into account the ephemeris of HD 149 404 [10] [44], the observation 0820510401 should account for the binary system close to phase ϕ 0.25, observation 0820510501 close to phase ϕ 0.0 and, finally,

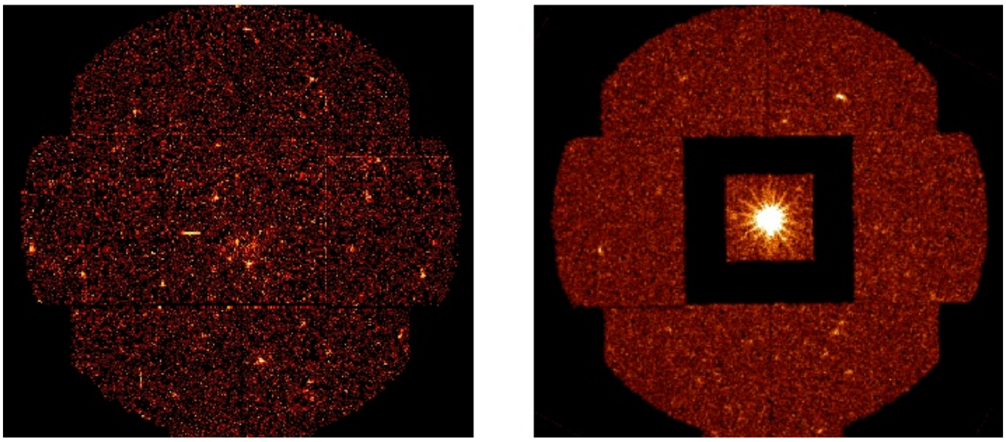

Figure 31: Full frame mode (right) and large window mode (left) of EPIC MOS[32].

observation 0820510601 should observe the system during phase ϕ 0.5. The binary system is not exactly observed at those phases but close to them owing to the uncertainties in the computed ephemeris [10] and to the motion of the stars themselves over the integration time (we do not observe a static system but a dynamical system with a period close to 10 days).

5 Data Processing

In this section, we will see how we can turn raw X-ray data obtained by XMM-Newton into usable data that can be fitted with a spectral model. This process is called data reduction and will be performed on the three distinct data sets we have at our disposal for this project (cf. Section 4 [29]). In the following, we will refer to them as rev3422, rev3426 and rev3428 which corresponds to the number of revolutions of XMM-Newton when the data were acquired rather than their official identifiers for simplicity reasons (official observation identifier for rev3422: 0820510401). The data reduction process will be divided into multiple steps and, if a step is identical for each data set, no distinctions will be made between them. However, if a step is different for one observation such as in the case of an increase in solar activity during that observation, we will, at that point, clearly state the differences in treatment between the three observations.

5.1 Data Reduction

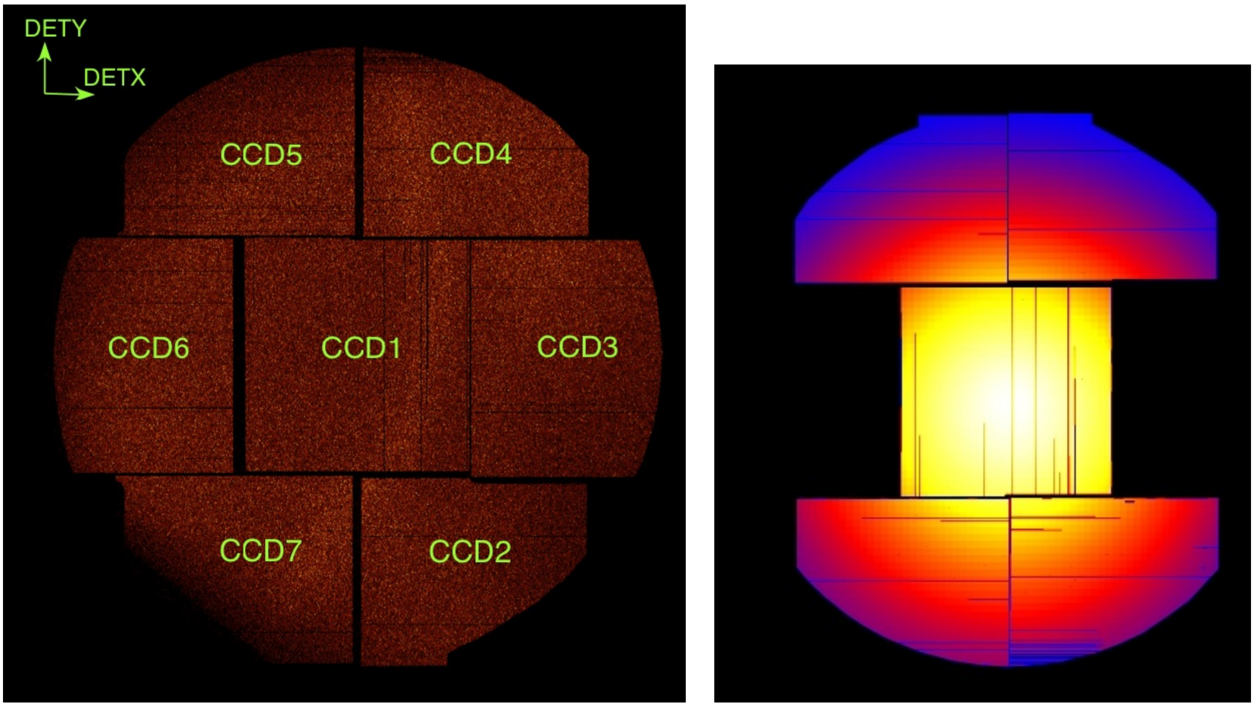

(a) Epic MOS 1 at launch.

(b) Epic MOS 1 at this time.

Figure 32: XMM-Newton EPIC MOS1 configuration. The left panel illustrates the mosaic of 7 CCDs shortly after launch. The right panel illustrates an exposure map taken these days. Due to two micrometeorite events, two of the peripheral CCDs have been lost. [21] [23].

The data reduction process is performed on the computer "rayonzix" located on the third floor of the department of Astrophysics, Geophysics and Oceanography (B5C) of the university of Liège which is dedicated to high energy astrophysics. This computer is able to remotely connect to a server "Gaphix" which possesses all the required software and files to reduce and analyze the raw data sent by the XMM ESA team. Those raw data, the Observation Data Files (ODF), communicated by ESA will be treated by the XMM-Newton Science Analysis System, SAS, a software developed by ESA scientists at the XMM-Newton Science Operations Center (SOC) and Survey Science Center (SSC). SAS, to quote its developers, is: "an extensive suite of software tasks developed to process the data collected by the XMM-Newton Observatory" [48]. The end goal is to produce calibrated event lists by, for instance, discarding bad events and correcting for the instrument response itself (redistribution matrix file, rmf, and ancillary response file, arf). All those steps, leading to the ability for us to exploit those data to study our target

HD 149 404, will be detailed and thoroughly explained as we go through the data reduction process. This data reduction process is carried on the latest SAS release which is identify by a version (18.0.0) and a build identifier (xmmsas_20190531_1155). This means that the treatment done to the data will be done with the latest updates and developments as well as bug fixes, all included to improve the quality of the reduced data.

To work properly, the Science Analysis System requires two things: the Observation Data Files (ODF) already mentioned and the Current Calibration Files (CCF). In fact, beside the data, those calibration files are mandatory to transform those raw data into usable data representing the real X-ray flux entering the telescope. Before being launched into space more than 20 years ago, XMM-Newton telescopes and instruments were tested in a specialized laboratory like any instrument designed to operate in space. The goal of those tests is to be able to reconstruct the real flux entering the telescope solely based on the information given by the detectors, here the CCDs. Without this information about the instrument response, we can't inverse the problem and the "flux" we observed at the exit of the CCD is a convolution between the real flux entering the telescope and all the effects due to the instruments themselves which can't be used to extract properties of the sources emitting those X-rays. Just looking at the EPIC MOS CCD quantum efficiency on Figure 33, we can see how complex this can be and how it depends on the energy. On XMM-Newton, they also use filters to prevent the impact of UV and optical light on the CCDs to avoid their detection which, unfortunately, alters the sensitivity of the CCD to soft X-rays as we can see on Figure 33. This problem is even more complex since, with time and the aging of the instruments, this efficiency changes and the overall quality decreases due to the harsh space environment. Beside the changes in the efficiency of the detectors, other events can cause issue to the mission and its ability to correctly detect incoming X-ray photons such as a defective pixel or, even worst, a defective CCD. This is not science fiction and really happens to space telescope as we can see on Figure 32 where we have a comparison between an EPIC MOS shortly after launch in almost perfect condition and the recent picture via an exposure map of the current state of EPIC MOS 1. The first thing that jumps to the eyes is the complete loss of two CCDs (CCD 3 and CCD 6 of the EPIC MOS 1). The loss of the CCD 6 is related to an event occurring during revolution 961 on March 9 2005 and for CCD 3, an event during revolution 2382 on December 11 2012. Both events were attributed to the impact of micrometeorites on the detectors that significantly damaged them and required them to be shut down due to not being usable anymore. The combined effect of those two events is a 28% loss of EPIC MOS 1 capability and a complete loss regarding the X-ray sources located on those parts of the focal plane. This is important to take into account for us since we are dealing with data coming from revolution 3000+ where those CCDs were already out of service. However, we will see that, fortunately for us, the source and target of interest HD 149 404 was located almost on axis which corresponds to CCD 1 on Figure 32 as far as EPIC MOS 1 and 2 are concerned. The similarity between the two MOS detectors is a strength for XMM-Newton since CCD 3 and 6 are still working on MOS 2 and so the source located in those regions can still be processed by scientists. On Figure 32, we can also note several black lines on EPIC MOS 1 on the 5 remaining CCDs. They correspond to defective pixels which block the CCD read-out sequence. If we image a line of pixels on a CCD, when a pixel on that line is defective, during the read-out, the information (electrons) can't transit on that dead pixel and all the information on the pixels before (upstream of the read-out sequence) are completely lost. Depending on the position of that defective pixel along the read-out line, the amount of pixels that won't be able to be read can vary from a single pixel if the last one is defective up to an entire line if the first pixel is concerned which explains the different lengths of the black lines on Figure 32.

From those few examples, we understand the necessity to have calibration files corresponding to the exact moment, the date when the observation took placed. Those files are called Current Calibration Files (CCF) which are distributed separately from SAS and available on the official XMM-Newton website of the Science Operations Center (SOC). They are updated regularly and continuously by the ESA team as well as the International Astrophysical Consortium for High Energy Calibration, IACHEC [1], whose objective is to provide standards for high-energy astrophysics calibration and cross-calibration

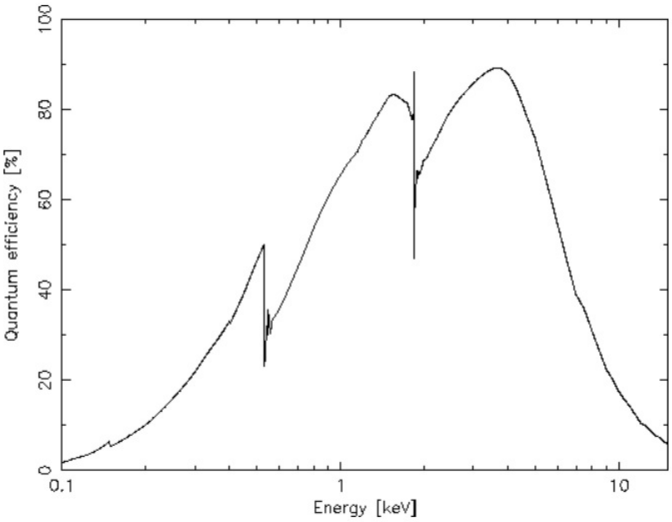

(a) Quantum efficiency of the MOS CCDs.

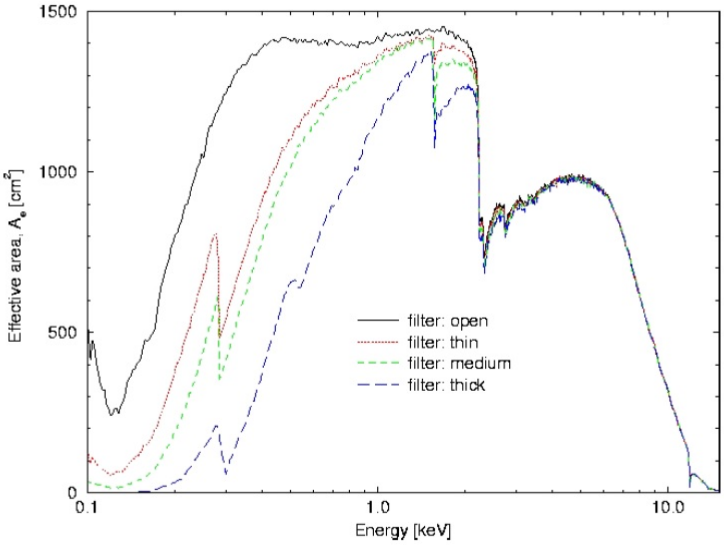

(b) EPIC effective area with different filters.

Figure 33: EPIC MOS, CCDs characteristics [45] [24].

between the various X-ray space telescopes such as NuSTAR and Chandra. This constant monitoring is done, for XMM-Newton, during a program called: "XMM-Newton Routine Calibration Programme" [30] which monitors the performances of all the scientific instruments on-board of the spacecraft by regular observations of well-known targets in such a way that the changes are assumed to solely come from the instruments and not the source itself. During those missions, multiple targets, such as HR1099 or SNR 1E 0102.2-7219, are used for the different instruments and functionalities of the spacecraft (Detector Response, Effective Area and so on...). For all the above reasons and before considering reducing the raw data communicated by the ESA XMM-Newton's team, we have to build a file, pointing towards all the CCF appropriate to our observations, called Calibration Index File (CIF) 1. For the observation time, the start of the target observation will be taken which corresponds to the 28th of August 2018 at 2:42 PM for the observation rev3428.

```
cifbuild append=no calindexset='ccf.cif' category='XMMCCF' \
ccfpath='/import/gaphe/datar2/gr/ccf/' fullpath='yes' \
withobservationdate=yes observationdate="2018-08-28T14:42:55"
```

Listing 1: Building CCF index file (rev3428)

Once this Calibration Index File has been created, we can continue to prepare SAS to treat our X-ray data by creating a file that will play the role of summary of the observation and contain the path to the data provided as Observation Data Files (ODF). In this ODF summary file, we also gather the different parameters, such as the instruments characteristics (filters, windows, identifier of each instrument and CCD and so on...) and the exposure time detailed in Section 4, that are required in order for SAS to correctly process the data. Just like the CIF, for each observation (rev3422, rev3426 and rev3428), one ODF summary file must be created using the following command 2:

```
odfingest odfdir=/import/gaphe/datar/sl/HD149404/0820510601/odf
setenv SAS_ODF 3428_0820510601_SCX00000SUM.SAS
```

Listing 2: ODF Summary File (rev3428)

At this point, the set-up of SAS is finalized and the data coming from XMM-Newton can begin to be processed and reduced. It all starts with a series of two simple commands 3 from the "epicproc" package of SAS [48]. This specific package contains two very similar tasks emproc for the EPIC MOS 1 and 2 data as well as epproc dedicated to the processing of the EPIC PN data. This pipeline processing is able, with the CIF and ODF summary file just created, to process and turn the raw Observation Data Files into a calibrated list of events (X-ray photon impacting the detectors) for each detector. This process is also able to identify Bad Pixels for each CCD on every detector which leads to 5 files for MOS 1, 7 for MOS 2 and 12 for the EPIC PN. Those simple commands allow us to turn the output of all the CCDs on one detector into a list of photons impacting the entire detector that can be used as input files to extract relevant scientific information.

```
 emproc
 epproc
```

Listing 3: EPIC Pipeline Processing

Now in possession of a calibrated list of events, we need to sort those events and make the distinction between a good event and a bad one such as a corrupted event or the impact of a cosmic ray. This step, called "grade filtering" is available in the listing 4 and is similar for both MOS detectors (similar filtering criteria) while stricter for the EPIC PN, hence the two evselect operators shown on the listing. This filtering process is performed event by event and based on criteria regarding the Grade/Pattern of the impacting photon on the CCD and a set of pre-defined screening parameters (#XMMEA_EM for MOS and a stricter one for PN FLAG==0). The pattern criterion, Figure 34, corresponds to the generation of free electrons upon a photon impact on a CCD. In fact, when an X-ray photon impacts the CCD, in one pixel, the amount of free electrons generated will be above a predefined threshold and trigger the count of an X-ray photon (orange pixel). A box is then defined around that pixel and the adjacent pixels are either above the threshold (green) or not (white) which corresponds to the way the photon impacted the CCD and its energy was spread over several pixels. The pattern depicted within that box corresponds to a certain probability that it is associated with the arrival of an X-ray photon. Furthermore, a pulse height and a pulse invariant (PI) are assigned. The PI measures the total number of free electrons generated by the arrival of the photon corrected for the charge transfer inefficiency of the CCD. This quantity is needed to reconstruct the energy of the incoming photon. Based on ground tests and calibrations of the imaging mode of the detectors, it was established that events, up to a pattern of twelve, correspond to the good events with an accurate representation of the energy of the X-ray photon. For the EPIC PN, the same pattern, between 0 and 12, criterion can be used, however, it was established that a stricter pattern criterion should be used and that patterns up to 4 (only 2 pixels involved) should be the only ones kept if a spectral analysis was performed once the data will be reduced [48]. This is due to the fact that those specific patterns of the EPIC PN detector are especially well calibrated and so a little trade-off is made here in order to have the highest quality data for the analysis and spectral fitting part of this work. As for the screening criterion, its role is to remove bad events such as events recorded during pointing stability issues, while the target was seen through the Earth's atmosphere or even cosmic ray events. In a similar manner as for the pattern criterion on the EPIC PN detector, a stricter screening criterion is used here as well and takes the form of "FLAG == 0" instead of "#XMMEA_EM".

```
MOS routine:
 evselect table="3428_0820510601_EMOS1_S001_ImagingEvts.ds:EVENTS" \
 expression="#XMMEA_EM&&(PATTERN<=12)" withfilteredset=true \
 destruct=true filteredset="3428_m1filt0_12xmmea.fits" keepfilteroutput=true

PN routine:
 evselect table="3428_0820510601_EPN_S003_ImagingEvts.ds:EVENTS" \
 expression="(FLAG==0)&&(PATTERN<=4)" withfilteredset=true \
 destruct=true filteredset="3428_pnfilt0_4flag0.fits" keepfilteroutput=true
```

Listing 4: Grade Filtering MOS and PN (rev3428)

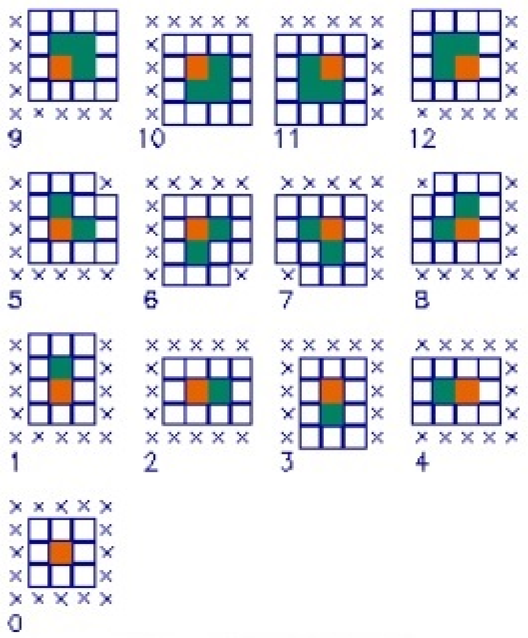

Figure 34: EPIC MOS list of acceptable patterns [48].

After getting rid of all the bad events thanks to filtering criteria, we need to inspect the remaining data and events and look at the background activity. Indeed, as mentioned in the introduction (cf. Section 1), our Sun has a "bad habit" of producing flares. The low-energy protons ejected during those flares can reach the X-ray detectors and produce a background flare that can seriously impact the quality of the X-ray data while still not being filtered in the previous step. This background check needs to be done based on the filtered data from the previous step and with new criteria. Actually, the solar activity, even with low-energy protons, is best seen on the harder side of the X-ray domain of XMM-Newton which corresponds to a pulse invariant above 10 keV. To find out if the background, in particular our Sun, affected the data, an histogram of the hard X-rays as function of time is computed. For such a curve, we bin the events on 100s intervals, we filter the data with the pulse invariant criterion to keep the hard X-rays and we apply a criterion to select only the pattern 0 corresponding to single pixel events. The pattern 0 is there to minimize the effect of Pile-up, more than one photon impacting the pixel during a read-out cycle, and ensure that the extracted light-curve corresponds to single events as prescribed by the SAS user guide [48]. As mentioned, the PI criterion is there to only account for the hard part of the X-rays and, for the EPIC PN, an upper limit of 12 keV is recommended to avoid noisy pixels. Finally the binning part is there to ensure that we have enough photons per interval in the graph (the 100 seconds bins are also recommended for filtering high background periods). All the criteria and code associated to the extraction of this single event light-curve can be found on Listing 5 after the evselect command. The dsplot command is there to simply plot the curve for a visual inspection and the light-curve for revolution 3426 and 3428 can be found on Figure 35.

```
MOS routine:
 evselect table="3428_m1filt0_12xmmea.fits:EVENTS" withrateset=true \
 expression="(PI>10000)&&#XMMEA_EM&&(PATTERN==0)" maketimecolumn=true \
 rateset="3428_m1hard.fits" timebinsize=100 makeratecolumn=true

 dsplot table=3428_m1hard.fits withx=YES x=TIME withy=yes y=RATE

IF FLARE ADD:
 tabgtigen table=3428_m1hard.fits gtiset=M1GTI.ds expression='RATE<0.3'

PN routine:
 evselect table="3428_pnfilt0_4flag0.fits:EVENTS" withrateset=true \
 expression="(PI>10000&&PI<12000)&&#XMMEA_EP&&(PATTERN==0)" maketimecolumn=true \
 rateset="3428_pnhard.fits" timebinsize=100 makeratecolumn=true

 dsplot table=3428_pnhard.fits withx=YES x=TIME withy=yes y=RATE

IF FLARE ADD:
 tabgtigen table=3428_pnhard.fits gtiset=PNGTI.ds expression='RATE<0.5'
```

Listing 5: Light curve for background flaring detection (rev3428)

Upon visual inspection of those light-curves, we can clearly see that there is a major difference between revolution 3426 and 3428 (rev3422, not shown, is similar to rev3428). For rev3428, the count rate/light-curve looks similar to white noise during the entire time of the observation while a clear peak is visible for rev3426. In high-energy astrophysics, a white noise like single event light-curve is a trustworthy sign of a stable (and hopefully low) background level during an observation. This means that the presence of a peak with such a high count rate during revolution 3426 is a clear sign that our observation was impacted by an increase in the solar activity. However, happily for us, the duration of that high background activity is relatively short and the data from rev3426 can be used at the condition of removing the events occurring during the increased solar activity. To get rid of those contaminated data, a special command tabgtigen is used (cf. Listing 5). The role of this command is to create a special file containing the so called Good Time Intervals (GTI file) based on a count rate criterion making the distinction between High and Low background activity. Even though the recommended values are 0.35 and 0.4 counts per second for the MOS and PN respectively, they heavily depend on the objective of the study, the data themselves and the type of source. For those reasons, a criterion of 0.3 counts per second is applied for the MOS detectors and of 0.5 for the EPIC PN which basically match the highest value of the single event light-curve of rev 3422 and 3428 (MOS and PN respectively). Those GTI files will serve later on as a criterion to discard events that were recorded during a high background episode and are only necessary for the data of rev3426 since the other two observations were done under low background conditions as we can see on Figure 35.

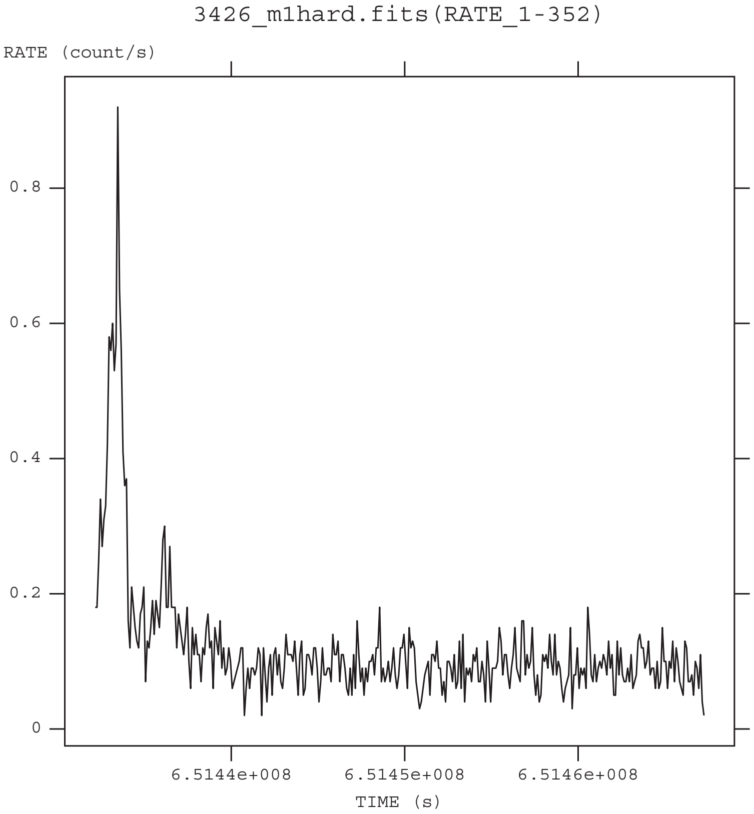

(a) Revolution 3426.

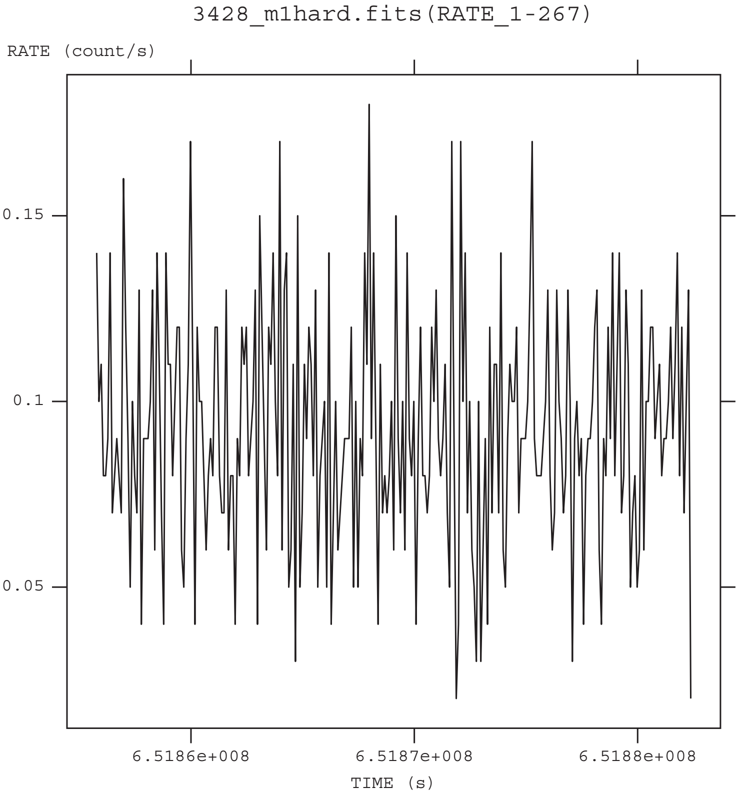

(b) Revolution 3428.

Figure 35: Single Event Light-Curve (MOS 1).

Once the background issue identified and solved, we can continue the reduction process and identify the sources located in the field of view of XMM-Newton during the observations, the end goal being to find our binary system HD 149 404. The first step in identifying sources is to create an image of the field of view of XMM-Newton. An image is produced for each cameras, the 2 MOS as well as the PN, and for each observations (rev3422, rev3426 and rev3428) thanks to the evselect command by inputting the filtered events list and several parameters. Unlike the single event light-curve, we need to bin here in terms of pixel coordinates in the sky (field of view of XMM-Newton) and not the time. In our case, we bin in the X and Y directions in 20 units with one unit representing 0.05 arcsec in the sky frame which allows us to extract clear images. For the subsequent creation of an energy-coded image, we also impose a PI interval for the events that will serve as basis for the image creation process. The lower 300 eV limit is there to clean the image and remove the parasitic low pulse height events while the higher limit match the end of XMM-Newton capability at 10 keV. The listing (6), corresponding to this first step of source identification, is only representing the MOS 1 camera of rev3428 but remains valid for the other cameras of rev3428 and rev3422 since they were not impacted by a high background (a simple change of the file name in the "imageset" parameter is the only change required to deal with the other data of rev3428 and rev3422).

```
evselect table="3428_m1filt0_12xmmea.fits:EVENTS" imagebinning="binSize"
imageset="3428_m1img.fits" \
withimageset=yes xcolumn="X" ycolumn="Y" ximagebinsize=20 yimagebinsize=20 \
expression="(PI in [300:10000])"
```

Listing 6: Source detection part 1 without flaring background (rev3428)

However, as we have seen previously, revolution 3426 was impacted by a high background activity during the first part of the data acquisition process and events recorded during that time interval need to be discarded. To do so, in addition to the PI criterion, an additional criterion is imposed on the event list. This specific criterion is making use of the GTI files created during the background inspection step (cf. Listing 5) and will make sure that any event used in the generation of the field of view image were acquired at a time of low background. This new criterion can be seen in the code specific to revolution 3426 in Listing 7.

```
evselect table="3426_m1filt0_12xmmea.fits:EVENTS" imagebinning="binSize"
imageset="3426_m1img.fits" \
withimageset=yes xcolumn="X" ycolumn="Y" ximagebinsize=20 yimagebinsize=20 \
expression="(PI in [300:10000])&&GTI(M1GTI.ds,TIME)"
```

Listing 7: Source detection part 1 with flaring background (rev3426)

At this stage, we have in our possession 3 images per observation that only contain good events. On Figure 36, we can see what a field of view image looks like for the EPIC PN camera during revolution 3428. On this picture, we can clearly see different sources of various sizes by simple visual inspection which is going to be the second and final step in the X-ray sources detection. Even though they are visible on the picture, we are not going to manually detect them but rather use one of the Science Analysis System most important tools: edetect_chain. By using the images just generated, the filtered list of events and the telemetry of XMM-Newton during the observation, this command will scan the images for sources with a roving box. One of the input, the telemetry file "AttHk.ds", is actually a by-product of the pipeline processing and contains the attitude of the satellite during the data acquisition process which is used to convert CCD coordinates into celestial ones. The complete code on Listing 8 contains the source detection part after the edetect_chain command where the remaining parameters such as

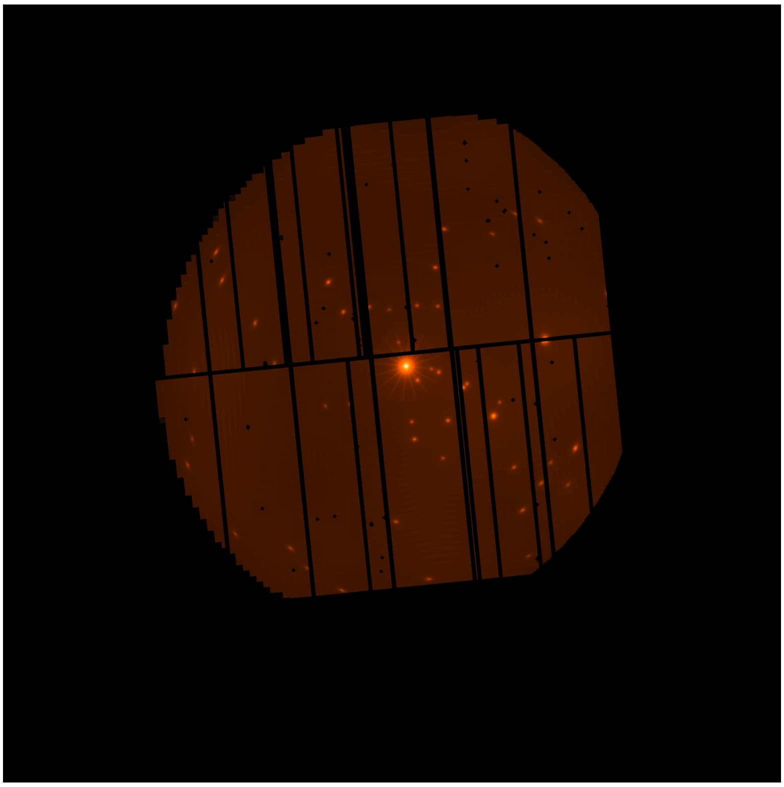

Figure 36: Field of view of EPIC PN (rev3428).

"likemin", detection likelihood threshold, and "ecf", energy conversion factors, are kept at their default values which imply that the source detection method will not give relevant information such as the sources X-ray flux but solely the position of the source in celestial coordinates, what we are looking for at this stage. To visualize the outcome of this command, an image combining the three instruments can be created using the emosaic command and the different sources can be represented by circles on top of this mosaiced image thanks to the srcdisplay command to finally achieve the result shown on Figure 37. As we can see, the XMM-Newton field of view, while being centered on the bright source HD 149 404 as we will see later, still contains many other X-ray sources that could be of scientific interest. Indeed, in astrophysics, it is not so rare that a source other than the one of interest for a given observation brings valuable scientific information. This is exactly what happened, for instance, during a performance and verification phase of INTEGRAL in 2002 focusing on Cygnus X-1 that allowed P. Goldoni to study Cygnus X-3, while the star was at 9° from the pointing direction, and write a scientific paper published in Astronomy & Astrophysics in 2003 called :"First results of IBIS/ISGRI Cygnus X-3 monitoring during INTEGRAL PV phase" [16].

```
edetect_chain imagesets=""3428_m1img.fits" "3428_m2img.fits" "3428_pnimg.fits" " \
eventsets=" "3428_m1filt0_12xmmea.fits" "3428_m2filt0_12xmmea.fits"
"3428_pnfilt0_4flag0.fits""  attitudeset="3428_0820510601_AttHk.ds" \
pimin="300 300 300 " pimax="10000 10000 10000"  ecf="1. 1. 1." \
eboxl_list="3428_eboxlist_l.fits" eboxm_list="3428_eboxlist_m.fits" \
esp_nsplinenodes=16 eml_list="3428_emllist.fits" esen_mlmin=2.3 \
likemin=10 eml_fitextent=no eboxl_likemin=10 eboxl_likemin=10
```

```
emosaic imagesets='3428_m1img.fits 3428_m2img.fits 3428_pnimg.fits' \
mosaicedset=mosaic.fits
```

```
srcdisplay boxlistset=3428_emllist.fits imageset=mosaic.fits \
sourceradius=0.01
```

Listing 8: Source detection part 2 (rev3428)

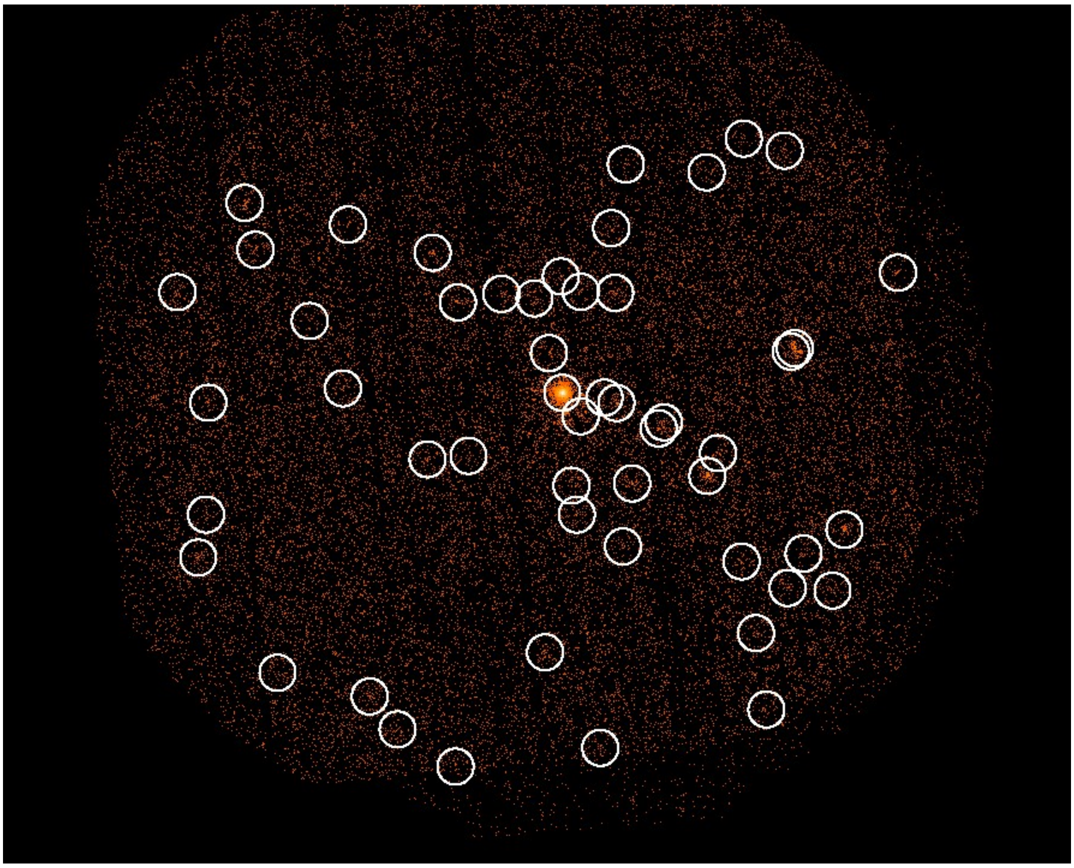

Figure 37: Source detection (rev3428).

5.2 Imaging

Now in possession of clean, filtered and calibrated data for the three observations, we can focus a bit more on the source of interest HD 149 404. The first thing we can extract is a proper normalized three-color image of the field of view. To place the source at the center of the final image we want to generate, we first need to know the coordinates of the binary system HD 149 404 which can be found on the Simbad portal in the International Celestial Reference System at epoch J2000 [47]. Those coordinates correspond to 16H 36min 22.56s in right ascension and -42° 51' 31.91" for the declination which respectively correspond to 249.09 and -42.86 in decimal degrees (unit used by SAS). The second requirement to generate such a three-color image is to divide the good events into three categories for each camera: soft, medium and hard. To do so, when creating an image like we did during the data reduction process, we will impose a criterion on the events based on the pulse invariant PI which directly relates to a criterion on the energy of the impacting X-ray photon. In terms of energy intervals, this corresponds, for the soft, to the range 500 to 999 eV, for the medium between 1000 and 1999 eV and finally, for the hard X-rays, between 2000 and 8000 eV. The code generating such image can be found on Listing 9 and corresponds to the EPIC MOS 1 camera soft band for revolution 3428. The increased binning is there to ensure that the image is smooth and avoid a pixel like image.

```
evselect table='3428_m1filt0_12xmmea.fits:EVENTS' xcolumn='X' ycolumn='Y' \
expression='(PI>499&&PI<1000)' \
raimagecenter=249.09417 decimagecenter=-42.85886 \
ximagebinsize=50 yimagebinsize=50 withfilteredset=true \
destruct=true withimageset=true imageset='imgm1soft.fits' \
imagebinning=binSize
```

Listing 9: Energy soft X-ray band MOS 1 (rev3428)

It is well known that the sensitivity of a detector is different for sources on and off axis. Those differences depend on the position of the source on the CCD but also the energy at which the source is considered (soft, medium or hard in our case). This means that, in order to compare the sources and to have an image that treats each source in the field of view similarly, one has to take into account this problem and correct it. This correction is performed by the creation of a so called exposure map which gives the effective exposure time for each pixel of the detectors at a given energy [45]. In SAS, the command eexpmap can be used to produce the exposure map at the condition the user supplies an image in a given energy band, the telemetry of the space telescope during the acquisition process as well as the filtered events list (the complete code is shown on Listing 10).

```
eexpmap imageset=imgm1soft.fits attitudeset=3428_0820510601_AttHk.ds \
eventset=3428_m1filt0_12xmmea.fits expimageset=expm1_soft.fits \
pimin=500 pimax=1000
```

Listing 10: Exposure map soft X-ray band MOS 1 (rev3428)

To produce the final three color image, one has to create, per observation (here we consider only rev3428), images and exposure maps for the 2 EPIC MOS and EPIC PN in each energy band we have defined previously. Considering here the case of the soft X-ray energy band of rev3428, to get the exposure map for the soft band "expo_soft", we need to add the exposure maps of the three instruments with the command "farith". The same is done with the three soft images to create an image representing the overall observation rev3428 in the soft band "softobs1". After a normalization of the soft band exposure map, we can finally correct the image by dividing it by the normalized exposure map. The outcome is an image, "colour1" corrected for the vignetting and other detectors artifacts that accurately represents the field of view of XMM-Newton in the soft x-ray energy band during revolution 3428 (cf. Listing 11 for the code related to the explanation).

```
farith exppn_soft.fits expm1_soft.fits inter.fits ADD
farith inter.fits expm2_soft.fits expo_soft.fits ADD

farith imgpnsoft.fits imgm1soft.fits inter.fits ADD
farith imgm2soft.fits inter.fits softobs1.fits ADD

fcarith expo_soft.fits 74080.8867 expo_soft_norm.fits DIV

farith softobs1.fits expo_soft_norm.fits colour1.fits DIV
```

Listing 11: Generation of normalized soft X-ray band image (rev3428)

So far, we have detailed the process of generating a corrected image for the soft x-ray energy band part of the observation which produces the first color of the three color image we are trying to create. To retrieve the other two colors, medium and hard energy band, the imaging process explained previously simply needs to be repeated but, this time, with the other energy bands defined as a criterion on the pulse invariant of the recorded events. This will generate an image for the medium energy band "colour2" and one for the high energy band "colour3". The Three color image is then simply obtained by plotting each "colour" images on the same figure with each a different color associated. It is common to use the red color for the soft part, the green for the medium and the blue for the hard. By making use of that color convention, the three color image, shown on Figure 38, is obtained.

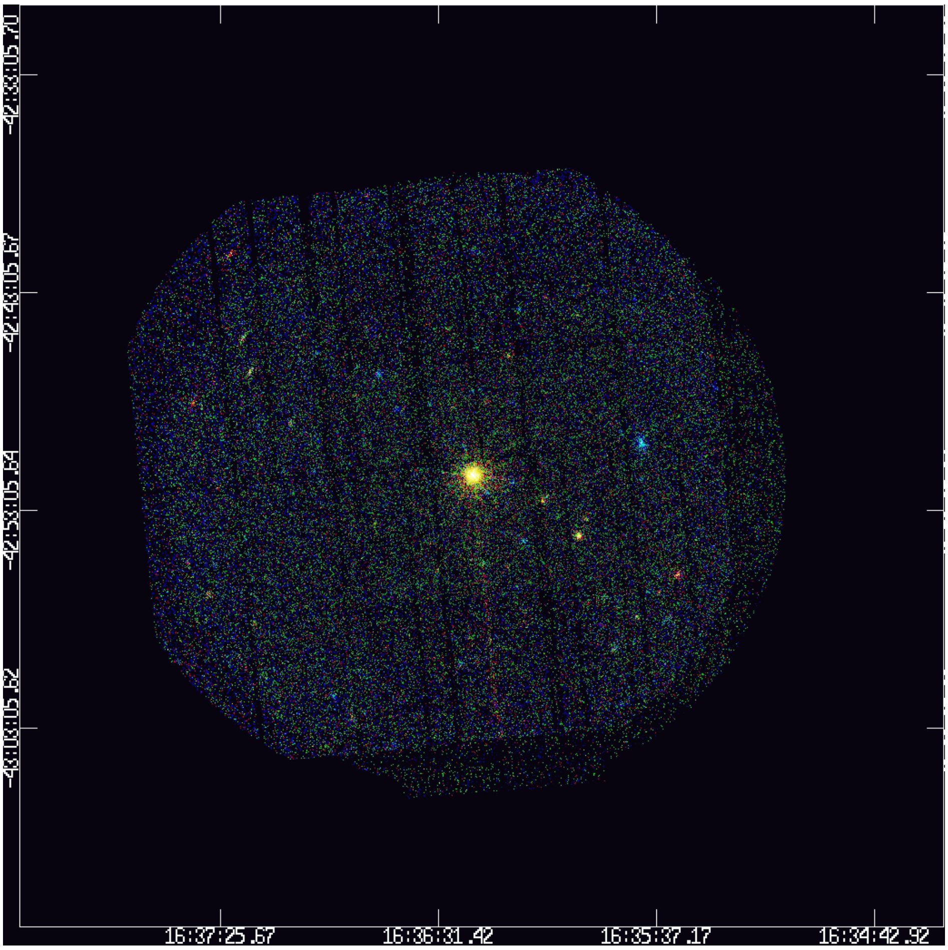

Figure 38: Three-color image.

On Figure 38, we can immediately spot the binary system of interest HD 149 404 placed at the center of the image which actually is the brightest X-ray source in the field of view. The other sources in the field of view seem to mostly be represented by only one of the three colors. Indeed, if we look to the right of HD 149 404, we can observe a small blue dot corresponding to a source almost entirely emitting hard X-rays. This could mean that the source is extremely hot and produced mostly hard X-rays and maybe even γ-rays or that the source is so far away from us that the interstellar medium has absorbed most of the soft and medium X-ray photons before they even had the chance to reach us which is, for instance, the case for sources located in the plane of our galaxy. On the other hand, if we look at the bottom right of the figure, we can see a red source meaning that the source is probably not hot enough and barely produces any X-rays. A final remark that can be done on this image concerns the presence of out of time events. If we look at the vertical below the binary system HD 149 404, we can clearly see a line that stops once our binary system is reached. This is the defining characteristic of out of time events which correspond to the impact of X-ray photons on the detector during the read-out time. Since those photons have impacted the detector during the read-out sequence, they have then been attributed to the wrong location on the CCD while they actually came from HD 149 404. This loss of photons is however very common for bright sources since no shutters are placed in front of the detectors during the read-out sequence but, fortunately for us, those events do not alter the quality of the data and can be ignored.

5.3 Spectrum Extraction

In this data processing section, we have started by reducing the data of the entire field of view and turning them into scientifically usable events. We have identified multiple sources in the XMM-Newton field of view and produced a three color coded image of this field of view with our source at the center. With the reduction and imaging steps of the data processing, we have made it possible to focus on the specific X-ray source that is HD 149 404 and to extract the source spectrum with the Science Analysis System in order to fit the three observations with a spectral model and learn valuable information by analyzing it.

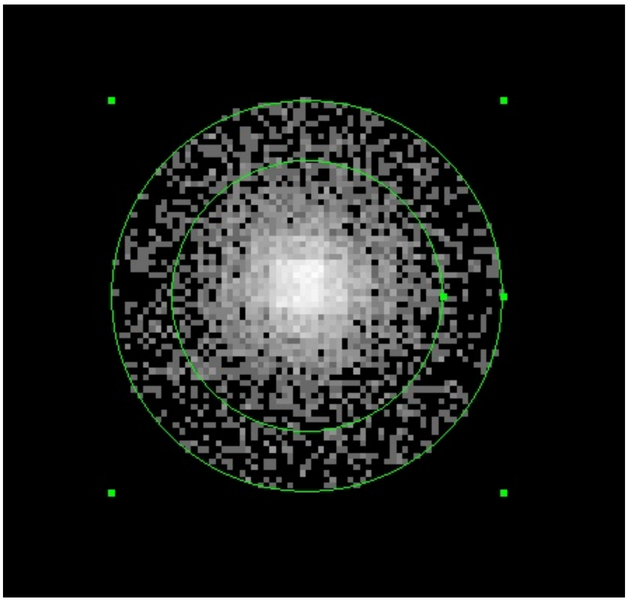

Figure 39: Source and background regions of HD 149 404.

To start the spectrum extraction process, we will, once again, start by creating an image of the region of interest HD 149 404 with the command evselect. This image is created from the filtered and calibrated events list and one spectrum will be extracted per instrument and per revolution. To create this image, we need to specify a source region as well as a background region. The source region is quite obvious and simply corresponds to the source we want to study which is identified by a set of coordinates, here physical ones in X and Y respectively 26866.611 and 27728.587, representing the source center and a radius, 450, of a circle that accounts for the extend of the source (no sources are exactly point like). The background region is a bit more complex and accounts, in principle, for all events unrelated to the source. This background can be internal, due, for instance, to Copper or Aluminum lines coming from the detector itself being excited by the incoming cosmic rays, or external such as diffuse X-ray emissions and cosmic X-rays. The true background, behind the source of interest, is however unknown and requires to be approximated. This approximation, of both internal and external background, coincides with all the events occurring in an annulus around the source of interest. Since our source is far away from any other sources and not at the edge of a CCD, we can build a full annulus around the source. The idea being that the background region is solely due to the background while the source region is a combination between the source and background events occurring in front or behind the stars of interest. To remove these effects, the basic principle is to subtract that background from the contaminated source to generate a spectrum solely accounting for the X-ray emission coming from the binary system. The generation of those images is shown on Listing 12 while a graphical representation of those two regions is available on Figure 39. It it worth mentioning that, for revolution 3426 contaminated by a high background (solar activity in this background context), the Good Time Intervals event list needs to be used to generate the source and background region image, hence a different code on Listing 12.

```
Valid for rev 3422 and 3428:

 evselect table="3428_pnfilt0_4flag0.fits:EVENTS"  imagebinning="binSize"
 imageset="brol.fits" \
 withimageset=yes xcolumn="X" ycolumn="Y" ximagebinsize=20 yimagebinsize=20 \
 expression="((X,Y) IN circle(26866.611,27728.587,450))
                 ||((X,Y) IN annulus(26866.611,27728.587,450,650))"

Valid for rev 3426:

 evselect table="3426_pnfilt0_4flag0gti.fits:EVENTS"  imagebinning="binSize"
 imageset="brol.fits" \
 withimageset=yes xcolumn="X" ycolumn="Y" ximagebinsize=20 yimagebinsize=20 \
 expression="((X,Y) IN circle(27125.656,27544.837,450))
                 ||((X,Y) IN annulus(27125.656,27544.837,450,650))"
```

Listing 12: Identification of source and background regions for EPIC PN

Now in possession of source and background regions, we can proceed to the extraction of the X-ray spectrum with the command especget as shown on Listing 13. This task will produce all the files necessary for the next part of the thesis and the spectral fitting of an XMM-Newton target. It will generate a source and background spectrum as well as the redistribution matrix file (RMF) and ancillary response file (ARF). The RMF contains information about the number of free electrons generated by the arrival of a photon of energy E. In a perfect world, a photon of energy E should always generate a fixed number of free electrons but this is unfortunately not the case and, most of the time, the number of free electrons generated varies over time and depends on the pixel impacted even though the impacting photon has the exact same energy E. For those reasons, a RMF must be created for each instrument and each observation as HD149404 was not exactly at the same position on the detector in the three observations we have at our disposal. A clear evidence is available on Listing 12, if we look at the position of the target in revolution 3428 and 3426, we can clearly see that the target is located at two distinct positions on the CCDs (center of the source region). As far as the ARF is concerned, this file contains information about the telescope effective area as well as filter absorption as a function of the energy within the source region defined. The combination of those two files corresponds to the instrumental response of the X-ray instrument used to observe the target.

```
 especget filestem="3428_HD149404_pnspec"
srcexp="((X,Y) IN circle(26866.611,27728.587,450) )"
backexp="((X,Y) IN annulus(26866.611,27728.587,450,650))"
table="3428_pnfilt0_4flag0.fits"

 specgroup spectrumset="3428_HD149404_pnspec_src.ds" minSN=3 oversample=5
rmfset="3428_HD149404_pnspec_src.rmf"
arfset="3428_HD149404_pnspec_src.arf"
backgndset="3428_HD149404_pnspec_bgd.ds"
groupedset="3428_HD149404_pnspec.pi"
```

Listing 13: Generation of spectrum and energy calibration files (rev3428 EPIC PN)

On Listing 13, we can also see another command specgroup whose role is to regroup all the relevant files for spectral modeling and fitting, done with the Xspec software in a following section, and link them to a repertory file that will be transmitted to Xspec. This file is similar to the ODF Summary File we discussed previously in the sense that it is used by the software to retrieve all the necessary information without having to indicate all the paths and names every time a new model is tried. On Figure 40, we can see what that spectrum looks like for revolution 3422 and the interesting parts of the graph at this point, for us, are the crosses representing the observational data we just extracted (the line being a spectral model we will discuss later on). The green color stands for the spectrum recorded by the EPIC PN instrument while the black and red crosses respectively correspond to the EPIC MOS 1 and 2 instruments.

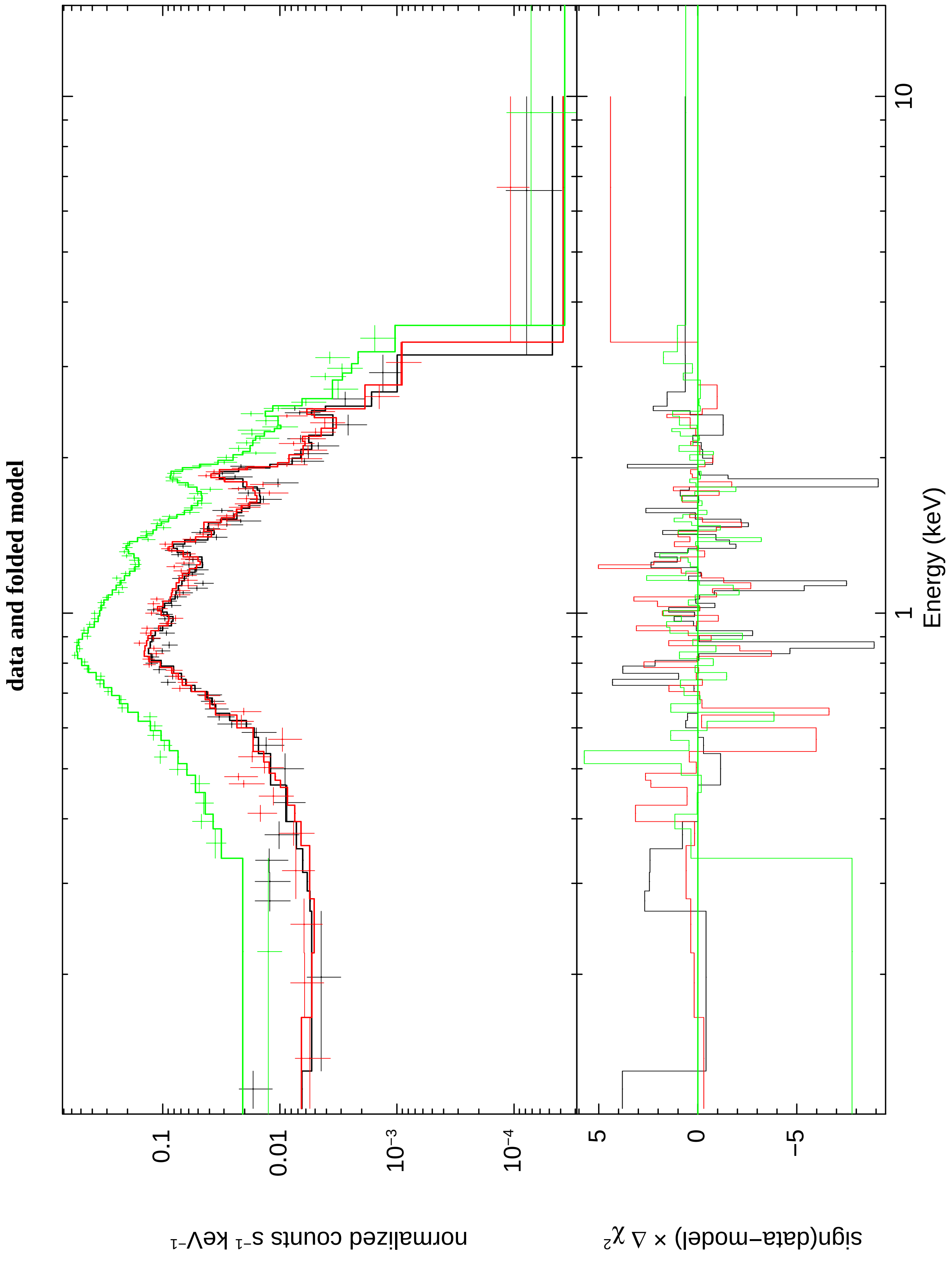

Figure 40: Spectrum of revolution 3422.

6 Spectral Modeling

After reducing the data acquired during the three observations performed by XMM-Newton, we were able to identify the source of interest, the binary system HD 149 404, among the several sources located in the field of view during the observations. This identification allowed us to retrieve the spectrum of the target, by selecting a source and a background regions, as well as to create all the energy calibration files required to model and fit such spectra by the software Xspec.

As stated in the introduction of the user manual, XSPEC is: "a command-driven, interactive, X-ray spectral-fitting program, designed to be completely detector-independent so that it can be used for any spectrometer" [35]. This means that this software can be used to analyze data coming from the Einstein observatory, ROSAT, ASCA and XMM-Newton. This is one of the most commonly used software in high energy astrophysics and, to this day, 9.300 scientific papers have been published on the Astrophysics Data System (ADS) directly mentioning its use. The first version was developed in 1983 and has been continuously updated since to reach the current version Xspec 12 developed by Keith Arnaud, Ben Dorman, and Craig Gordon under the supervision and support of the High Energy Astrophysics Science Archive Research Center (HEASARC) [39], member of the National Aeronautics and Space Administration (NASA).

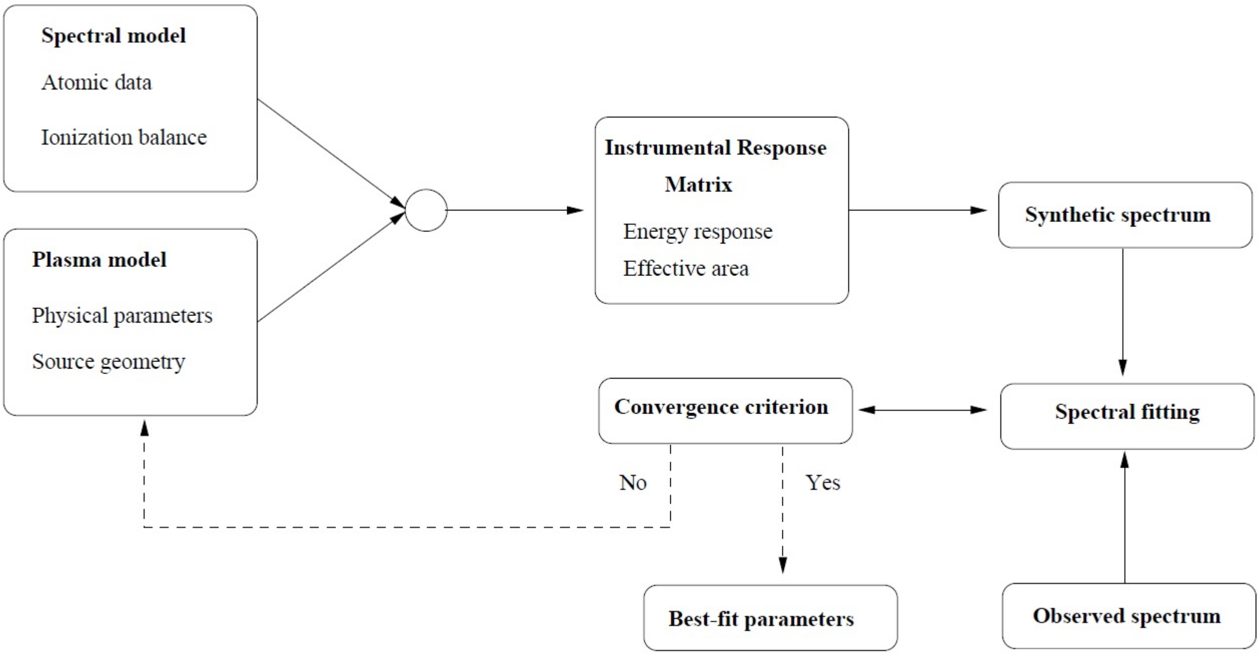

Figure 41: X-ray spectral modeling scheme [45].

Before entering into the spectral modeling part, it is interesting to quickly recall the process and main characteristics of X-ray spectral fitting summarized on Figure 41. We know, at this stage, that the observed X-ray spectrum we have is actually a convolution of the real spectrum with the instrumental response that we divided into a redistribution matrix file for the energy response and an ancillary response file for the effective area effect. Due to their complexity (cf. Figure 33 for the EPIC MOS effective area), the inversion of this problem does not possess a unique solution. Therefore, a fitting theoretical model, based on assumptions on the actual target properties and a set of free parameters, is built and combined with the instrumental response (RMF and ARF) at which point it can be compared with the observed spectrum. This process requires multiple iterations on the model free parameters to reach a satisfactory synthetic spectrum. The reason to improve a model comes from the fact that all the source characteristics and properties will be deduced from this theoretical spectrum which is why, in this section, we will develop and improve our spectral model of HD 149 404 starting from a simple model up to the most advanced one in order to be sure that the properties, like the X-ray flux we will extract at the end, are as close as possible to the actual flux created by the binary system.

As far as the binary system HD 149 404 is concerned, we will use a plasma model in Xspec belonging to the family of optically thin thermal plasma models. In such plasma, once an X-ray photon is emitted, it does not interact anymore with the plasma which means that the emitting plasma is sufficiently transparent for an emitted photon to leave the plasma without further interaction. In this way, the resulting spectrum reflects solely the microscopic processes occurring in that plasma [45]. This plasma is at a certain temperature and follows an equilibrium in terms of ionization. One model is defined by a temperature and a composition ruled by the ionization equilibrium equation (56) for each element still retaining electrons. This equation represents a balance between the ionization by electron impact ($S_{Z,z}$) and the recombination by electron capture ($\alpha_{Z,z}$) of an element of atomic number Z (hence Z+1 equations). In this equilibrium, N_e stands for the number density of electrons, $N_{Z,z}$ the number density of ion Z^{z+}, Z the atomic number of the element and z the ionization state.

$$\frac{1}{N_e}\ \frac{dN_{Z,z}}{dt}\ =\ N_{Z,z-1}\ S_{Z,z-1} -\ N_Z\ (S_{Z,z}+\alpha_{Z,z}) +\ N_{Z,z+1}\ \alpha_{Z,z+1} \tag{56}$$

If the temperature of the plasma is maintained at a constant value (radiated power is compensated by heat generation), the ionization equilibrium is stationary and the ionization balance is given by equation 57. This is a good assumption as long as the microscopic processes are fast compared to the plasma as a whole (not valid during a Supernovae explosion for instance). With this hypothesis, the ionization rate $S_{Z,z}$ and the recombination rate $\alpha_{Z,z}$ depend mostly on the electron temperature T_e within that plasma (kinetic energy of the free electrons).

$$\frac{N_{Z,z+1}}{N_{Z,z}}\ =\ \frac{S_{Z,z}(T)}{\alpha_{Z,z+1}(T)} \tag{57}$$

For every iteration on the spectral model presented in this section, the solar abundances in the plasma emission and photoelectric absorption models will be set to the values determined by Asplund M., Grevesse N., Sauval A.J. & Scott P. (2009, ARAA, 47, 481) [15]. Similarly, the absorption by the interstellar medium will be described using the latest version of the Tuebingen-Boulder ISM absorption model (TBabs in Xspec) with an hydrogen column density of 0.372 $10^{22} cm^{-2}$ as determined by S. B. Gudennavar [17] (cf. Section 2.1).

6.1 Simple spectral model

The first spectral model we are going to try is an extremely basic one. It consists of two main components: an absorption part and a plasma emission model. We have already stated that the absorption by the interstellar medium between us and the source HD 149 404 will be taken care of by the TBabs Xpsec model based on the hydrogen column density determined by S. B. Gudennavar [17] but this is not the only absorption that can occur in our system. Indeed, the cool wind material contained in the binary system itself can also absorb the X-rays produced close to the hydrodynamic shock and trying to "escape" the system. This photoelectric absorption, mostly by the stellar winds, is however unknown and requires to be evaluated by a free parameter expressing the equivalent hydrogen column density of this portion of the absorption. To model this is Xpsec, we will add the phabs model with only one free parameter n_H.

The second part of this first model is there to represent the plasma and, in particular, the optically thin thermal plasma that fits best the physical processes taking place during the collision of stellar winds and the creation of a hydrodynamic shock. In Xspec, this corresponds to a model of the family APEC (Astrophysical Plasma Emission Code) emission spectrum which, based on atomic data coming from the AtomDB [18] (Atomic data for astrophysicists), is able to produce an emission spectrum resulting from the collisionally-ionized equilibrium in the plasma at a given temperature that needs to be determined (the temperature being a free parameter). From this apec model and once the best-fit solution is found, we can get important information about the source responsible for the emission such as the plasma temperature in keV and the norm in cm^{-5} of this plasma emissions (the emission measure of the APEC model) computed by equation 58 where D_A stands for the angular diameter distance to the source (cm), z is the redshift and n_e and n_H respectively represent the electron and hydrogen densities (cm^{-3}).

$$\frac{10^{-14}}{4\pi\left[D_A\ (1+z)\right]^2}\int n_e n_H\ dV \tag{58}$$

```
model  tbabs*phabs*(apec+apec)
```

Listing 14: First spectral model

While dealing with the X-ray spectra of O-type stars, a single plasma at one temperature is usually not enough to fully describe the emission spectrum of the source. To account for this possibility from the beginning, we will have our first model made of two distinct plasmas and our first spectral model ends up taking the form shown on Listing 14. The fact that multiple plasma components are responsible for the emission can also be quite obvious in our case due to the presence of stellar winds as well as a hydrodynamic shock and post-shock plasma. Indeed, while discussing the mechanisms and characteristics of stellar winds collision (cf. Section 2.3), we have seen that the plasma constituting the stellar winds will have a drastic increase of temperature due to the hydrodynamic shock. It is then reasonable to imagine that the cooler plasma (stellar wind not affected by the wind-wind interaction) will contribute more to the softer part of the spectrum while the hot post-shock plasma will contribute more in the higher energy part of the emission. One could argue that the two stellar winds are at a different temperature and should then be accounted for separately which would take the form of three distinct apec models. This is a valid argument that will be discussed later on and, in the meanwhile, we will keep it basic with only two plasma models at two different temperatures.

Fitting such a model (cf. Listing 14) to the three observations, we obtain the results given in Table 3. In this table, we have the plasma temperatures, the hydrogen column density of photoelectric absorption, an estimation of the flux for the EPIC MOS 1 detector in the soft X-ray energy band between 0.5 and 1.0 keV as well as the χ squared associated with the model of each observation. Even though fluxes for the other detectors and at different energy bands have been computed alongside the emission norm of the emitting plasma, they are not shown here since we are dealing with a simple first model of the binary system and those results still require multiple iterations of the model to reach an acceptable state that can be used to derive properties of HD 149 404. However, we can still make a few remarks on this first attempt at spectral modeling. The first important information, that is relevant any time we try to model observations, is the notorious statistic χ^2 which is a measure of the difference between our synthetic spectral model and the spectrum resulting from the data processing of XMM-Newton. The fact that, for all three observations, this statistic is close to one indicates that the best fit solutions we found are a good match for the observations which is the first criterion to even discuss the results one obtains by a mathematical model of real data. Another visual proof of the accuracy of our model can be seen on Figure 40 shown at the end of the data processing section (cf. Section 5). We can now focus on the bottom graph of the Figure representing the χ squared for each detector as a function of energy, and the plain line fitting the data represented by the crosses. Discarding the fit at both extremities due to a lack of a sufficient amount of data, we can see that the plain line correctly follows the data.

This is especially visible on the PN spectrum (green curve) since it is well separated from the other two MOS instruments. Since our model fits accurately the observed spectrum, we can look at the properties estimated by the model for the three observations. One notices immediately that there are clear variations in terms of temperatures, hydrogen column density and flux between the three observations with rev3426 standing out and having the biggest drift between the three data sets. We can also notice that the two temperatures are quite separated, first one around 0.17 keV while the second one is closer to 0.61 keV, which indicates that the choice of multiple plasmas was the right approach to model the observations. Indeed, if one temperature would suffice, the two plasma temperatures would most likely converge to the same value since they are free parameters of the fit.

	Rev 3422	Rev 3426	Rev 3428
n_H $[10^{22} cm^{-2}]$	0.46	0.38	0.46
kT_1 [keV]	0.18	0.15	0.18
kT_2 [keV]	0.61	0.62	0.61
Soft X-ray (0.5 to 1 keV) flux MOS 1 $[10^{-4}$photons cm^{-2} $s^{-1}]$	2.27	1.80	2.52
Reduced χ^2 [/]	1.19	1.26	1.16
dof [/]	220	208	231

Table 3: First spectral model (results).

6.2 Number of plasma components

We have built our first spectral model based on simple assumptions regarding the number of plasma components required to best fit the observed spectrum. Based on a scientific reasoning, we concluded that two plasma models at two different temperatures would be a good choice to start with. We will now put that hypothesis to the test thanks to a statistical method, an F-test, who will compare two models between them and assess the relevance of the upgrade. In our test, even though we ruled that out quickly in the first spectral model, we will start by having one plasma and gradually increase the number of plasmas to evaluate if the addition of a temperature is useful. In Xspec, this is done by the command ftest who, solely based on the χ^2 and degrees of freedom of two distinct models, will return an F-statistic value and its probability. In the context of an F-test in Xspec, if the probability is low, it means that the addition made to the model is reasonable and the added component should be kept [35] from a purely statistical point of view which will have its importance in the process of choosing the right number of plasma components.

```
ftest chisq2 dof2 chisq1 dof1
```

Listing 15: F-test syntax

By adding or removing a plasma model, apec, in the Xspec command (cf. Listing 14), we can fit the observed spectrum with theoretical models made of one plasma and up to four. The resulting χ^2 and associated degrees of freedom of those four different models can be found in Table 4. We have already stated that the F-test only cares about statistics and not the relevance of the physical parameters in those models meaning that, even if a plasma temperature is found to be either incredibly low or extremely high, the F-test could still lead to the conclusion that the improved model is better which is why someone needs to make the decision at the end. The F-test shown here only concerns the models of observation rev 3426 but the test was performed on the three observations which behave similarly in terms of the F-test results.

Number of plasma models	1	2	3	4
χ^2 [/]	426.46	261.65	244.46	239.76
dof [/]	210	208	206	204

Table 4: χ^2 and degrees of freedom as a function of the number of plasma components in the spectral model (rev3426).

Once in possession of the required model statistics (χ^2 and degrees of freedom), we can apply the ftest command to two successive models which consists of comparing a model with X temperatures to a model with X+1 temperatures. After every model has been compared, we obtain the following results (cf. Table 5):

	From 1 to 2 temperatures	From 2 to 3 temperatures	From 3 to 4 temperatures
F-statistic F [/]	65.51	7.24	2.0
Probability p [/]	$8.62\ 10^{-23}$	0.00091	0.14

Table 5: F-test values and probabilities (rev3426).

The F-test probability comparing one and two temperature clearly stands out due to its extremely low value. This means that the first assumption we made on our source and the use of two plasma models to described it was a valid one in the first spectral model. The χ^2, going from one to two temperatures on Table 4 also significantly improves and this upgrade can not be ignored by having only one plasma in our model. If we look at the other extremity of the F-test going from a model with three temperatures to one with four, while the F-test is able to run, the parameters of a four temperatures model are not well constrained such as the fourth temperature that is close to zero keV and the solution found by Xspec was also accompanied by different warnings regarding the parameter space which lead us to conclude that a model with four temperature was not appropriate for our specific observations. The fact that the F-test probability is also 0.14 implies that the addition of this fourth temperature is not necessary nor reasonable. The last F-test is actually the most problematic since all the parameters seem to converge on Xspec to valid physical ones and the F-test probability is neither low nor high but in the middle. This signifies that a model with three temperatures, while not being as big of an improvement as going from one to two temperatures, can be a valid model that slightly improves the two temperatures model.

This F-test allowed us to reject models with one temperature but also models with more than three plasma components (three temperatures) but could not help us decide between two or three temperatures models. Based on the fact that we will already complexify the spectral model disregarding the number of plasma components, choosing a spectral model with three temperatures (hence three distinct emitting plasmas) would render the computation and solution finding even more complex by adding more free parameters which possibly leads to many more local minima in our parameter space. A two temperature model will then be used to describe the source HD 149 404 due to the complications that a three temperatures model would bring and to the F-test not clearly demonstrating a significant benefit to add this third temperature to our model.

6.3 Spectral model with free abundances

When we discussed the characteristics of massive stars (cf. Section 2.2), we have briefly discussed the convective phenomena that can bring material processed by the CNO cycle and other fusion reactions from the stellar interior to the surface and upper atmosphere of the star and, eventually, being ejected by the massive star via the stellar wind. This characteristic of massive stars led us to change the model by letting the abundances of those specific elements (Carbon, Oxygen and Nitrogen) free to vary and not set by default to the solar abundances as it is the case for the apec model. The value of those parameters in the apec model were, by default, set to the solar abundances values coming from the model developed by Asplund M. and his colleagues. To set those parameters free, the plasma model is changed from the apec one to the vapec which is still an optically thin thermal plasma model similar to apec with more options regarding the abundances [35]. The full list of elements whose abundances can be set free is the following: He, C, N, O, Ne, Mg, Al, Si, S, Ar, Ca, Fe, Ni. However, in our case, we are only interested in the Carbon, Oxygen and Nitrogen which implies that the remaining elements will still be defined by the solar abundances from the Asplund model. This new model takes a similar shape as the first spectral model developed and is shown on Listing 16.

```
model tbabs*phabs*(vapec+vapec)
```

Listing 16: C N O abundances free spectral model

Once we supplied the data to this new synthetic spectral model, we can start the iterative process of fitting the model parameters in the hope of finding their best values which is what we did for the first spectral model. However, here, we are also interested in the confidence intervals of the best fit solution in order to find some constraints on the model parameters and possibly identify a trend in those model parameters. This search of confidence regions for a model parameter is done in Xspec by the command error followed by the number assigned to the model parameter we want to assess the confidence interval. The process was done for multiple parameters and the outcome can be found on Table 6 for the three observations. Note that the Carbon, Nitrogen and Oxygen abundances have no unit since they are expressed relatively to the solar abundances of the Asplund model [15].

	Rev 3422		Rev 3426		Rev 3428	
Confidence interval	min	Max	min	Max	min	Max
kT_1 [keV]	0.285	0.35	0.28	0.37	0.28	0.36
kT_2 [keV]	0.70	0.765	0.63	0.745	0.695	0.76
Carbon [/]	0	20	0	13.43	0	13.16
Nitrogen [/]	7.27	25.83	25.89	52.91	15.80	35.48
Oxygen [/]	1.00	1.89	0.92	1.84	1.29	2.37
Reduced χ^2 [/]	1.15		1.14		1.07	
n_H [$10^{22} cm^{-2}$]	0.42		0.32		0.40	

Table 6: Carbon, Nitrogen and Oxygen free abundances spectral model.

The first important quantity that is worth looking at is, once again, the reduced χ^2 to access the accuracy of our model and we gladly found that the reduced χ^2 of this model with free abundances are smaller than the ones from our previous model (cf. Table 3). This is important since it assesses the improvements made by changing the model from apec to vapec and freeing the Carbon, Nitrogen and Oxygen abundances. When looking at the confidence intervals for the freed elemental abundances, we immediately notice the strange behavior of the Carbon whose abundance is even compatible with 0. Such behavior indicates that the fit is actually insensitive to the presence of Carbon. The Nitrogen, even though also accompanied by a large interval, clearly follows a tendency of overabundance in comparison to the solar abundances which was badly represented in our first model. Finally the Oxygen is well constrained and, for every observation, seems close to the solar abundance which could mean that the Oxygen relative abundance is compatible with one.

If we take a look at the temperatures, we can see that their confidence intervals, for both kT_1 and kT_2, are pretty similar for the three observations which means that we could impose a constraint on their values that could be identical for the three spectral models as long as the values are compatible with each confidence interval. We also noticed that the first temperature kT_1 has almost doubled in comparison with the first temperature of the previous model (cf. Table 3). This can be understood by the increase abundance of Nitrogen in this new model. In fact, spectral lines due to Nitrogen in the X-ray domain are located at a low energy, mostly below 1 keV [45]. To correctly represent the flux in the soft part of the spectrum we can either assume a model with solar abundance but lower plasma temperature or a model with an enhanced Nitrogen abundance, but a slightly higher temperature. We could see the first model as a trick of Xspec who was able to correctly account for the low energy part of the spectrum by compensating the wrong and lower Nitrogen abundance by a plasma centered at the peak emission temperature.

Now that we have a better and more accurate model for the spectrum of HD 149 404, we could be tempted to add another plasma with a third temperature since the choice of keeping only two plasma models was mainly subjective. By doing so, the third temperature accounts for the lower part of the spectrum at around 0.1 keV while the other two remain within the confidence interval of the two temperatures model. However, even though the χ^2 improves with the addition of a third temperature, the F-test probability is now 0.12 if we consider revolution 3422 (similar result for the other two observations). Unlike our very first model where the F-test could not help us decide, we are here with a high probability that statistically indicates that the addition of this third plasma is not reasonable. This concludes the still open question about the number of temperatures and plasma models that need to be included in our Xspec spectral model and sets the best number to be two vapec models at two distinct temperatures for the emitting plasmas.

6.4 Spectral model with fixed abundances

Now that we have managed to establish some general properties of the plasma whose X-ray spectrum we are trying to fit with our Xspec model, we could try to constrain those model parameters by a priori knowledge of the binary system HD 149 404. To find this knowledge, we first have to remember that the X-ray emission we are observing with XMM-Newton is mostly coming from the hydrodynamic shock generated by the encounter of the highly supersonic stellar winds of two massive stars. The actual plasma emitting the X-ray photons is then comprised of elements coming from both winds and could therefore possibly be modeled by a mix of the compositions of the winds of both stars. To get those abundances, we have to go back to Section 2.1 where, in the paper "Observational signatures of past mass-exchange episodes in massive binaries: The case of HD 149 404" by Raucq & al. [9], members of the department of Astrophysics, Geophysics and Oceanography at the Liège university performed the disentangling of the optical spectra of the two stars. They were able to reconstruct the spectra of both stars separately as if they were not part of a binary system and determine the composition of the stellar atmosphere of both stars which will end up representing the stellar wind composition due to the wind driving mechanism.

	50/50 mixture	secondary only
Carbon [/]	0.22	0.07
Nitrogen [/]	6.26	10.58
Oxygen [/]	0.83	0.16

Table 7: Carbon, Nitrogen and Oxygen fixed abundances.

Two different models will be put to the test. In a first one, we will assume a perfect mixture of the stellar winds of both stars resulting in an emitting plasma made of fifty percent of the abundances in the stellar wind of the primary and the remaining fifty percent coming from the abundances in the secondary stellar wind. As the wind of the primary star is stronger than the secondary one, it is reasonable to estimate that the shock is actually stronger for the stellar wind of the secondary star. In return the material of the stellar wind of the secondary star will be the one heated and emitting most of the X-rays which is the reason we will also try a model where the abundances are set by the secondary wind only. All the relative abundances in Carbon, Nitrogen and Oxygen used in the following spectral models can be found in Table 7.

6.4.1 Wind of only the secondary star (0/100 composition)

For this new model, within which we only consider the Carbon, Nitrogen and Oxygen abundances coming from the secondary star wind, we still use the model represented on Listing 16 at the exception that, this time, the C,N,O abundances will be frozen to the secondary values. The parameters of the best fit solution for the spectral modeling of the three observations can be found on Table 8.

	Rev 3422	Rev 3426	Rev 3428
n_H $[10^{22} cm^{-2}]$	0.473	0.395	0.461
kT_1 [keV]	0.215	0.252	0.203
kT_2 [keV]	0.605	0.901	0.608
Reduced χ^2 [/]	1.4916	1.8339	1.4957

Table 8: Secondary abundances, spectral model.

During the computation and iterative process performed by Xspec, multiple alerts appeared to indicate that the model parameter may be ill conditioned which is already a sign that this might not be the best solution in terms of fixing the abundances. Once the results were computed and the model parameters extracted, we can see that the reduced χ^2 is higher than the ones with the free abundances model with an increase of up to 62 percent in the worst case (rev 3426). We can then conclude that a plasma with C, N, O abundances coming solely from the wind of the secondary star is not suited to describe our binary system. This could be due to the low relative Oxygen abundance linked to such an assumption of 0.22. Indeed, with the free abundances model, we saw that the Carbon was not constrained at all, the Nitrogen was obviously overabundant with respect to the solar values and the Oxygen was compatible with a solar abundance. Here, the tendencies are respected as far as the Carbon and Nitrogen are concerned but not at all for the Oxygen which makes it extremely difficult to fit the plasma with our synthetic spectrum.

6.4.2 Perfect mix of the stellar winds (50/50 composition)

The other possibility evoked is to represent the Carbon, Nitrogen and Oxygen abundances as a perfect mix between the two stellar winds involved in the binary system (cf. Table 7). In such hypothesis, each wind contributes evenly to the composition of the emitting plasma and the model parameters of the best fit solution computed by Xspec are available in Table 9.

With this model and the 50/50 assumption on the stellar winds mixture, no errors nor alerts were emitted by the spectral modeling software which is already a sign that the assumption made here is better than the previous one. This is confirmed by the reduced χ^2 closer to the free abundances model (cf. Table 6). The slight increase in its value comes directly from the imposed Nitrogen and Oxygen abundances since the Carbon one was not constrained at all. In our model, the Nitrogen and Oxygen, while being close to the free abundance model and following the discovered trends (overabundant Nitrogen and Oxygen compatible with solar abundance) are slightly below the free abundance values which degrades a bit the fit as expected.

	Rev 3422	Rev 3426	Rev 3428
n_H [$10^{22} cm^{-2}$]	0.487	0.391	0.484
kT_1 [keV]	0.2066	0.175	0.197
kT_2 [keV]	0.6133	0.618	0.619
Reduced χ^2 [/]	1.1834	1.1655	1.1284

Table 9: 50/50 mixture for the abundances, spectral model.

Similarly to the free abundances model, all the second temperatures are almost identical while the first ones seem a bit apart. However, if we consider their confidence intervals, the same can be said regarding the first temperature. We can also notice the decrease in the two temperatures if we compared them to the free abundances model temperatures. This can be explain by the difference between the Carbon, Nitrogen and Oxygen abundances of this fixed model and the free model ones. Analogously to the explanation of the increase in temperatures while going from the first spectral model to the free abundances one due to an increase in the Carbon, Nitrogen and Oxygen abundances in section 6.3, the opposite phenomenon is actually taking place here. When we set the fixed abundances at lower values than the free ones, the lowest temperature kT_1 was shifted down to compensate the loss of photons in the lower energy part of the spectrum due to this decrease in abundances. In practice, the code shifted the temperature toward the maximum, the peak emissivity of the Carbon, Nitrogen and Oxygen which is located at a lower temperature. Since the first temperature decreased, the equivalent column density of hydrogen of the photoelectric absorption by the binary system itself (the stellar wind) slightly increased which had a repercussion on the second temperature kT_2 that was also decreased to correctly reproduce the observed flux at higher energies.

6.5 Final spectral model

So far, we started with a very basic and simple model that we progressively improved in order to find constraints on the model parameters. By a scientific reasoning and the use of results from previous studies on the binary system of interest HD 149 404 (cf. Section 2.1), we were able to constrain the Carbon, Nitrogen and Oxygen abundances in the emitting plasma. Similarly, we concluded that two optically thin plasma models were an accurate representation based on a statistical approach, the F-test. In all our previous models, we also noticed that the two plasma temperatures were always close to each other in-between the three observations we have at our disposal. Moreover, by looking at their respective confidence intervals, a common value could be compatible for the three data sets which led us to conclude, for our final model, that the two temperatures will be constrained and the attributed values are the mean kT_1 and kT_2 of the model we called "Perfect mix of the stellar winds (50/50 composition)". Let's also recall that the absorption by the interstellar model is still set by the hydrogen column density from Gudennavar & al. [17]. All those well constrained parameters are summarized in Table 10.

TBabs n_H (ISM) [$10^{22} cm^{-2}$]	kT_1 [keV]	kT_2 [keV]	Carbon [/]	Nitrogen [/]	Oxygen [/]
0.372	0.193	0.617	0.22	6.26	0.83

Table 10: Model parameters fixed in the final model.

In Xspec, by fixing those model parameters in the vapec plasma models (cf. Listing 16) and running the spectral fitting code, we ended up with results, for the remaining free parameters, gathered on Table 11 (Best fit values as well as their confidence intervals). Imposing those parameters does actually not noticeably degrade the χ^2 which confirms that we have made the right choices for those parameters. The photoelectric absorption by the stellar wind, represented by an equivalent hydrogen column, was not fixed since it is a property of the binary system we want to study and that, as we can easily understand, will vary depending on how we see the hydrodynamic shock (phase of the binary system) and especially through which stellar wind. The same can be said about the emission norms whose variations correspond to a different flux reaching us due to the phase of the system during the acquisition process. The variations associated with each revolution, accurately represented with our final, most advanced best fit model, will be the basis of the analysis of the binary system HD 149 404 performed in a following section. Indeed, now that we have our best model, we can extract important properties on the binary system such as fluxes in different energy bands, the global X-ray flux to compute the L_x/L_{bol} ratio and a bunch of other relevant quantities.

	Rev 3422			Rev 3426			Rev 3428		
Confidence interval	best fit	min	Max	best fit	min	Max	best fit	min	Max
Photoelectric absorption n_H $[10^{22} cm^{-2}]$	0.468	0.434	0.507	0.415	0.381	0.450	0.480	0.445	0.518
Plasma 1, emission norm $10^{-3}[cm^{-5}]$	4.323	3.228	5.778	2.931	2.244	3.802	5.647	4.307	7.381
Plasma 2, emission norm 10^{-3} $[cm^{-5}]$	1.386	1.341	1.432	0.922	0.888	0.956	1.472	1.425	1.520
Reduced χ^2 [/]	1.184			1.180			1.066		

Table 11: Final model best fit solution with confidence intervals.

7 Analysis & Wind Collision Modeling

Now in possession of our best fit model for the three observations at our disposal, we can start to analyze the data and check if the overall picture is consistent with what is expected for colliding wind binaries. We will here keep the syntax established in Section 5 to refer to the observations. However, it is useful, in order to analyze properly the data, to recall that the observations rev3422, rev3426 and rev3428 correspond respectively to observations of the binary system HD 149 404 at phases close to 0.25, 0.0 and 0.5 (cf. Section 4). See Figure 5 for a schematic view of the system as well as the projected line of sight at those orbital phases.

7.1 X-ray Spectra

A first analysis can be based on the fitted spectra of the three observations. On Figure 42, the three EPIC-PN spectra are gathered. This comparison clearly indicates variations and, especially, at low energy between 0.7 and 1 keV. We can clearly see that the conjunction phase when the primary star is in front, $\phi = 0.5$, possesses the highest count rate while the other conjunction phase with the larger secondary in front, $\phi = 0.0$, is almost half the first spectrum in terms of count rate between 0.7 and 1 keV. As far as the quadrature phase is concerned, $\phi = 0.25$, the difference is less obvious and requires further investigations in order to properly notice the differences between this observation and rev3428. However, we can already note that this first indication of variations between the observations is fully consistent with the overall picture of observing a colliding wind binary at different phases. Indeed, the same behavior of the fitted spectra was observed in 2014 by G. Rauw & al. [11] during their study of a very massive binary system HDE 228 766.

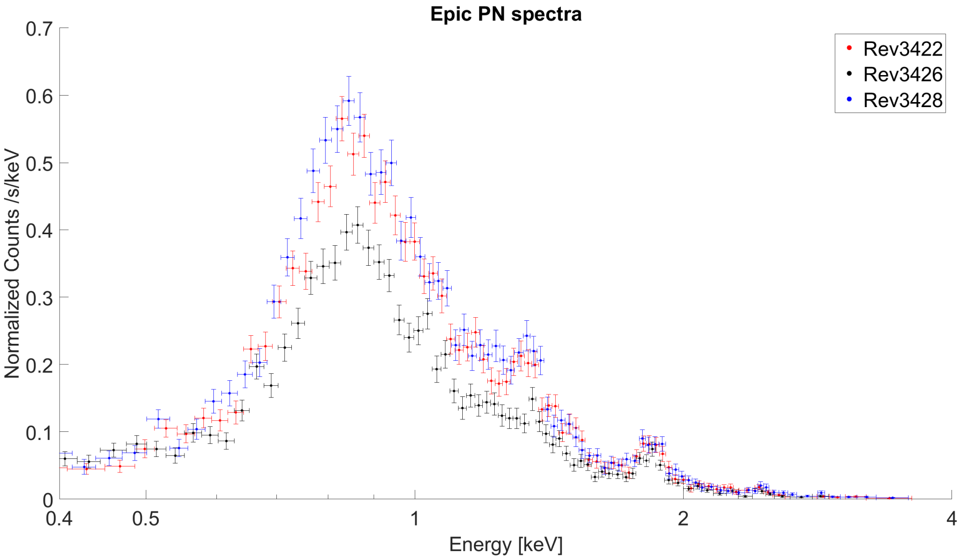

Figure 42: EPIC-PN spectra of HD 149 404 at three orbital phases.

7.2 X-ray Fluxes

The approach based on the spectra already clearly separated the two conjunction phases but we can go further to better distinguish them. To do so, based on our best fit solution for the spectra, we can extract the fluxes of each observation over a series of narrow energy bands: 0.5-0.75, 0.75-1.0, 1.0-1.5, 1.5-2.0, 2.0-3.0 and 3.0-4.0 keV. Once the fluxes in each energy band for each instrument are computed in Xspec for an observation, the three instruments are combined to get an estimation of the mean fluxes per energy band and per observation. The results are gathered on Figure 43 where we can now clearly notice the separation between the three observations. Unlike the spectra, the fluxes allow a clear distinction between rev3428 and rev3422.

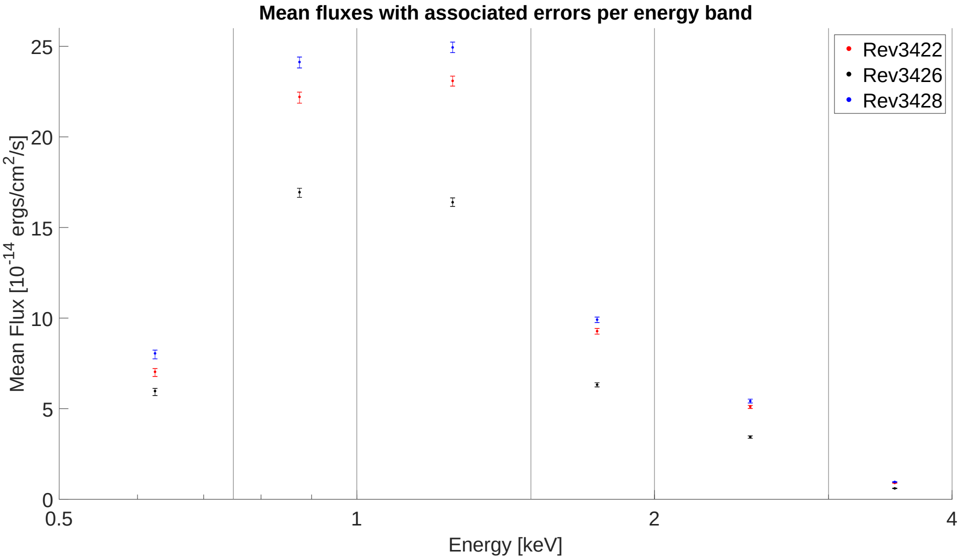

Figure 43: X-ray fluxes of HD 149 404 at three orbital phases in several energy bands.

Now that a clear distinction has been established between the three observation, we can normalize the fluxes by those of the observation displaying the highest level (rev3428). The ratio of the fluxes with the associated errors are available on Figure 44. With this final manipulation and normalization of the fluxes, the distinction and variations between the three observations are indisputable. This type of variability in the X-ray emissions, while monitoring binary systems, is a property that is commonly observed in colliding wind binary systems[12]. The phase locked variations of the X-ray emissions of such systems can either be explained by a change in the separation between the two stars due to the orbital motion or by a change of the absorption along the line of sight. In this case, the changing absorption concerns the binary system itself and not the interstellar medium and is, for instance, due to the line of sight going through denser wind during a certain phase of the binary. Taking our specific case, it was established in Section 2.1 that HD 149 404 has a circular orbit and an orbital period of 9.81 days which only leaves us with the changing absorption as the principal cause of the observed fluxes variations. Note that is was also established that HD 149 404 is a non-eclipsing binary [10].

Since the lowest observed flux level occurs when the secondary is in front (rev3426) while the maximum when the primary is in front (rev3428), this implies that the X-ray occultation and absorption are the highest by the secondary star and its wind. As the primary star wind is expected to be stronger, the shock is wrapped around the secondary star (cf. Section 6) which, consequently, is more shocked. In most colliding wind binaries, the less energetic wind is also the one which has the lower absorption in X-rays. This does not seem to be the case here. If the primary wind of HD 149 404 is indeed more energetic than the secondary wind, then the difference in absorption must come either from a low secondary wind velocity (increasing the secondary wind density despite a lower wind momentum) or from the differences in the composition of the winds.

The long-term behaviour of the X-ray flux of HD 149 404 is illustrated on Figure 45. On this Figure, the ROSAT observation made on JD2449056.813 ($\phi = 0.7$, close to the other quadrature phase) extracted from the ARNIE database at Leicester University [10] was included in red. We can see that the trend we determined from our three observations is also in agreement with the ROSAT observation error bars. From phase $\phi = 0.0$, the flux progressively increases as the line of sight passed through less and less of

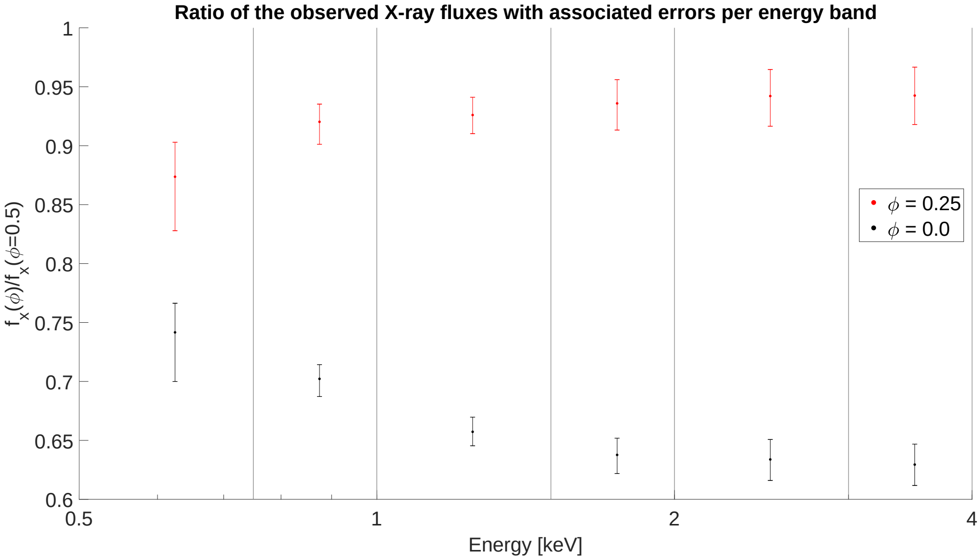

Figure 44: Ratio of X-ray fluxes of HD 149 404 in several energy bands.

the secondary wind to reach an estimated maximum around phase $\phi = 0.5$. Then the decrease starts as the line of sight of the hydrodynamic shock producing the X-rays goes through more and more of the secondary wind. We can also note that the behavior at the two quadrature phases should be different since at phase $\phi = 0.25$, the primary is coming toward us while the opposite holds true for phase $\phi = 0.75$ (cf. Section 4). This motion will impact the hydrodynamic flow of the winds in the binary system and therefore the line of sight will cross different densities at those two phases which leads to different absorptions of the X-ray emissions. However, we can notice that this effect does not seem to be very pronounced in HD 149 404.

7.3 L_x/L_{bol} ratio

When dealing with a cosmic X-ray source, an important characteristic is the ratio between the X-ray luminosity and its bolometric luminosity, L_x/L_{bol}. Indeed, soon after the all sky survey by ROSAT, it appeared that this specific ratio is constant for all O-type stars and around 10^{-7}. This trend was also confirmed by XMM-Newton and Chandra while they were studying large populations of massive stars [12][42]. Therefore, it is extremely useful to compute such a ratio for our binary system HD 149 404 in order to assess the impact of the wind collision on the X-ray brightness of the stars themselves. Since we are dealing with a ratio and to avoid errors based on the uncertainties on the distance to the binary system, the fluxes will be used instead of the luminosity to compute this ratio.

In Xspec and from our best fit models, the unabsorbed X-ray flux (corrected for the interstellar medium) used to compute the luminosities ratio can be extracted by a little trick of setting the interstellar medium absorption to zero in the TBabs model and computing the flux over the entire energy band (0.5-10.0 keV). On the other hand, to compute the bolometric flux, we will base our reasoning on the 2009 paper "Hot stars observed by XMM-Newton" written by Y. Nazé [42]. The most important formula, for us, in this paper is shown in equation 59 where we clearly see that optical data are required in order to compute the bolometric flux. Fortunately for us, the Space Technologies and Astrophysics Research (STAR) Institute at the university of Liège already thoroughly studied the binary system at those wavelengths and all the optical data required are available from the literature (cf. Section 2.1 for the exhaustive list of papers where the optical data were taken).

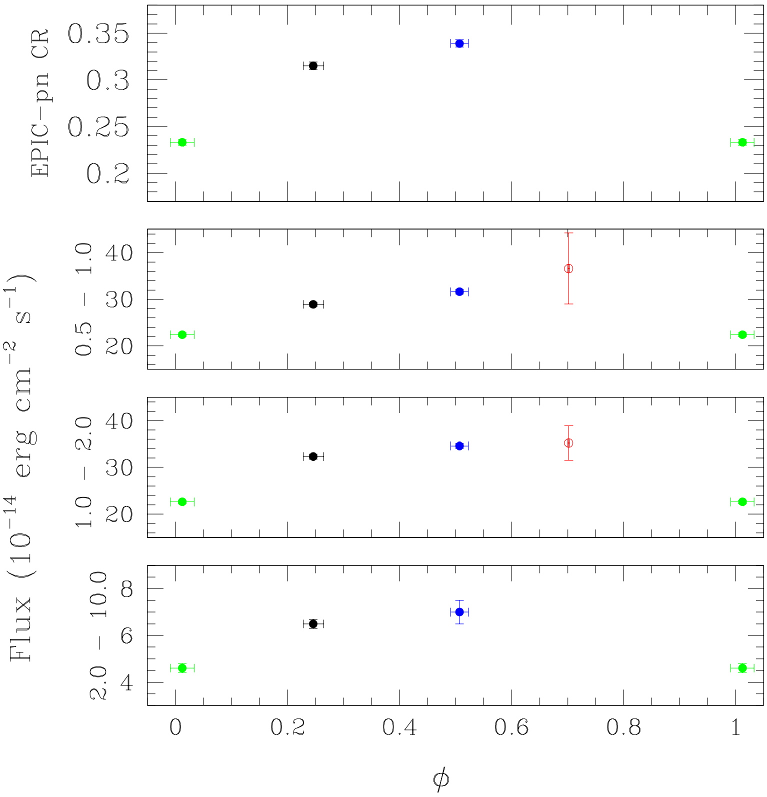

Figure 45: X-ray fluxes as a function of the binary phases (Red flux is from ROSAT observations at phase $\phi = 0.7$ [10]).

$$\log(f_{bol}) \;=\; -4.16 - \left(\frac{m_V \;-\; R_V \cdot E(B-V) \;+\; BC}{2.5} \right) \tag{59}$$

Extinction factor R_V	3.1
Color excess $E(B-V)$	0.65 ± 0.02
Brightness ratio l_1/l_2	0.70 ± 0.12
Binary magnitude m_V	5.48 ± 0.02
Bolometric correction primary $BC1$	-3.17
Bolometric correction secondary $BC2$	-2.67

Table 12: Optical parameters of HD 149 404.

Based on the parameters gathered in Table 12, the magnitude of the primary and secondary can be computed via the following equations (60) and (61):

$$m_{V,1} \;=\; m_V \;+\; 2.5\log\left(1+\frac{l_2}{l_1}\right) \;=\; 6.44 \pm 0.11 \tag{60}$$

$$m_{V,2} \;=\; m_V \;+\; 2.5\log\left(1+\frac{l_1}{l_2}\right) \;=\; 6.06 \pm 0.08 \tag{61}$$

Now in possession of all the parameters required for equation 59, we can compute the bolometric fluxes of the primary $f_{bol,1}$ and secondary $f_{bol,2}$ stars, respectively equal to 7.76±0.89 10^{-6} and 6.92±0.64 10^{-6} erg/cm^2/s. By a simple addition, the bolometric flux of the binary system HD 149 404 is obtained

($f_{bol} = 1.468 \pm 0.11\ 10^{-5}$ erg/cm^2/s). This result along with the X-ray fluxes corrected for the interstellar medium finally allows us to determine the L_x/L_{bol} ratio for the three observations.

/	ISM corrected X-ray flux 10^{-12} erg/cm^2/s	L_x/L_{bol} ratio
rev3422	1.43	$0.98 \pm 0.07\ 10^{-7}$
rev3426	1.10	$0.75 \pm 0.05\ 10^{-7}$
rev3428	1.58	$1.07 \pm 0.08\ 10^{-7}$

Table 13: X-ray fluxes and L_x/L_{bol} ratio of HD 149 404 for the three observations.

The first characteristic of this L_x/L_{bol} ratio that stands out is a match for the trend established previously regarding the fluxes. Moreover the L_x/L_{bol} ratio, within the error margins, is around a value of 10^{-7}. This value is in agreement with the majority of O-O binaries which, in itself, is consistent with assumed single O-type stars [10]. This result indicates that the wind collision in HD 149 404 is not as bright as expected. This is in line with the conclusions of other studies which found that X-ray bright wind collisions are actually the exception which HD 149 404 is not a part of. Those results were expected by G. Rauw & al. [10] in 2001 and are confirmed by this X-ray study. Similarly to the fluxes, the low L_x/L_{bol} ratio seems to point toward an X-ray dim hydrodynamic shock.

7.4 Wind collision simulation

In the previous sections, we have established the presence of phase locked variations in the X-ray fluxes and shown that the L_x/L_{bol} ratio of HD 149 404 does not reveal a strong X-ray over-luminosity. Whilst the former property is consistent with the presence of a hydrodynamic shock resulting from the collision of the stellar winds, the latter property is not. To check whether a wind interaction can explain the observed variability, we will try to model this contact discontinuity by the Canto formalism [14] in a similar manner as for the binary system HDE 228 766 [11].

The Canto formalism, developed in 1996, is based on the conservation of linear and angular momentum and designed to solve axisymmetric, steady, thin-shell problems such as the hydrodynamics shock resulting from the collision of stellar winds in a binary system [14]. It allows to constrain the properties of the shock such as the mass loss rates or wind velocity based on a resolution of a set of equations. This code is part of a program developed by the Liège group of high energy astrophysics led by professor G. Rauw entitled: "Programme pour le calcul de l'opacite X moyenne dans binaires a collision de vents stellaires" (program for the computation of the mean X-ray opacity in colliding wind binaries). In order to start the iterative process and extract the best fit properties of our system such as the orbital inclination or mass loss rates, the program requires the following information:

- Observational data accounted for by the computed flux in different energy bands.
- Opacity of the wind material involved in the binary system.
- Intrinsic emissivity of elements that display lines within the energy band covered by the observation.

For the observational fluxes, the values provided correspond to the ones we have already detailed and analyzed in this section. As far as the intrinsic emissivity is concerned, we will use the 6 lines presented in Table 14. They have been chosen since they are well within the energy band covered by our data (0.5-10 keV). Finally, for the opacity of the binary, we have to determine the opacity of each star. Indeed, as we have already mentioned, depending on the phase of the binary system HD 149 404, the line of sight is crossing the wind of the primary or the secondary. For the conjunction phases, the concerned wind stands immediately out if we refer to the scheme of the binary system on Figure 5 [10]. Emitted X-rays cross the wind of the secondary star during rev3426 ($\phi = 0.0$) while the primary wind during rev3428 ($\phi = 0.5$). The situation is however more complicated regarding the conjunction phase rev3422 where the shock is seen perpendicularly to the line joining the two stars. At this phase, the sight lines towards the front part of the shock cross only the primary wind, whereas those towards the rear part of the shock cone cross both winds. The exact answer to this question depends on the shape of the shock and mainly the opening angle of the shock cone which, at this stage, is unknown and a free variable.

Line	O VIII Ly α	O VIII	Mg XI	Al XIII Ly α	S XIII	Ar XVII
Energy [eV]	653.55	817.03	1352.10	1729.20	2440.20	3701.00

Table 14: Elements used for the intrinsic emissivity in the Canto code.

To compute the opacity, once again, we will make use of the available literature and, especially, the reference paper [9] where a spectral disentangling routine was used on Optical and UV data in order to reconstruct the individual spectra of the primary and secondary stars as well as important properties of the system (cf. Section 2.1). Thanks to the work of F. Raucq and her collaborators, the opacity of each star can be computed. The wind opacity of the primary (1) and secondary (2) is shown on Figure 46 at a distance of a/2 from the respective center of each star[2]. For our specific system, this implies the wind opacity at half the distance between the two stars. Those two curves are extremely close to each other and exhibit the same shape beyond 0.7 keV with the same jump around 7-8 keV. Below 0.7 keV, the behavior is actually quite different which could be attributed to the differences in composition between the two winds that play a major role at low energy as we already explained in previous section (cf. Section 6 and the CNO abundances of the two stars on Figure 7). The optical depth is then simply computed by the relation 62 which corresponds to the integral of the wind opacity curve along a specific line of sight dz.

$$\tau(E) = \int \kappa(E) \cdot \rho \; dz \tag{62}$$

The fact that the opacity curves are extremely close was also expected from the ratio of the fluxes at phases $\phi = 0.0$ and $\phi = 0.5$ on Figure 44. Indeed, the flux is proportional to the emission times the exponential of the optical depth. Since the emission is not changing with the orbital phase but only the optical depth, the ratio of fluxes is actually proportional to the exponential of the difference between the optical depth of the primary and secondary. Therefore, in the case of HD 149 404, where the ratio of those two fluxes is relatively close to one (around 0.65), unlike HD 228 766 where this ratio is closer to 0.1, the optical depths and, consequently, the opacity of the winds were expected to be close to each other.

Now that we have at our disposal all the required parameters and information regarding the binary system HD 149 404, we can use the program to derive properties of the binary system. Let's first have a look at how the system is represented in the Canto formalism on Figure 47 (note that all the distances are expressed as unit of semi major axis a, the radius of the circular orbit). On this Figure, we can see a scaled version of the primary and secondary star assuming an inclination of 25°, hence a semi major axis of 72.6 $R_\odot$ (cf. Section 2.1). Important quantities such as the stagnation point, the opening angle θ and the general shape of the hydrodynamic shock, all discussed in Section 2.3, can also be noticed. Those quantities mainly depend on the relative strength between the two stellar winds accounted for by the wind momentum ratio $\eta = \frac{\dot{M}_2 \; v_2}{\dot{M}_1 \; v_1}$. Finally, we can also observe a portion of the contact discontinuity in purple color and whose size is related to the parameter r_{max}. This maximum radius, defined from the

---

[2] a stands for the radius of the circular orbit of HD 149 404.

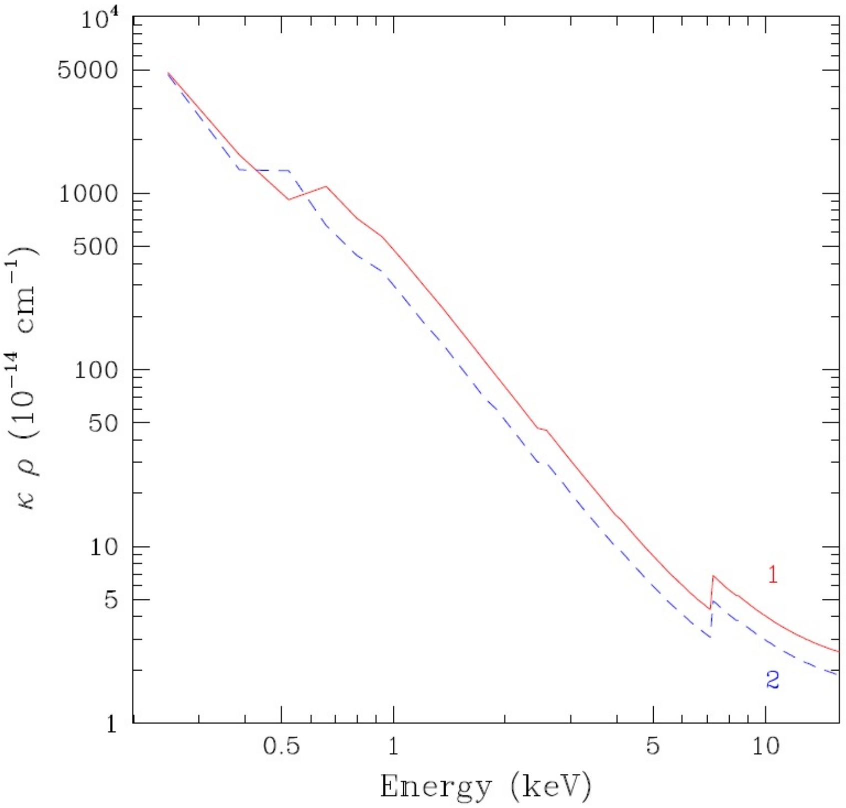

Figure 46: Product of the wind opacity κ and the wind density ρ as a function of the energy for the binary system HD 149 404 computed from the CMFGEN model of F. Raucq et al.[9] and adopting their values of the wind mass-loss rates and wind velocities. .

center of the primary star, represents the limit above which the hydrodynamic shock does not produce X-ray photons anymore. This limit can be easily understood by the properties of a hypersonic shock. Indeed, if we consider the bow shock happening in our system, at the stagnation point, we have a normal strong shock that was considered in Section 2.3 but going further away from this point, the shock is actually more and more inclined with respect to the upstream flow and we have an oblique shock. This oblique shock is weaker and weaker as it happens further away from the stagnation point which leads to a lower and lower post shock temperature and, hence, a lower plasma temperature. Therefore, the different processes leading to X-ray emissions are unable to take place at some point which is defined by this maximum radius.

As mentioned, the position of the shock and its shape are strongly influenced by the wind moment ratio η. It is already expected that the wind of the primary is stronger than the one of the secondary which leads to a shock closer to the secondary star as we saw on Figure 47. As the wind of the primary increases in strength and/or the secondary wind decreases, the position of the shock will be shifted toward the secondary star and up to a contact of the shock with the photosphere of the secondary. In that situation, the wind of the primary is directly impacting the secondary star without the formation of a shock and the shock is only created outside the secondary star as depicted on Figure 48 (this situation was also explained in Section 2.3 when discussing the simulation of E. Gosset and E.R. Parkin of an eccentric binary system). For our binary system HD 149 404, this situation is reached when the wind momentum ratio is below the critical value of 0.524. Imposing such a limit, in the code, for the wind momentum ratio in the colliding wind program ensures the hydrodynamic shock is not in contact with the secondary star. However, once the results of the wind collision model obtained for various values of the maximum radius of X-ray emissions, from 0.25 to 5.0 a, the fitting statistic χ^2 was always extremely high no matter the maximum radius (values of at least several hundreds) which leads to the conclusion that the model was not a good fit for the observations.

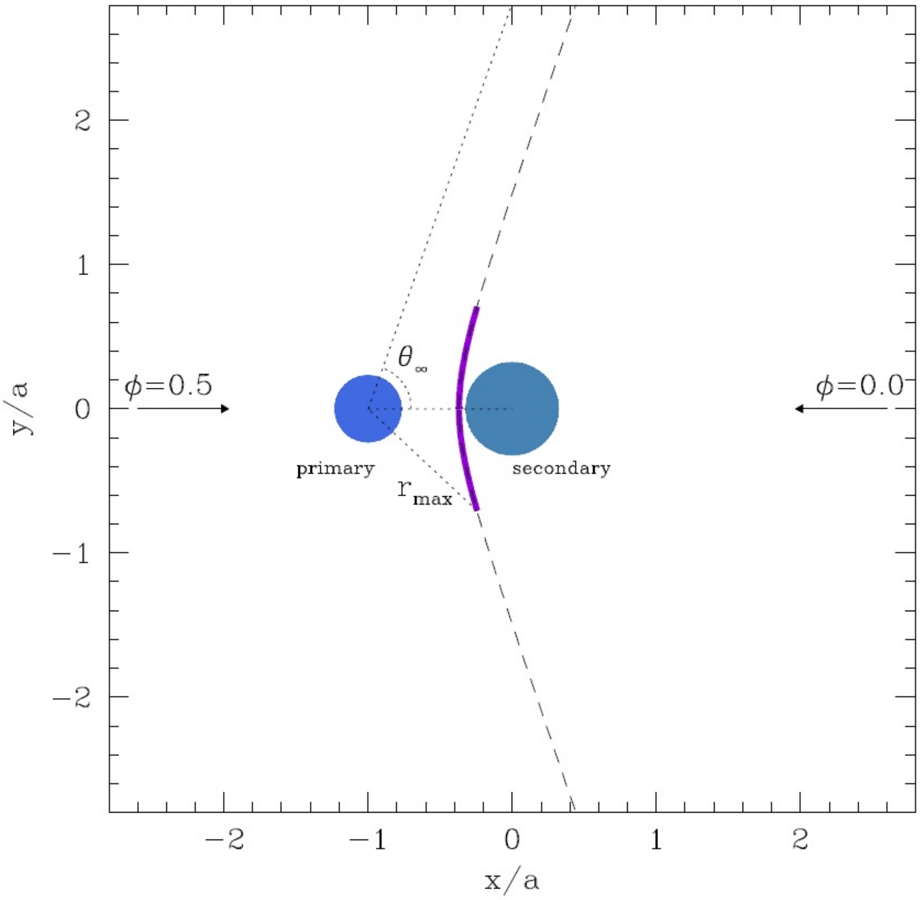

Figure 47: Scheme of the wind collision in the binary system HD 149 404 ($\eta > 0.524$).

Following this observation, values of the wind moment ratio lower that the critical one were allowed. In this case, the X-ray emissions were assumed coming solely from the hydrodynamic shock up to r_{max} but not from the region in contact with the photosphere of the secondary star. The X-ray emissions regions are shown on Figure 48 by the purple color. Compared with the assumption made previously, Figure 47, we can clearly see that the emitting region is now much smaller. With those new constraints, the model greatly improved leading to the following results for different values of the maximum radius (cf. Table 15):

R_{max}/a	χ^2
0.25	21.70
0.5	18.29
0.75	139.05
1.0	170.18
3.0	183.13
5.0	182.79

Table 15: r_{max} and associated impact on the solution (Canto model without limit on η).

By removing this limitation on the wind momentum ratio η, we can see a direct improvement on the fit with a χ^2 as low as 18.29. This also leads to establish that a good fit solution is associated with a

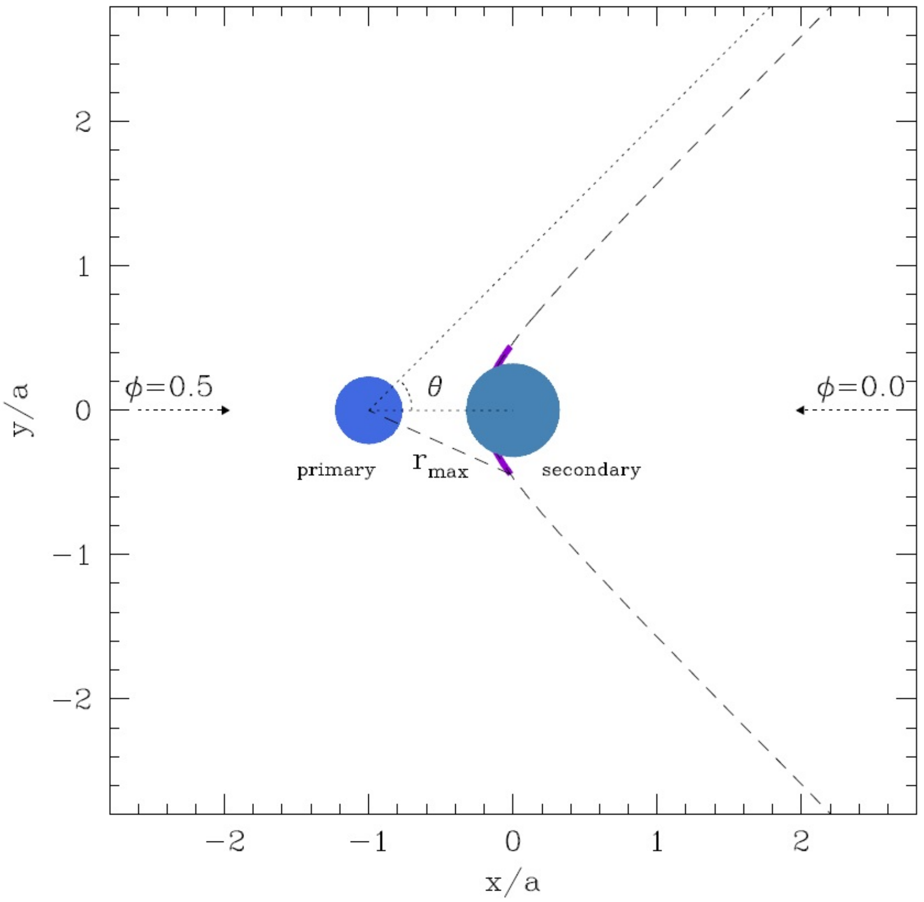

Figure 48: Scheme of the wind collision in the binary system HD 149 404 ($\eta \leq 0.524$).

maximum radius below 0.75 times the semi major axis. With the lowest value of the χ^2 18.29 in a 90% confidence interval (+ 12.02), we can use our model to extract the properties of the binary system that lead to a value equal or lower than a χ^2 of 30.31. All those properties are gathered in Table 16.

Orbital inclination [°]	23.0 ± 0.9
Secondary mass loss rate $\dot{M}_2$ [10^{-6} $M_\odot$/yr]	0.27 ± 0.04
Secondary wind velocity $v_{inf,2}$ [km/s]	125
Primary mass loss rate $\dot{M}_1$ [10^{-6} $M_\odot$/yr]	0.19 ± 0.04
Primary wind velocity $v_{inf,1}$ [km/s]	2539 ± 184
Shock cone aperture angle θ_∞ [°]	43.5 ± 1.5

Table 16: HD 149 404 properties, best fit model.

The orbital inclination of 23° based on the X-ray observations for our best fit model is consistent and in agreement with the value found in 2001 by G. Rauw & al. [10] but also with the latest study of the binary system HD 149 404 using photometric data collected by the BRITE-Heweliusz satellite performed by G. Rauw & al. [13]. In the latter, an inclination range between 23 and 31 ° was found which led to huge uncertainties regarding the stellar masses of both components. With our study, a new constraint on the stellar masses is found and, based on the minimal masses found by G. Rauw & al. [10] (cf. Section 2.1), we obtain a stellar mass of 42.24±3.52 $M_\odot$ for the primary and 25.48±2.18 $M_\odot$ for the secondary. We can also notice that the shock cone is really crashed on the secondary star and that the secondary wind is strongly dominated by the primary one noting a wind momentum ratio of 0.07 for our best fit solution, well below the critical value of 0.524 established previously. While the estimated mass loss rate of both stars is in agreement with typical values for O-type star (10^{-7} up to 10^{-4} $M_{\odot}$/yr), the wind velocity is a different story. Indeed, the wind velocity of the primary star is again well within typical values for such massive stars but the secondary, with a terminal velocity of 125 km/s is well below the usual values (from 1000 to 3000 km/s). This surprising result can, at least in part, be due to the fact that the secondary wind does not have the time to accelerate before it collides with the primary wind. Regarding the mass loss rates, we can also compared with values gathered by F. Raucq & al. [9] (cf. Section 2.1) and we directly notice that the order of magnitude of the mass loss rate is identical while the trend is reversed. Indeed, in our study, we found that the mass loss rate of the secondary is actually greater than the one of the primary.

With the binary system properties we found in our best fit solution, we can compute the ratio of fluxes at different phases and in the energy bands used when analyzing the X-ray fluxes. They could then be compared with the ratio determined based on our spectral model as shown on Figure 49. We can immediately observe that the model actually fits really well the observations at the conjunction phase (ϕ = 0.0) while the quadrature phase ($\phi = 0.25$) is poorly represented (reduced χ^2 above 2.6). The failure of our model to fit the flux ratios for both situations equally well could suggest that our assumption that the X-rays mostly arise from the shock between the winds is wrong. Indeed, as an alternative, the bulk of the X-ray emission could be intrinsic to the winds of the individual stars. This conclusion can also be supported by the X-ray luminosity that is fully compatible with that of single O-type stars and does not show a significant increase that could be explained by an excess emission resulting from the hydrodynamic shock.

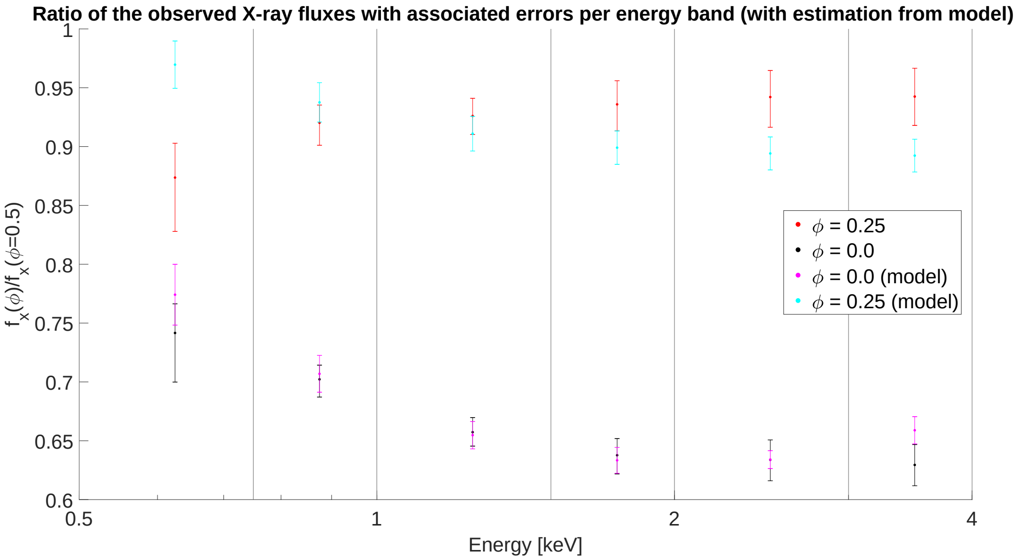

Figure 49: Ratio of X-ray fluxes of HD 149 404 (including fluxes from model).

Note that the Figures 47 and 48 as well as the results from the wind collision simulation were realized and obtained using the data of this thesis by professor G. Rauw due to my inability to continue working at the university of Liège following the closing decision of the university by the rector P. Wolper during this pandemic.

8 Future Perspectives

With the arrival of the coronavirus and the global pandemic it caused, the academic activities have been moved to the internet and the university was closed for students. This unforeseen and unfortunate event had a consequence on this thesis and prevented to achieve all the objectives initially set. In this section, we will briefly discuss what steps could come after the Canto model and that would have been, in part, realized without the pandemic.

Following the results of the wind collision simulation, it seems plausible that the observed X-rays are not coming from the wind collision region but rather due to intrinsic emissions from the stars which is a conclusion also compatible with the fluxes and L_x/L_{bol} ratio determined. This scenario could be confirmed by the use of another model than the Canto formalism to assess this trend and ensure that the conclusion truly matches what is happening in the binary system. If this conclusion stands, it would be useful to develop a simulation of the hydrodynamic shock as well as the surrounding wind and not only the contact discontinuity as we did with the Canto formalism. This corresponds to a dedicated hydrodynamical simulation of the binary system and, in particular, the region between the two stars to better understand the origin of the emissions. Moreover, in the Canto formalism, a steady, axisymmetric shock is assumed while we are observing a dynamical system. Therefore, it would be interesting to have a look at the deflection of the shock cone and the overall spiral motion resulting from the orbital motion of the stars. So far, we have also not assessed what was happening to the post shock plasma. The effect of radiative cooling in the post shock plasma and its possible effect on the upstream wind can also be an interesting issue to address.

Finally, we have seen during the reduction of the data that we have an data set of extremely good quality and barely affected by the background (very small impact for rev3426). During this process, we have also detected many other fainter X-ray sources (cf. Section 5 and, especially, Figure 38). It could therefore be interesting to identify their optical counterparts (if any), and, for instance, try to fit the brightest ones with a spectral model similarly to what we did for HD 149 404 and, if possible, extract some important properties such as the L_x/L_{bol} ratio.

9 Conclusion

In this thesis entitled "Probing the wind interaction in the massive binary system HD 149 404 with XMM-Newton", we started by a brief description of the binary system using the scientific literature to extract relevant properties of the system useful for our work. We learned that the binary system was made of a type O7.5 If primary star and a type ON9.7 I secondary star and that the binary system had experienced a case A Roche lobe overflow in the past. Information regarding the ephemeris of the binary as well as the CNO abundances were also gathered at that point.

With this better understanding of HD 149 404, the intriguing nature of those incredible objects that are massive stars and their peculiar evolution, especially in binary systems, pushed us to briefly describe them and understand how carbon, oxygen or even nitrogen could possibly end up with such abundances in the stellar photosphere and wind. Then, the study was focused on the wind-wind interaction and the production of a contact discontinuity, an hydrodynamic shock. In a first time, we took an interest in the geometry of the shock and its location which allows us to state the importance of the wind momentum ratio η in colliding wind binaries since this ratio is solely responsible for the location of the stagnation point as well as the opening of the shock cone. In a second and final time, we took an interest in the physical properties of such an interaction by starting with the Navier-Stokes equations and establishing the Rankine-Hugoniot relations for steady strong hypersonic shocks. Those relations allowed to understand how the post shock plasma could reach temperatures of several million Kelvin. The presence of such hot plasma and an hydrodynamical shock justified the need and interest of X-ray observations by XMM-Newton.

After briefly describing the data set obtained by XMM-Newton and corresponding to observations of the binary system close to phase 0.0 , 0.25 and 0.5, the crucial step of data reduction was realized. This step is peculiarly important since it allows to turn raw X-ray data obtained by XMM-Newton into scientifically usable data that can be fitted with a spectral model. With the Science Analysis System, SAS, we were able to calibrate the list of events and discard bad events such as the impact of a cosmic ray thanks to a grade filtering routine. A special attention was paid to the background activity and, in particular, the solar activity and the detection of solar flares. The low-energy protons ejected during those flares can, unfortunately, reach the X-ray detectors and produce a background flare that can seriously impact the quality of the X-ray data. The data rev3422 and rev3428 were acquired during low background activity. This was, however, not the case of rev3426 and we had to discard the data acquired during the high background activity which luckily lasted a short while and solely impacted a small portion of the observation rev3426. In possession of a calibrated list of good events, we were able to identify all the sources in the XMM-Newton field of view and, especially, the binary system HD 149 404, the brightest X-ray source of the field of view. With our target identified, we defined a source and background region to extract, for each observation, an observational spectrum of HD 149 404.

Once the observational spectra obtained, they could be fitted with a spectral model thanks to the Xspec software. There, we separated the absorption by the interstellar medium from the photoelectric one within the binary system itself. Making use of the empirical relation established by S. B. Gundennavar, the hydrogen column density of the interstellar medium was fixed while the absorption by the binary system was left as a free parameter. As far as the plasma involved in the system is concerned, it was modeled by two optically thin thermal plasma models at two different temperatures. From this simple first spectral model, many upgrades were done. We discussed the addition of more temperatures in our model but rejected this idea following an F-statistic study that clearly showed a two temperatures model to be the best solution. Based on the CNO abundances of the two stars involved in the binary system, we discussed different mixing of the stellar winds and demonstrated that an emitting plasma with a 50/50 mixture of the stellar winds was ideal to describe HD 149 404. Thanks to the scientific literature and our hypothesis, we were able to reach an excellent fit for the observational spectra and constrain many parameters.

Our best fit solution/model in hand, we could begin a deeper analysis of the binary system. We first compared the spectra of the three observations to look for variations, signs of the presence of an hydrodynamical shock in the system. Those variations were found as expected and their presence was made more obvious by a computation of X-ray fluxes in several energy bands. The conjunction phase ϕ = 0.5 with the primary in front clearly stood out as dominating the X-ray flux while a minimum was reached at the other conjunction phase $\phi = 0.0$. We identified phase locked variations compatible with the presence of an hydrodynamic shock and in agreement with the ROSAT data ($\phi = 0.7$). However, we noticed that those variations were quite small and not as spectacular as those observed in HDE 228 766. We continued our analysis with the computation of the L_x/L_{bol} ratio which did not show an excess that could be attributed to the presence of X-rays resulting from the hydrodynamic shock. Finally, based on our results, we applied the Canto formalism in order to simulate the wind-wind interaction and extract properties of the binary system such as the orbital inclination. The result of this simulation allowed to bring new constraints on the stellar masses of the stars in the binary system but also indicates that the X-ray emissions are possibly intrinsic to the stellar winds themselves and not coming from the shock created by the interaction of the stellar winds.

Those results require further investigations such as a proper hydrodynamical simulation in order to fully understand what is happening within this binary system. This work could be the basis of a deeper analysis with more advanced techniques that could improve the comprehension and knowledge we have of such binary systems.

References

[1] International astrophysical consortium for high energy calibration. URL: `https://iachec.org/`.

[2] Introduction and emission mechanisms. URL: `http://spiff.rit.edu/classes/ast613/lectures/radio_i/radio_i.html`.

[3] Inverse compton scattering. URL: `https://www.researchgate.net/publication/275836032/figure/fig12/AS:667202403463169\spacefactor\@m{}1536084857620/Inverse-Compton-scattering.jpg`.

[4] Pp chain and cno cycle. URL: `https://www.researchgate.net/figure/The-respective-weights-of-the-p-p-chain-and-CNO-cycle-in-the-global-stellar-luminosity_fig9_267157073`.

[5] Radiative recombination. URL: `https://www.researchgate.net/figure/Sources-of-recombination-losses-radiative-recombination-A-non-radiative-recombination_fig3_281383935`.

[6] X-ray production: Bremsstrahlung interaction. URL: `https://i.ytimg.com/vi/xFL-B9wbRsg/maxresdefault.jpg`.

[7] Airbus. Xmm-newton before launch. URL: `https://www.airbus.com/newsroom/press-releases/fr/2019/12/twenty-years-of-xray-astronomy-with-xmmnewton.html#media-list-image-image-all_ml_0-2`.

[8] E. R. Parkin & al. 3d modelling of the massive star binary systems eta carinae, wr 22, and wr 140. *Bulletin de la Societe Royale des Sciences de Liege*, 80:610, 01 2011. URL: `https://popups.uliege.be:443/0037-9565/index.php?id=3074`.

[9] F. Raucq & al. Observational signatures of past mass-exchange episodes in massive binaries: The case of hd 149 404. *Astronomy & Astrophysics*, 588(A10), 2016. `doi:https://doi.org/10.1051/0004-6361/201527543`.

[10] G. Rauw & al. The strange case of the massive binary hd149404. *Astronomy & Astrophysics*, 368(1):212–224, 2001. `doi:https://doi.org/10.1051/0004-6361:20000527`.

[11] G. Rauw & al. Phase resolved x-ray spectroscopy of hde288766: Probingthe wind of an extreme of+/wnlha star. *Astronomy & Astrophysics*, 566(A107), 2014. `doi:https://doi.org/10.1051/0004-6361/201423885`.

[12] G. Rauw & al. X-ray emission from interacting wind massive binaries: A review of 15 years of progress. *Advances in Space Research*, 58(5):761–781, 2016. `doi:https://doi.org/10.1016/j.asr.2015.09.026`.

[13] G. Rauw & al. Brite photometry of the massive post-rlof system hd149 404. *Astronomy & Astrophysics*, 621(A15), 2018. `doi:https://doi.org/10.1051/0004-6361/201833594`.

[14] J. Canto & al. Exact, algebraic solutions of the thin-shell two-wind interaction problem. *Astrophysical Journal*, 469, 1996. `doi:https://doi.org/10.1086/177820`.

[15] M. Asplund & al. The chemical composition of the sun. *Annual Review of Astronomy and Astrophysics*, 47:481–522, 2009. `doi:https://doi.org/10.1146/annurev.astro.46.060407.145222`.

[16] P. Goldoni & al. First results of ibis/isgri cygnus x-3 monitoring during integral pv phase. *Astronomy & Astrophysics*, 411, 2003. `doi:https://doi.org/10.1051/0004-6361:20031392`.

[17] S. B. Gudennavar & al. A compilation of interstellar column densities. *The Astrophysical Journal Supplement Series*, 199(1), 2012. `doi:https://doi.org/10.1088/0067-0049/199/1/8`.

[18] AtomDB. Atomic data for astrophysicists. URL: `http://atomdb.org/`.

[19] PennStata college. The evolution of massive stars and type ii supernovae. URL: `https://www.e-education.psu.edu/astro801/content/l6_p5.html`.

[20] M.-A. Dupret. Ulg lecture: Stellar structure and evolution, 2019-2020.

[21] ESA. Epic mos 1 (2 ccds out of order). URL: `https://www.cosmos.esa.int/web/xmm-newton/mos1-ccd3`.

[22] ESA. The european photon imaging camera (epic) on board xmm-newton. URL: `https://www.cosmos.esa.int/web/xmm-newton/technical-details-epic`.

[23] ESA. The layout of the mos cameras. URL: `https://xmm-tools.cosmos.esa.int/external/xmm_user_support/documentation/uhb/moschipgeom.html`.

[24] ESA. The quantum efficiency of the mos ccds. URL: `https://www.cosmos.esa.int/web/xmm-newton/technical-details-epic`.

[25] ESA. Xmm-newton announcement of opportunity. URL: `https://www.cosmos.esa.int/web/xmm-newton/ao19`.

[26] ESA. Xmm-newton announcement of opportunity: policies and procedures. URL: `https://xmm-tools.cosmos.esa.int/external/xmm_user_support/documentation/AOpolicy/index.html#propeval`.

[27] ESA. Xmm-newton data files handbook. URL: `http://xmm-tools.cosmos.esa.int/external/xmm_user_support/documentation/dfhb/node1.html`.

[28] ESA. Xmm-newton mission. URL: `https://sci.esa.int/web/xmm-newton/-/31249-summary`.

[29] ESA. Xmm-newton observational database search. URL: `https://xmmweb.esac.esa.int/cgi-bin/xmmobs/public/obs_view_cosmos.tcl?search_rev=&search_ra=&search_target=HD149404&search_obs_start=&search_obs_id=&search_dec=&search_pi=&search_obs_end=&search_prop=&search_radius=&search_category=0&search_order_by=3&search_instrument=0&action=Get+Selection`.

[30] ESA. Xmm-newton routine calibration programme. URL: `https://xmm-tools.cosmos.esa.int/external/xmm_user_support/documentation/uhb/routinecal.html`.

[31] ESA. Xmm-newton science archive. URL: `http://nxsa.esac.esa.int/nxsa-web/#search`.

[32] ESA. Xmm-newton users handbook. URL: `https://xmm-tools.cosmos.esa.int/external/xmm_user_support/documentation/uhb/epicmode.html`.

[33] E.R. Parkin & E. Gosset. Simulation of colliding wind binary. URL: `https://sci.esa.int/web/xmm-newton/-/50922-simulation-of-colliding-wind-binary`.

[34] C. Hirata. Caltech lecture: Interstellar shocks, 2011. URL: `http://www.tapir.caltech.edu/~chirata/ay102/Shocks.pdf`.

[35] Craig Gordon & Ben Dorman Keith Arnaud. *An X-Ray Spectral Fitting Package, Users' Guide for version 12.11*. 2020. URL: `https://heasarc.gsfc.nasa.gov/xanadu/xspec/manual/XspecManual.html`.

[36] P. Magain. Ulg lecture: Astrophysics, 2019-2020.

[37] T. Magin. Ulg lecture: Aerothermodynamics of high speed flows, 2016-2017.

[38] NASA. Doomed star eta carinae. URL: `https://apod.nasa.gov/apod/ap190220.html`.

[39] NASA. High energy astrophysics science archive research center. URL: https://heasarc.gsfc.nasa.gov/.

[40] NASA. Messier 16 (the eagle nebula). URL: https://www.nasa.gov/feature/goddard/2017/messier-16-the-eagle-nebula.

[41] NASA. Xmm-newton mirror at csl. URL: https://imagine.gsfc.nasa.gov/educators/programs/xmm/mission/mirrors.html.

[42] Y. Nazé. Hot stars observed by xmm-newton i. the catalog and the properties of ob stars. *Astronomy & Astrophysics*, 506(2):1055–1064, 2009. doi:https://doi.org/10.1051/0004-6361/200912659.

[43] Mike Peel. A replica of xmm-newton at the cite de l'espace in toulouse, france. URL: https://upload.wikimedia.org/wikipedia/commons/thumb/8/88/XMM-Newton_at_Cite_de_l%27espace_2.jpg/1200px-XMM-Newton_at_Cite_de_l%27espace_2.jpg.

[44] G. Rauw. Xmm proposal: Constraining the properties of the post-rlof massive binary hd149404.

[45] G. Rauw. Ulg lecture: High-energy astrophysics, 2019-2020.

[46] G. Rauw. Ulg lecture: Variable stars, 2019-2020.

[47] Simbad. Hd 149404 basic data. URL: http://simbad.u-strasbg.fr/simbad/sim-id?Ident=HD%20149404#lab_bib.

[48] XMM-Newton Science Operations Centre Team. *Users Guide to the XMM-Newton Science Analysis System*. 2019. URL: https://xmm-tools.cosmos.esa.int/external/xmm_user_support/documentation/sas_usg/USG/.

[49] Eichler D. & Usov V. Particle acceleration and nonthermal radio emission in binaries of early-type stars. *Astrophysical Journal*, 402, 1993. doi:https://doi.org/10.1086/172130.

[50] Vinay Venugopal. The geometry of compton scattering. URL: https://www.researchgate.net/figure/The-geometry-of-Compton-scattering-showing-the-directions-of-the-scattered-photon-a
fig1_236737231.